Photocatalytic Hydrogen Production Using Layered Perovskite Oxides

By

Ali Berk Demir

A Dissertation Submitted to the
Graduate School of Sciences and Engineering
in Partial Fulfillment of the Requirements for
the Degree of

Master of Science

in

Materials Science and Engineering

KOÇ
ÜNİVERSİTESİ

June 29, 2022

Photocatalytic Hydrogen Production Using Layered Perovskite Oxides

Koç University

Graduate School of Sciences and Engineering

This is to certify that I have examined this copy of a master's thesis by

Ali Berk Demir

and have found that it is complete and satisfactory in all respects,
and that any and all revisions required by the final
examining committee have been made.

Committee Members:

Assoc. Prof. Uğur Ünal (Advisor)

Asst. Prof. Umut Aydemir

Assoc. Prof. Mustafa Kemal Bayazıt

Date: 29.06.2022

The future is uncertain, and the end is always near.

ABSTRACT

Photocatalytic Hydrogen Production Using Layered Perovskite Oxides

Ali Berk Demir

Master of Science in Materials Science and Engineering

June 29, 2022

Fossil fuels have a known impact on environmental pollution, and there is a possible scarcity of these fuels in the future. Because of this reason, cleaner and more abundant fuels may be preferred for substitution. Hydrogen, an eco-friendly and promising fuel obtained from electrolysis, is a strong candidate for this purpose. Since solar energy is renewable, electrolyzing water using semiconductors is a sustainable approach.

The photocatalytic water splitting reaction can be done by using perovskite oxides, and there are many examples of perovskite oxide materials that can be found in the literature for this purpose. Among these perovskite oxides, layered perovskite oxides stand out because of their chemical stability, tunable morphology, and low-cost precursor chemicals. Sr_2TiO_4 and $KCa_2NaNb_4O_{13}$ are layered perovskite oxides, which have a limited number of studies in the literature, were inspected for their hydrogen evolution capability in this dissertation. The stated molecular structures were studied both with and without dopants to determine their hydrogen evolution rates.

Adding additives to a photocatalyst is a widely used method for bandgap engineering. In the study, the effect of copper and nitrogen addition was tested for Sr_2TiO_4 without the addition of a cocatalyst. Noble metals (Pt, Pd, Ru, Rh) were added to $KCa_2NaNb_4O_{13}$ during the synthesis instead of being added later, and hydrogen production rates were evaluated. In addition, proton exchange method was used to increase the surface area of $KCa_2NaNb_4O_{13}$ and change its electronic structure.

The structural analysis methods, optical measurements, and hydrogen evolution tests were performed on these materials to evaluate their properties. According to the results, both materials were successfully synthesized, their bandgap changes were determined, and their hydrogen production rates increased after the doping and proton exchange processes.

ÖZETÇE

Katmanlı Perovskit Oksitler ile Fotokatalitik Hidrojen Üretimi

Ali Berk Demir

Malzeme Bilimi ve Mühendisliği, Yüksek Lisans

29 Haziran 2022

Fosil yakıtların çevre kirliliği üzerinde bilinen bir etkisi vardır ve gelecekte bu yakıtların olası bir kıtlığı söz konusudur. Bu nedenle ikame amaçlı daha temiz ve daha bol bulunan yakıtlar tercih edilebilir. Elektrolizden elde edilen çevre dostu ve gelecek vaat eden bir yakıt olan hidrojen bu amaca uygun güçlü bir adaydır. Güneş enerjisi yenilenebilir olduğundan, yarı iletkenler kullanarak suyun elektrolize edilmesi sürdürülebilir bir yaklaşımdır.

Fotokatalitik su ayırma reaksiyonu, perovskit oksitler kullanılarak yapılabilir ve bu amaçla literatürde bulunabilecek birçok perovskit oksit malzeme örneği mevcuttur. Bu perovskit oksitler arasında, kimyasal kararlılıkları, ayarlanabilir morfolojileri ve düşük maliyetli öncül kimyasalları nedeniyle katmanlı perovskit oksitler öne çıkar. Literatürde sınırlı sayıda çalışma bulunan katmanlı perovskit oksitlerden olan Sr_2TiO_4 ve $KCa_2NaNb_4O_{13}$ bu tezde hidrojen üretim oranları açısından incelenmiştir. Belirtilen moleküler yapılar, hidrojen evrim oranlarını belirlemek için hem katkılı hem de katkısız olarak incelenmiştir.

Bir fotokatalizöre katkı maddelerinin eklenmesi, bant aralığı mühendisliği için yaygın olarak kullanılan bir yöntemdir. Yapılan çalışmada bakır ve nitrojen katkısının etkisi, bir yardımcı katalizör eklenmeden Sr_2TiO_4 için test edilmiştir. Soy metaller (Pt, Pd, Ru, Rh) $KCa_2NaNb_4O_{13}$'e sonradan eklenmek yerine sentez sırasında katkılanmış ve hidrojen üretim hızları değerlendirilmiştir. Ayrıca, $KCa_2NaNb_4O_{13}$'ün yüzey alanını arttırmak ve elektronik yapısını değiştirmek için proton değişim yöntemi kullanılmıştır.

Özelliklerini değerlendirmek için bu malzemeler üzerinde yapısal analiz yöntemleri, optik ölçümler ve hidrojen evrim testleri yapılmıştır. Elde edilen sonuçlara göre her iki malzeme de başarılı bir şekilde sentezlenmiş, bant aralığı değişimleri belirlenmiş ve katkılandırma ve proton değişim işlemleri sonrasında hidrojen üretim hızları artmıştır.

AKNOWLEDGEMENTS

First and foremost, I would like to thank my advisor, Assoc. Prof. Uğur Ünal for giving me this opportunity and supporting me throughout my bachelor's and master's studies. He was always kind and helpful. In addition, I would like to acknowledge Dr. Ceren Yılmaz Akkaya and Dr. Durata Haciu for their exceptional contributions during my bachelor's years. I learned a lot from these people; they will always have a special place in my heart.

I also want to pay my gratitude to my colleagues from Unal Lab. Significantly, Bengisu Yılmaz and Tuğba Yalçın helped me tremendously with my studies from the beginning of this journey, and they were great friends that I am going to remember my whole life. In addition, I would like to thank my remaining colleagues, Armin Ashgari Alamdari, Hasibe Gizem Kanat, and Dr. Mohammedreza Khodabakhsh, for their lovely companionships and support.

I also would like to thank to my friends Hatice Pelin Çağlayan, Kaan Yalçın, Ezgi Hatipoğlu, İlayda Terzi, Ebrahim Sadeghi, and Dr. Naeimeh Sadat Peighambardoust from the other joints at Koç University. They were always so kind and conversing with them to improve myself scientifically was always joyful.

I want to thank Asst. Prof. Umut Aydemir and Assoc. Prof. Mustafa Kemal Bayazıt, for honoring me by being part of my defense jury and their kindness. Also, I would like to thank Dr. Barış Yağcı for his aid with characterization measurements and Prof. Cemal Özeroğlu for leading me to academia.

I would like to pay my respects and gratitude to my mother, Hanife Demir, and my father, Yüksel Demir, for their unconditional support. In addition, I would like to thank my aunt Serpil Demir and my grandmother Güner Demir. We endured many hard times together. I am glad they were always there for me.

Finally, I would like to thank to TÜBİTAK for supporting this research under project no 118Z865 and title "Katmanlı perovskit yapıların 2D nanokatmanlarının fotokatalitik CO_2 indirgenme reaksiyonu için incelenmesi".

Table of Contents

List of Tables

List of Figures

Abbreviations

LUMO	: Lowest unoccupied molecular orbital
HOMO	: Highest occupied molecular orbital
XRD	: X-Ray Diffraction Spectroscopy
XPS	: X-ray Photoelectron Spectroscopy
FESEM	: Field Emission Scanning Electron Microscopy
UV-VIS	: Ultraviolet - visible
PEC	: Photoelectrochemical
SCE	: Standard calomel electrode
RPM	: Rounds per minute

Chapter 1: **Introduction**

1.1 Layered Perovskite Oxides

Perovskite oxides are inorganic molecules with the chemical formula of ABO_3, which is based on $CaTiO_3$, where A-type elements are usually in alkaline or rare earth groups, and B-type elements are from transition metals [1]. The structure consists of BO_6 octahedrons and 12 coordinated A cations, which can be seen in the Figure 1.1. below.

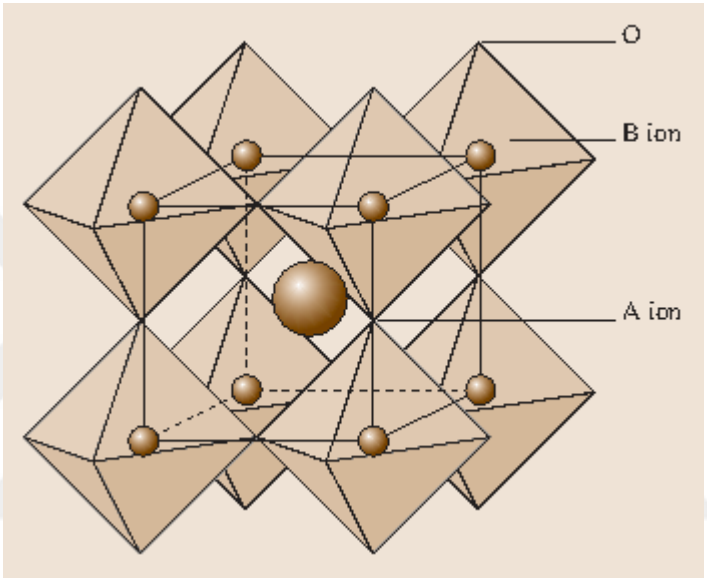

Figure 1.1. Illustration of cubic perovskite oxide structure [2]

Since perovskite oxides have ferro, piezo, and pyroelectrical properties, they are being used for many applications such as catalysis [3], fuel cells [4], and electrodes [5]. According to Tanaka and Misono, perovskite oxides have the following advantages:

- Various elements can be employed while the cell structure remains the same
- The bulk structure of perovskite can be characterized detailed; because of this reason, the surface of perovskites can be well estimated
- Stoichiometry, valency, and vacancies of perovskites can have various parameters
- There is much research about perovskites, which gives much information regarding their physical and solid-state chemical properties [6].

Even though the perovskite structure was introduced as ABO_3, this structure's derivates depend on their lattice plane parameters. For instance, ($A_{n+1}B_nO_{3n+3}$) has the layer of (111) plane, whereas ($A_nB_nO_{3n+2}$) structure has the layer of (110) plane [7].

There are three types of (100) layered perovskites, which are Ruddlesden-Popper phase ($A_{n+1}B_nO_{3n+1}$), Dion-Jacobson phase ($A'[A_{n-1}B_nO_{3n+1}]$), and Aurivillius phase (Bi_2O_2)($A_{n-1}B_nO_{3n+1}$). The detailed crystal structures illustrated below were shown in the Liu et al.'s publication [8].

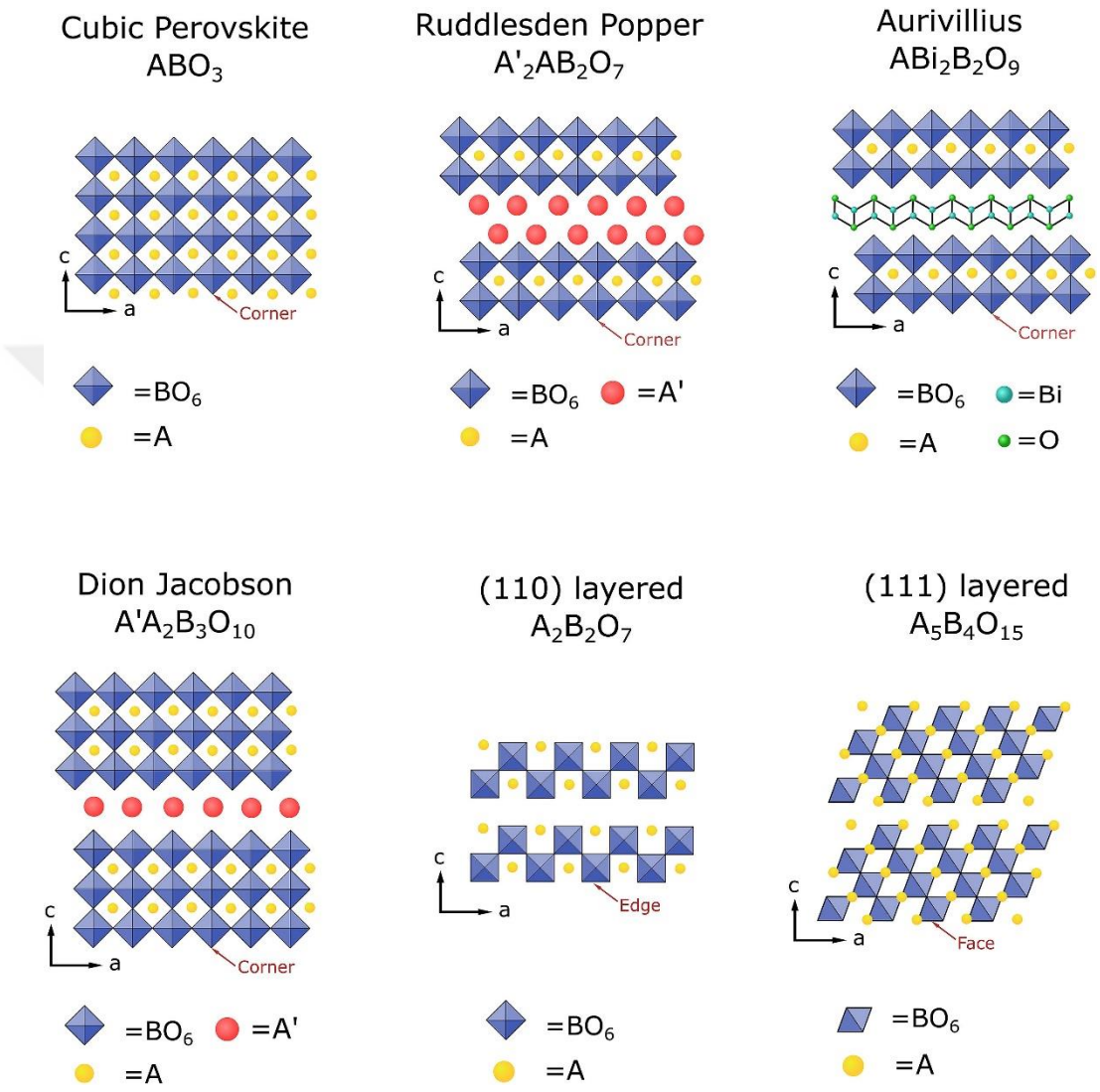

Figure 1.2. Crystal structures of different types of perovskite oxides

The layered perovskite oxides have similar applications as the cubic perovskite oxides. These applications include thermal catalysis [9], electrocatalysis [10], photocatalysis for water splitting [11], CO_2 reduction [12], and degradation of organic pollutants [13]. The layered perovskite oxides have advantages compared to the cubic perovskite oxides for the field of the photocatalysis [7]. Since the structure consists of negatively charged octahedrons and weakly bonded A-site cations, the A-site cations can

be easily removed, and the electronic properties can be altered easily. Proton exchange is a well-known method for this purpose [14]. The proton exchange procedure allows the removal of the A-site cations and replaces them with the H^+ cation. It is quite easy to accomplish this task due to the process being mixing the perovskite oxide with an acid solution and applying mechanical stimulation. Since the bulk material will lose its weakly bonded cations, layer separation is also possible. Because of this, the relative area will increase, and the activity of the catalyst will be affected. This procedure can be further improved to have 2D nanosheets of the perovskite oxides. Adding water-soluble large molecules with hydroxyl groups such as tetrabutylammonium hydroxide (TBAOH) will attach to the negatively charged layers of the perovskite oxide; then, it will create a steric hindering and separate the layers from each other [15]. In addition, the layered structure allows distortion of lattice parameters, which also impacts the electronic structure [16]. The distortion will affect the transportation and recombination of charge carriers [7].

1.2 Photocatalysis

The photocatalyst term is derived from the words “photo,” which comes from the photon, and “catalysis,” which is defined as a substance that increases the rate of the reaction without participating in it. The incoming light from an external source causes the activation of the photocatalyst by creating an electron flow out of the system. Since there is a requirement for an electron ejection from to system, the materials used for this purpose must not act as an insulator yet using entirely conducting materials will not allow electrons to have enough time to alter the reaction. Because of this reason, the proper candidates for photocatalytic applications are semiconductors.

The conductivity of a material is determined by the difference between the conduction band (LUMO) and the valence band (HOMO). The difference between these levels, known as bandgap (Eg), is defined as electronvolts (eV), and the three types of materials are specified as stated in the previous paragraph. According to their bandgap values, these three possible electronic states are

- Conductor, Band gap < 1.0 eV
- Semiconductor, Band gap < 1.5 – 3.0 eV
- Insulator, Band gap > 5.0 eV [17]

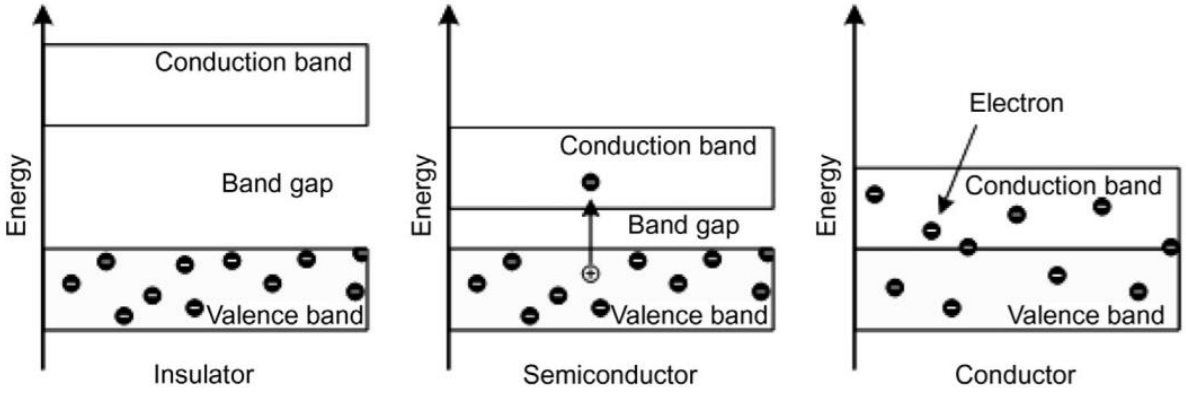

Figure 1.3. Types of conductivities [17]

The semiconductors work with the principle of ejection of an electron from a hole by incoming light due to photon energy carried with it. When the light illumination is sufficient to excite the electron and remove it from the valance band to the conduction band, the electrons and the holes are separated. Because of this reason, the electrons obtained from photocatalyst can be used for reduction, where the holes created can act as active sites. Therefore, they can be used for the oxidation processes.

It is also possible for both oxidation and reduction to take place during the photocatalytic process (redox reaction). Nevertheless, there might be any reaction due to bandgap divergences. In order for a reaction to occur, the energy levels must be inside the bandgap levels of the semiconductors. For instance, a semiconductor material with the valance band level at 0.5 eV and the conduction band level at 3.0 eV cannot perform a reduction reaction that will take place at 3.2 eV or an oxidation reaction at 0.4 eV. Because of this reason, the determination of the band levels has a crucial role in photocatalytic applications.

Another important aspect is the energy of the incoming light. If the energy is insufficient to excite the electron to leave its hole, the photon's energy must exceed the semiconductor's bandgap value. The photon's energy can be obtained from the "Planck Equation," where h indicates the Planck constant 6.625×10^{-34} Js, c is the velocity of the light, and the λ stands for the wavelength in nanometers. Since the energy of photon increases as the wavelength decreases, the smaller wavelengths in the UV region are more efficient for charge separation.

$$E = \frac{h*c}{\lambda} \quad (1)$$

1.3 Methods of Production of Efficient Photocatalytic Semiconductors

As was previously stated, the semiconductor's bandgap must be at specific levels, and the photon energy must be higher than the bandgap energy. Since many materials have specific band gaps for each, the photocatalyst must be designed for the specific process. Different methods can be employed in order to change the electronic structures, also known as bandgaps. In this section, the primary techniques for bandgap manipulation will be covered with a literature review specifically for perovskite oxides for water-splitting due to this dissertation being written for photocatalytic hydrogen production.

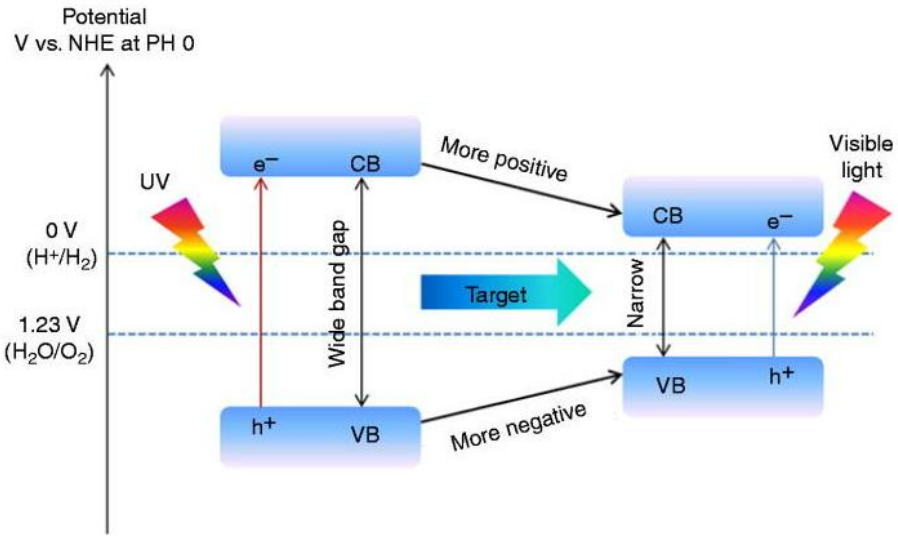

Figure 1.4. Illustration of band gap narrowing [18]

1.3.1 Doping

Doping can be described as introducing different elements to the system via a chemical reaction. Doping allows its user to change the semiconductor's bandgap to obtain a material that will have proper energy values for the specific application. For instance, Maeda introduced Rh to BaTiO3 perovskite oxide in order to decrease its bandgap for hydrogen evolution reaction [19]. However, excessive doping may also cause a change in energy levels of the bands, and therefore it may cause a decrease in the efficiency. Sun et al. introduced La and N elements to Sr_2TiO_4, and they found that the highest hydrogen evolution rate was achieved with $Sr_{1.8}La_{0.2}TiO_{4-y}N_y$ (x = 0.2). On the other hand, $Sr_{1.7}La_{0.3}TiO_{4-y}N_y$ (x = 0.3) was the best choice for having the highest oxygen production rate [11].

There are examples of doping that can be done using both anions and cations. The cations, which can also be classified as metals, in this case, cause the formation of an impurity band below the conduction band. According to the structure, it is possible to encounter many cations doping in the literature. Ma et al. used transition metals such as Ni, Cu, Fe, Mn, and Rh as dopants for $SrTiO_3$ [20]. Shimizu et al. worked on doping the $A_2SrTa_2O_7$ to demonstrate the effect of alkaline group elements on photocatalytic water splitting where A indicates H, Li, K, and Rb [21]. On the other hand, cation doping can also be used to increase the bandgap of a semiconductor. Mizoguchi et al. showed that the bandgap of the $BaSnO_3$, which is 3.1 eV, can be increased with doping Ca by replacing the Ba [22].

Anion doping has an impact on the bandgap due to it cause the formation of an energy level above the valence band which will lead to decreasing in the bandgap, which can be seen from fig; N, F, and chalcogens are known anions for doping procedure. The most preferred anion for doping is nitrogen. It is possible to encounter many examples of oxynitrides in the literature. Oxynitridization can be performed by treating the photocatalyst under NH_3 flow as it was done by Diot et al. [23], it can be done by mixing the semiconductor with amides [24], or it can be prepared with solid ammonia sources such as ammines and urea [25]. Fluorine can be doped to the structure by adding PVDF (polyvinylidene fluoride) and applying heat [26]. Qiu et al. used YF_3 instead of Y_2O_3 for doping fluorine to their material due to the electronegativity of the fluorine being higher than the oxygen. Thus, the fluorine inside the sample will be replaced by oxygen during the calcination process [27]. There are oxychalcogenides in the literature that supports the possibility of synthesizing chalcogen doped perovskite oxides. Charkin et al. synthesized Ca_2CuFeO_3S and Ca_2CuFeO_3Se by preparing pellets of precursors mixture. They placed these pellets inside a quartz tube and sealed it to keep the synthesis medium away from the air to ensure the samples did not get oxidized [28].

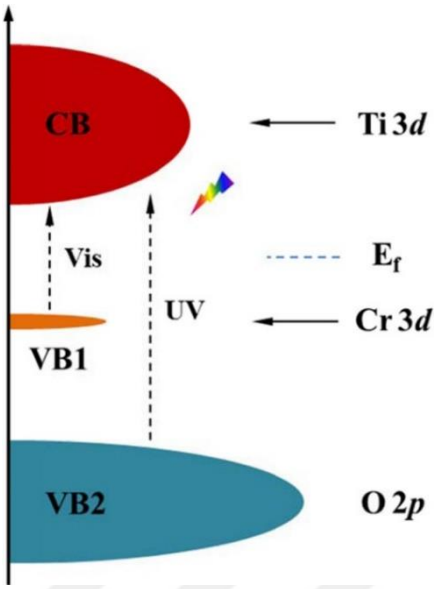

Figure 1.5. Formation of new energy levels [29]

There are also examples of co-doping in the literature. Co-doping enables the creation of two new levels of pseudo valance and conduction bands. Even though it is expected for this process the narrow the bandgap, it is also possible that the bandgap may remain the same according to the dopant preferred. In theory, it is also possible to create new levels above for both valance and conduction bands. Because of this reason, by employing the co-doping method, the bandgap may remain the same, yet the activity range can be altered. It should be considered that discussed method can only be relevant to a simultaneous anion and cation do-doping. When only cation or only anion co-doping is introduced to the system, only one band will remain the same where there will be new energy levels for the corresponding band. Some of the cation co-doping examples in the literature are La and Fe co-doping to Sr_2TiO_4 by Zhang et al. [30], and La and Rh co-doping to Sr_2TiO_4 by Sun et al. [31]. For photocatalytic hydrogen production. There are also cation and anion co-doping examples, as well. For instance, Kadari et al. doped Ag and N to $K_2Nd_2Ti_3O_{10}$ to increase its photocatalytic activity for pollutant degradation [32], where Jeyelakshmi et al. doped N, S and Fe to strontium titanates simultaneously by using urea or thiourea to inspect its effect on CO_2 reduction.

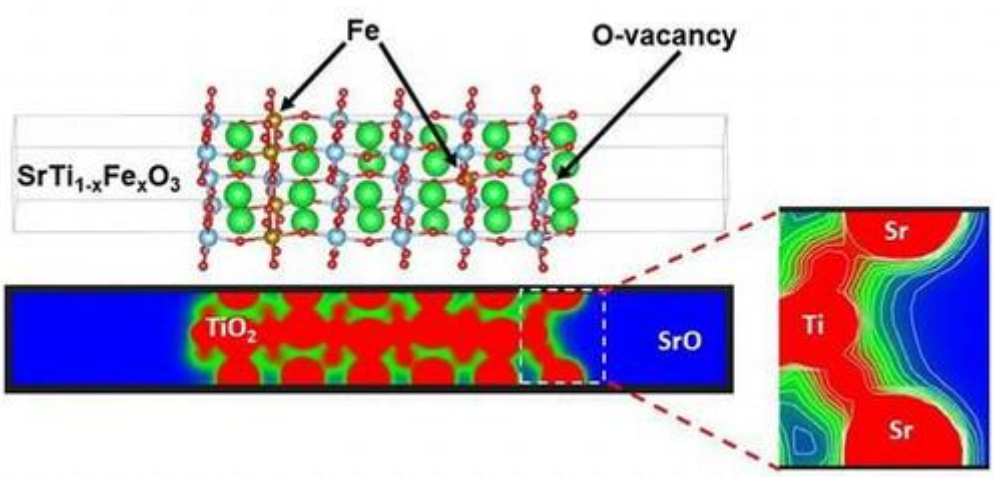

Figure 1.6. Effect of iron doping on oxygen vacancies [33]

Doping not only narrows the bandgap but also affects the charge carriers. Since doping affects the electronic properties of the semiconductors due to the creation of new energy levels and the formation of vacancies, vacancy formation takes place because of the introduction of different atoms to the structure, which has a lower charge than the substituted parent element. Staykov et al. conducted a study on iron-doped $SrTiO_3$ to see the effect of doping on surface reactivity [33]. Their research has shown that replacing Fe^{3+} atoms with Ti^{4+} atoms cause oxygen vacancies, which can be seen from the Figure 1.6, to compensate for the charge neutrality. These oxygen defects may play a crucial role in electron lifetime [34], and the prolonged lifetime of the electrons is connected to reducing electron-hole recombination [35,36]. The correlation of electron lifetime with photocatalytic hydrogen production can be seen from the Figure 1.7. According to the results of Yinxing et al., the addition of the fluorine to the system has surpassed the charge hole recombination and the electron lifetime was increased Figure 1.7a. Because of this reason, the photocatalytic activity and hydrogen production rates were increased (Figure 1.7b).

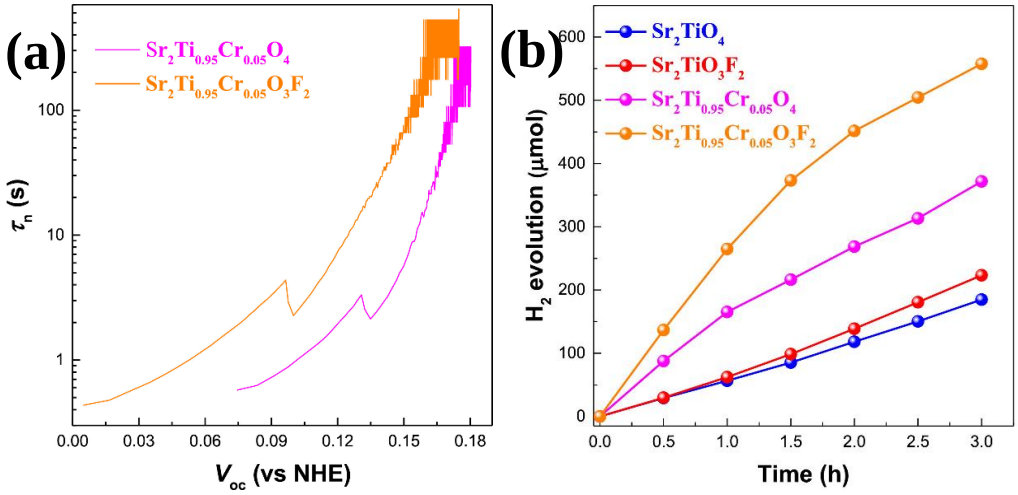

Figure 1.7. (a) Life-time measurement, (b) H_2 evolution graph for $Sr_2Ti_{0.95}Cr_{0.05}O_4$ and its fluorine doped derivatives [29]

1.3.2 Reduction

The positive effect of anion defect formation on lifetime was covered in the previous section. The anion defect may occur due to the charge neutrality. If a dopant with the same charge as the parent element, such as doping V^{4+} to Ti^{4+} like Bantawal et al. did in their research [37], it is possible to not to encounter anion defects. Reducing the semiconductor can create oxygen vacancies in a balanced system. For the reduction process of the perovskite oxide semiconductors, $NaBH_4$ is the most preferred reductant chemical due to it is a simple, quick and controllable process [38]. On the other hand, photocatalytic applications prepared with perovskite oxide semiconductors by using this reduction method are newly emerging, and it is needed to be investigated further.

1.3.3 Particle Shape Manipulation

The shape of the particles of a semiconductor plays an essential role in its photocatalytic activity. It will lead to surface heterojunction, which has advantages. The cost of building such a system is relatively lower than the two or more component systems, and redox potential loss is reduced [39]. For instance, Yu et al. worked on surface heterojunction of {001} and {101} facets of anatase TiO_2 by introducing different amounts of fluorine to manipulate the shape of the particles, and they found that the CH_4 production varies for each shape which can be seen from the Figure 1.8. [40].

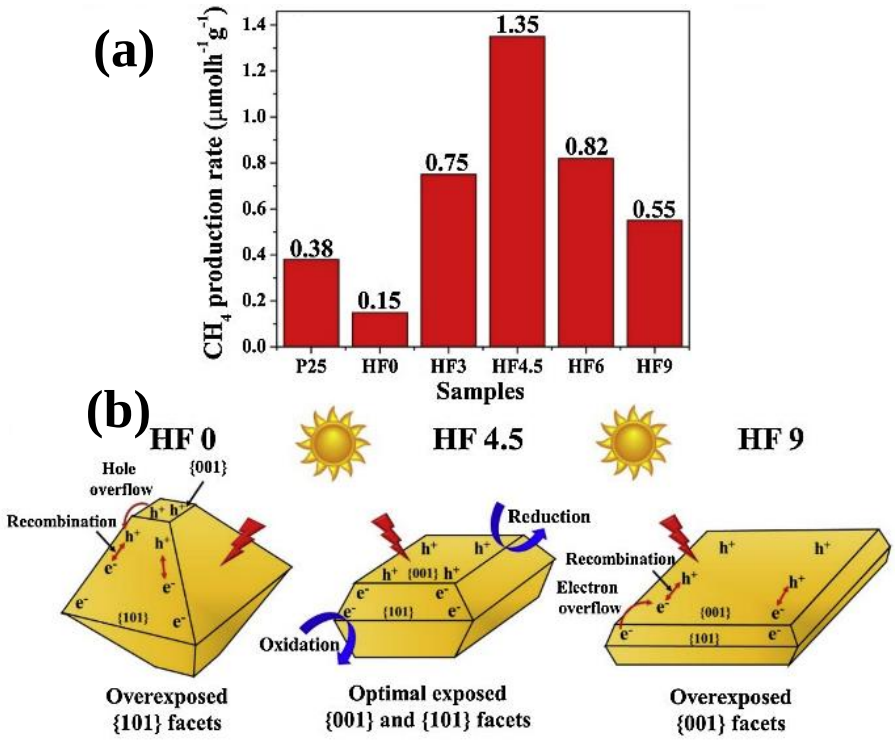

Figure 1.8. (a) Methane production rate of different TiO_2 morphologies, (b) Illustrations of different TiO_2 morphologies [40]

There are many ways to change the morphology of oxide semiconductors. Another work focused on hydrothermal synthesis demonstrates that the H_2 and CO_2 evolution rate differentiates for each particle shape, which Figure 1.9 shows was researched by Kimijima et al. [41]. In addition, the effect of ionic liquids on crystal engineering is a newly emerging topic in terms of shape manipulation. Mudring et al. worked on the ionic liquid-assisted sonochemical synthesis of $SrTiO_3$ [42] and $SrSnO_3$ [43]; their results indicated even the bandgap of the materials were affected. It should also be noted that the ionic liquids are because they Have different functional groups with a wide variety. Thus, the effect of ionic liquids on photocatalytic semiconductors may have a promising future.

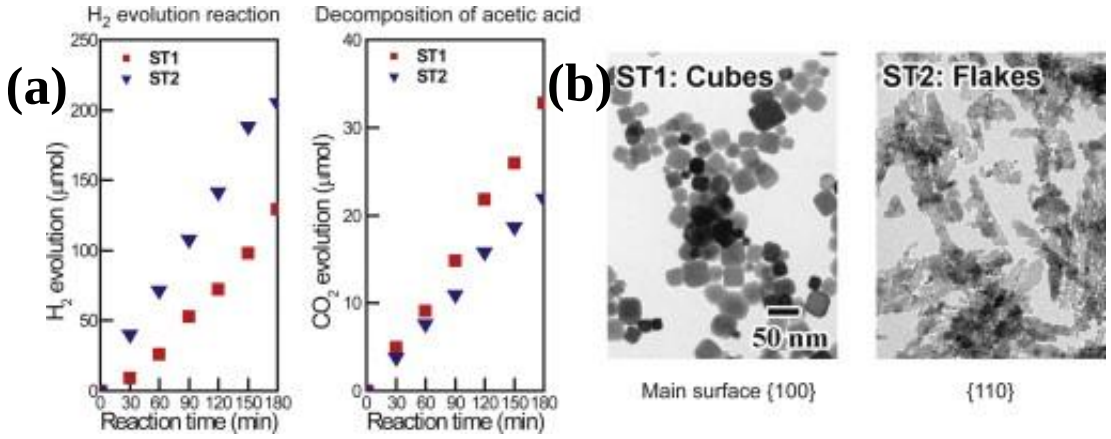

Figure 1.9. (a) H_2 evolution and CO_2 evolution rates, (b) SEM Images of different type of $SrTiO_3$ Structures [41]

1.3.4 Addition of Co-Catalyst

Most of the time, introducing co-catalysts into to system increases the efficiency of the reaction. The addition of co-catalysts promotes charge separation efficiency, lowers the activation energy of the formation of species, and co-catalyst nanoparticles act as active sites for the corresponding reaction [44]. The addition of the co-catalyst creates a depletion layer between the material and the co-catalyst, and the electric field provided by the co-catalyst promotes charge separation. It is also possible for the co-catalyst to have a negative impact because of the concentration of the co-catalyst [45]. The excessive amount of co-catalyst may block the incoming photons, thus leading to lower efficiency. Because of this reason, the amount of co-catalyst should be carefully chosen in order to have the optimum performance.

Since photocatalysts are used for different applications, the co-catalyst type varies. Generally, two types of co-catalyst are utilized for oxidation and reduction separately [46]. Yan et al. simultaneously loaded their sample with Pt–PdS/CdS photocatalyst for a water-splitting reaction. They found that using both co-catalysts caused very high apparent quantum efficiency (93% at 420 nm) [47].

Pt metal nanoparticles, which are created by the addition of $H_2PtCl_6.xH_2O$, are widely used for hydrogen production via water-splitting where CoO_x [48], PtO_x [49], and IrO_x [50] are used for photocatalytic oxygen production. The selectivity can be altered by using co-catalysts; because of this, the choice of co-catalyst is important for photocatalytic CO_2 reduction [51]. For instance, Hori investigated Cu for photocatalytic CO_2 reduction and

found that the Cu is a specific co-catalyst for this process because Cu increases adsorption of CO to the surface and promotes further reactions to obtain valuable chemicals [52].

1.4 Applications of Photocatalysts

As previously stated, the photocatalysts, which can also be addressed as light-sensitive current producing semiconductors, can be mainly utilized for CO_2 reduction to produce fuels such as CO, CH_4, CH_3OH, for pollutant degradation, and for water splitting to produce hydrogen or oxygen. In this part of the dissertation, examples of such applications will be explained, and current development will be discussed.

1.4.1 Photocatalytic Carbon Dioxide Reduction (or Fuel Production)

The photocatalytic CO_2 reduction can be described as artificial photosynthesis due to CO_2being reduced for the synthesis of valuable chemicals such as methanol, methane, and formic acid. The working principle stems from the bandgap part, as stated in chapter 1.2. When a photon with sufficient energy has higher energy than the semiconductor's bandgap, the electrons and the holes are formed on the surface of the material due to the electrons in the conduction band moving to the valence band. These electrons and holes are used to reduce CO_2 and oxidation of water accordingly. The Figure 1.10 exhibits the proposed mechanism for CO_2 reduction.

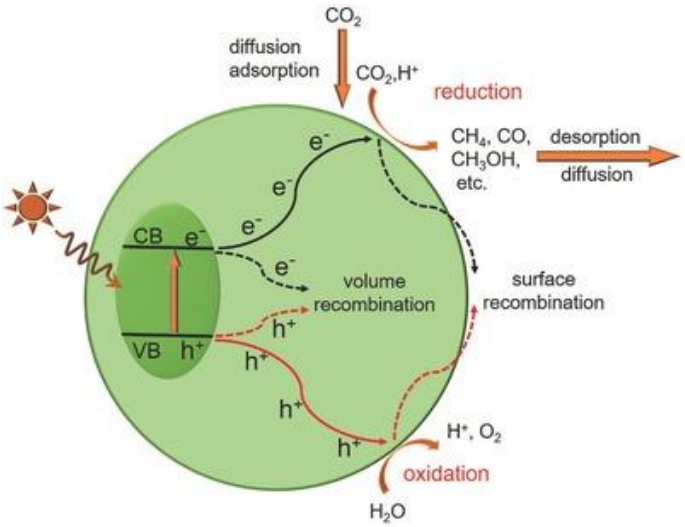

Figure 1.10. Illustration of the CO_2 reduction mechanism on a photocatalyst [53]

The material's bandgap also plays a crucial role in the CO_2 reduction process. The bandgap values must be lower to utilize the visible light spectrum. On the other hand, the positions of both valance and conduction bands are essential parameters. If desired reactions are not between the bandgap levels, the reaction will not occur. The Figure 1.11 shows the formation of CO, H_2CO, CH_3OH, and CH_4 using a perovskite oxide semiconductor. Also, possible detailed reactions are available in the Table 1.1.

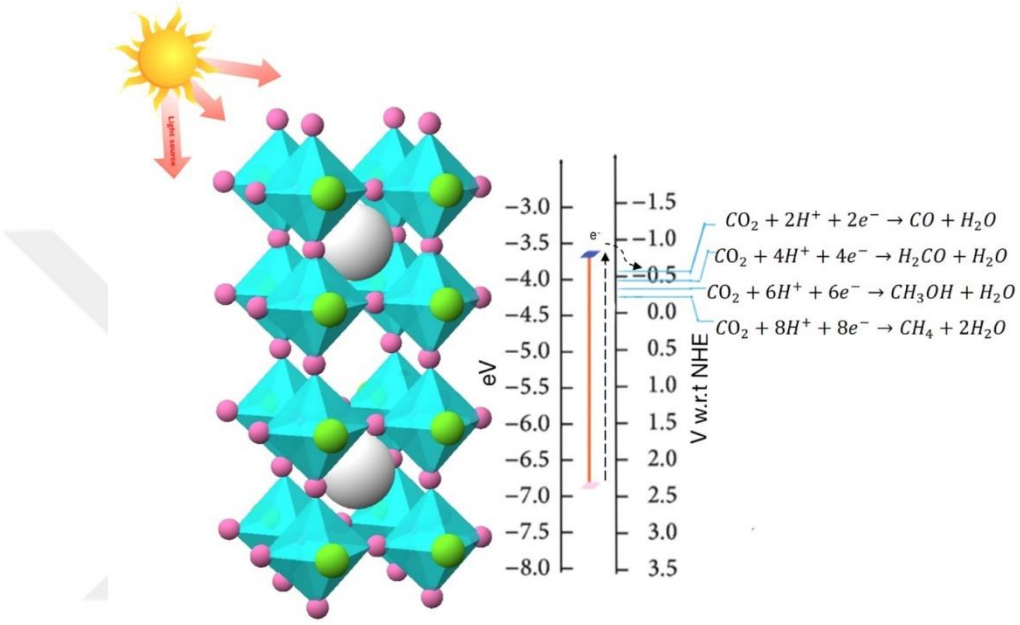

Figure 1.11. Illustration of reduction potentials of CO_2 based fuels [54]

The semiconductor's bandgap in proper oxidation and reduction is not only the single challenge for the photocatalytic CO_2 reduction process. Another issue arises from the adsorption of CO_2 to the semiconductor. Since the CO_2 is an acidic molecule, using basic sorbents or applying alkaline modification will cause chemisorption, and thus intermediate species (for instance, bidentate carbon dioxide) will form [39]. Luévano Hipólito and Torres-Martínez utilized this phenomenon, and they investigated the CO_2 reduction efficiency of alkaline niobates [56].

Another critical factor that should be considered for CO_2 reduction is the presence of carbonaceous residues on catalyst [57]. These molecules may also be affected by the redox reaction. Therefore, they may cause the formation of extra smaller molecules such as CO and CH_4, which may cause an overestimation of catalytic activity [58].

Product	Reaction	E^0redox[a] (V versus NHE)
Oxygen	$H_2O \rightarrow ½O_2 + 2H^+ + 2e^-$	+0.82
Methane	$CO_2 + 8H^+ + 8e^- \rightarrow CH_4 + 2H_2O$	−0.24
Ethane	$2CO_2 + 14H^+ + 14e^- \rightarrow C_2H_6 + 4H_2O$	−0.27
Carbon monoxide	$CO_2 + 2H^+ + 2e^- \rightarrow CO + H_2O$	−0.51
Methanol	$CO_2 + 6H^+ + 6e^- \rightarrow CH_3OH + H_2O$	−0.39
Ethanol	$2CO_2 + 12H^+ + 12e^- \rightarrow C_2H_5OH + 3H_2O$	−0.33
1-Propanol	$3CO_2 + 18H^+ + 18e^- \rightarrow CH_3CH_2CH_2OH + 5H_2O$	−0.31
2-Propanol	$3CO_2 + 18H^+ + 18e^- \rightarrow CH_3CH(OH)CH_3 + 5H_2O$	−0.30
Formaldehyde	$CO_2 + 4H^+ + 4e^- \rightarrow HCHO + H_2O$	−0.55
Acetaldehyde	$2CO_2 + 10H^+ + 10e^- \rightarrow CH_3CHO + 3H_2O$	−0.36
Propionaldehyde	$3CO_2 + 16H^+ + 16e^- \rightarrow CH_3CH_2CHO + 5H_2O$	−0.32
Acetone	$3CO_2 + 16H^+ + 16e^- \rightarrow CH_3COCH_3 + 5H_2O$	−0.31
Formic acid	$CO_2 + 2H^+ + 2e^- \rightarrow HCOOH$	−0.58
Acetic acid	$2CO_2 + 8H^+ + 8e^- \rightarrow CH_3COOH + 2H_2O$	−0.31

Table 1.1. Redox potentials of CO_2 based compounds [55]

1.4.2 Photocatalytic Degradation of Pollutants

The constantly increasing population of the Earth creates a demand for various objects, which requires mass production and improvement of industrial systems. While the making of products continues, organic pollutants are produced as undesired side-products. The contamination caused by these organic pollutants primarily affects the

water supplies; removing the pollutants is considered an essential solution for the water shortage [59]. An environmentally friendly approach for this issue is using the photocatalyst due to their light-driven redox abilities [60]. The organic pollutants, which correspond to toxic but degradable compounds, include toxic organic chemicals such as dyes, drugs, or pesticides.

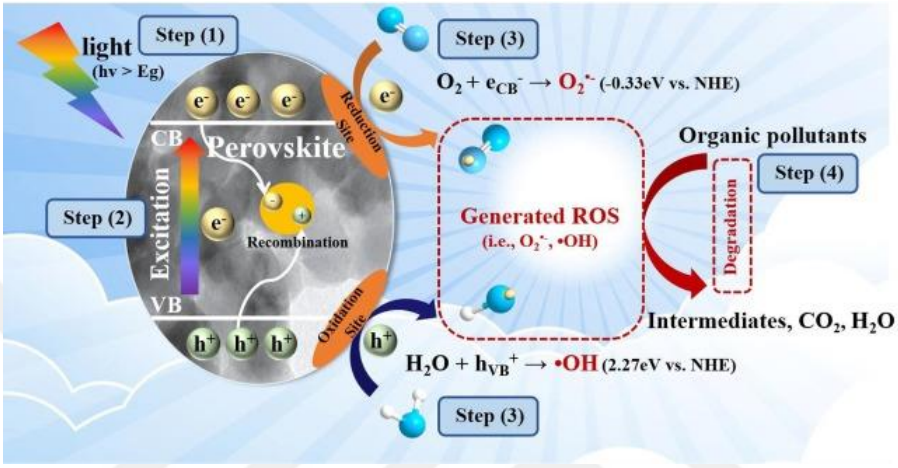

Figure 1.12. Illustration of the pollutant degradation mechanism on a photocatalyst [61]

The photocatalytic activity, which is shown on the Figure 1.12, takes place via the formation of charged carriers due to the illumination. The mechanism is identical to the CO_2 reduction, yet this time reduction and oxidation sites are used to form redox oxidative species for pollutant degradation [61].The photogenerated holes can participate in the degradation reaction [13]. Specifically, redox oxidative species are the essential compounds for this process [62,63]. When this information is considered, the possible degradation mechanism can be seen from the Equation 2 and Equation 3 below.

$$h^+ + Pollutants \rightarrow Intermediates, CO_2, H_2O, etc. \quad (2)$$

$$O_2^- \bullet or \bullet OH + Pollutants \rightarrow Intermediates, CO_2, H_2O, etc. \quad (3)$$

The bandgap of the photocatalyst should include the formation of free radicals' redox potentials to have the best outcome. However, since $O_2^- \bullet$ formation redox potential is relatively high, it is hard to achieve this reaction [64]. In addition, prolonging the lifetime of the charge carriers by decreasing the recombination rate has a positive impact on degradation efficiency, as expected. Thus, the methods of efficient

photocatalysis production could be used for bandgap engineering. As a bandgap-altering method, which is doping, Fei et al. used $CeCo_{0.05}Ti_{0.95}O_{3.97}$ for photodegradation of the aqueous Nile blue [65]. Also, there are examples of morphology manipulation. Su et al. synthesized porous $LaFeO_3$ for rhodamine B photodegradation [66], and Dong et al. found that the nanofibers of $LaFeO_3$ have better photodegradation activity comparing to the regular bulky structure [67]. They found that the surface area is enhanced by using a silica template and removing the template from the structure.

1.4.3 Photocatalytic Water Splitting

For photocatalytic water splitting, the semiconductor's bandgap should be above 1.23 eV. The electrons (e^-) and holes (h^+) accumulated from the photo-excitation process, and each of them is used for a different purpose. The electrons are used for reduction (hydrogen production), whereas the holes are used for oxidation (oxygen production). The conduction band value for the photocatalyst must be lower than the reduction potential of the water for the H_2 production, where the valence band of the photocatalyst must be higher than the oxidation potential of the water so that O_2 can be produced. [18] Figure 1.13 shows the suggested mechanism for the water-splitting process.

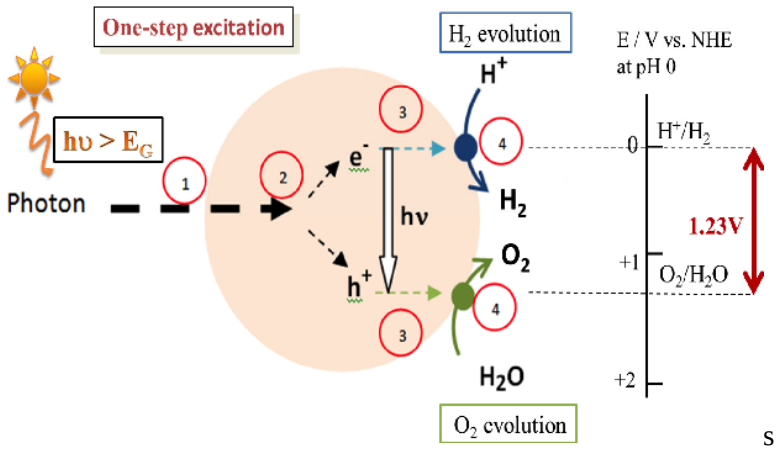

Figure 1.13. Schematic demonstration of water splitting process [68]

Under normal circumstances the overall water splitting reaction can be described as follows:

$$4H^+ + 4e^- \rightarrow 2H_2 \quad (4)$$

$$2H_2O + 4h^+ \rightarrow 4H^+ + O_2 \quad (5)$$

However, there may be some cases where the reduction or the oxidation process cannot take place due to the position of the valance and the conduction bands may not be in the range of water splitting potentials. If this is the occurrence, then a sacrificial agent must be used in order to achieve the preferred reaction. For instance, methanol (CH_3OH) is a commonly used sacrificial reagent for photocatalytic hydrogen production. There are also other sacrificial reagents in the literature such as ethanol (C_2H_5OH) [69], triethanolamine (TEOA) [70], sodium sulfide (Na_2S) [71]. Sacrificial reagents affect the reaction mechanism, as well. According to Kumaravel et al., using methanol as the sacrificial reagent will yield the given reaction below [72]:

$$H_2O + h^+ \rightarrow H^+ + OH^- \quad (6)$$

$$CH_3OH + OH^- \rightarrow H_2O + (CH_2OH)^- \quad (7)$$

$$(CH_2OH)^- \rightarrow HCHO + H^+ + e^- \quad (8)$$

$$2H^+ + 2e^- \rightarrow H_2 \quad (9)$$

$$HCHO + H_2O \rightarrow HCOOH + H_2 \quad (10)$$

$$HCOOH \rightarrow CO_2 + H_2 \quad (11)$$

Overall:

$$CH_3OH + H_2O \rightarrow CO_2 + 3H_2 \quad (12)$$

There are also sacrificial electron acceptors for photocatalytic oxygen production. However, there are a few examples of oxygen production sacrificial reagents, and the most used one is silver (Ag). There is also a study that shows that the iron (Fe) ions [73] and peroxodisulfate ($S_2O_8^{2-}$) [74] can be used for water oxidation sacrificial agents. The suggested mechanism for water oxidation with silver is as follows [75]:

$$2H_2O + 4h^+ \rightarrow 4H^+ + O_2 \quad (13)$$

$$4e^- + 4Ag^+ \rightarrow 4Ag \quad (14)$$

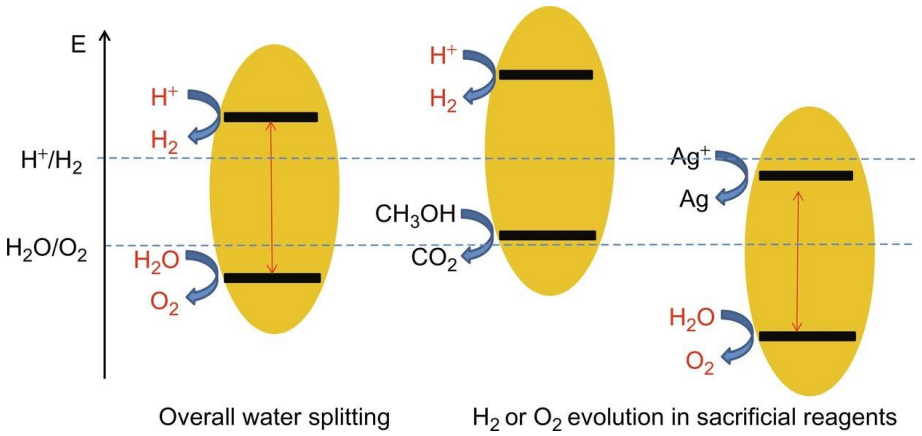

Figure 1.14. Illustration of sacrificial agents use in water-splitting redox reactions [44]

There are many examples of photocatalytic water splitting for hydrogen and oxygen production. Due to the nature of this dissertation, the perovskite oxides will be evaluated for this purpose. For regular ABO_3 type of perovskites, there are examples of $NaTaO_3$ [76], $KNbO_3$ [77], $NaNbO_3$ [78], $BiFeO_3$ [79], $BaZrO_3$ [80], $SrSnO_3$ [81], $LaCoO_3$ [82], and $LaNiO_3$ [83]. It should also be noted that there are derivates of these materials with enhanced performance in terms of hydrogen or oxygen production, with the methods of improvement covered in the first section of this chapter.

The layered perovskites with different structures are also known for their photocatalytic water splitting application. The Table 1.2, Table 1.3, and Table 1.4 exhibit some of the layered perovskite oxides that are tested for photocatalytic water splitting.

				Activity ($\mu mol\ g^{-1}h^{-1}$)		
Chemical Formula	**Band gap (eV)**	**Solution**	**Co-catalyst**	**H_2**	**O_2**	**Ref.**
$H_2SrTa_2O_7.nH_2O$	3.9	Water		770	358	[21]
$H_{1.81}Sr_{0.81}Bi_{0.19}Ta_2O_7$	3.64	Water		2460	1100	[84]
$K_2La_2Ti_3O_{10}$		0.1 M KOH		2186	1131	[85]
Sr_2SnO_4		Water	RuO_2 1%	4	2	[86]
$Na_2Ca_2Nb_4O_{13}$	3.3	20% MeOH	Pt 1%	1355		[87]
Rh / Ln doped $Ca_3Ti_2O_7$		10% MeOH	Pt 1%	3.3		[88]
$H_2La_{2/3}Ta_2O_7$	4.0	Water		158	77	[89]
$Sr_3Ti_2O_7$	3.2	Water	NiO 3%	144	72	[90]
$Sr_4Ti_3O_{10}$	3.2	Water	NiO 3%	170		[91]
$A_2La_2Ti_3O_{10}$ (A = K, Rb, Cs)	3.4 – 3.5	Water		869	430	[92]

Table 1.2. Layered Ruddlesden-Popper perovskite oxides for photocatalytic water splitting process

				Activity (μmol $g^{-1}h^{-1}$)		
Chemical Formula	**Band gap (eV)**	**Solution**	**Co-catalyst**	**H_2**	**O_2**	**Ref.**
Bi_2WO_6	2.8	5.4% MeOH	Pt 1%	1.6	34	[93]
Bi_2MoO_6	3.0	0.05 M AgNO3		0.01	2.1	[94]
$Bi_2Mo_2O_9$	3.1	0.05 M AgNO3			3.6	[94]
$Bi_2Mo_3O_{12}$	2.88	0.05 M AgNO3			15.2	[94]
$PbBi_2Nb_2O_9$	2.88	30% MeOH - 0.05 M AgNO3	Pt 1%	7.6	520	[95]
$ALa_4Ti_4O_{15}$ A= Ca, Sr, Ba	3.8 - 3.9	Water/CO2	Ag	363	168	[96]
$Bi_4Ti_3O_{12}$	3.1	5% MeOH	Pt 1%	0.6	3.0	[93]
$K_{0.5}La_{0.5}Bi_2M_2O_9$ (M = Ta, Nb)	3.4	Water		2.95	17	[97]

Table 1.3. Layered Aurivillius perovskite oxides for photocatalytic water splitting process

				Activity ($\mu mol\ g^{-1}h^{-1}$)		
Chemical Formula	**Band gap (eV)**	**Solution**	**Co-catalyst**	**H_2**	**O_2**	**Ref.**
$RbNdTa_2O_7$	3.8	Water		234.8	126.4	[98]
N doped $CsCa_2Ta_3O_{10}$	2.0	0.01M AgNO3			21.6	[99]
$HSr_2Nb_3O_{10}$	3.3	1M 2-propanol	Pt 0.3%	900		[100]
$KCa_2Nb_3O_{10}$		10% MeOH	Pt 1%	5500		[101]
$AgLaNb_2O_7$	2.98	20% MeOH	Pt 1.0%	2102		[102]
$HLaNb_2O_7$	3.9 - 4.2	10% MeOH	Pt	4800		[103]
$ASr_2Ta_xNb_{3-x}O_{10}$ (A = K, H)	3.3 - 4.3	10% MeOH	Pt	9300		[104]
Ag/$RbLaNb_2O_7$, $RbA_2Nb_3O_{10}$	2.4 - 3.7	20% MeOH	0.1% Pt	13616		[105]

Table 1.4. Layered Dion-Jacobson perovskite oxides for photocatalytic water splitting process

Chapter 2: **Photocatalytic Hydrogen Evolution from Copper and Nitrogen Doped Layered Strontium Titanate**

2.1 Introduction

Hydrogen production via light-driven methods is a promising ongoing research topic. Because of this reason, it is possible to find many examples of it in the literature with different materials [106]. Among these materials, titanates are preferable due to their relatively cheaper production precursors and non-toxicity. The most basic type of titanate, which is TiO_2, as a result of its basic molecular formula, is used widely for water-splitting applications [107]. Fujishima and Honda investigated TiO_2 as photoelectrochemical material as a pioneer [108], and their findings promoted the attention toward this material. Even though TiO_2 has the photocatalytic feature, it also has the drawback of rapid recombination of charge carriers, which negatively impacts efficiency [109]. Since the rapid recombination creates a problem due to charge carriers and holes recombining and causes the decreasing period of free electron lifespan, the scientists wanted to overcome this issue. They approached this issue with a solution of doping the TiO_2 with different elements [110], using it in heterojunction systems [111], and investigating efficiency outcomes of different crystal types such as anatase and rutile [112].

Since TiO_2 has limitations due to its simple structure, the perovskite derivates also drew attention. Among these types of materials, $SrTiO_3$ is known for its photochemical susceptibility [113]. The bandgap of the $SrTiO_3$, which is 3.25 eV [114], is suitable for the photoelectrochemical hydrogen production process. Nevertheless, the large bandgap of the material causes it to absorb only the UV region of the light spectrum. The researchers worked on this material as previously stated for TiO_2, and they achieved changing the bandgap of the material [115–117]. Since TiO_2 and $SrTiO_3$ have a promising future for the photoelectrochemical hydrogen production process, Sr_2TiO_4 (Figure 2.1 below) is also a noteworthy candidate due to its semiconductor nature with a bandgap of 3.5 eV [118]. However, the broad bandgap issue continues with this Ruddlesden-Popper type layered perovskite as it was happening with the other titanates. The Ruddlesden-Popper structure allows Sr_2TiO_4 to have a layered structure which is going to have a positive impact on hydrogen production rates due to the (001) SrO-ended surface in rock-

salt layer allows a barrier-free water dissociation while the active apical oxygen site in perovskite layer promotes hydrogen adsorption and evolution [119].

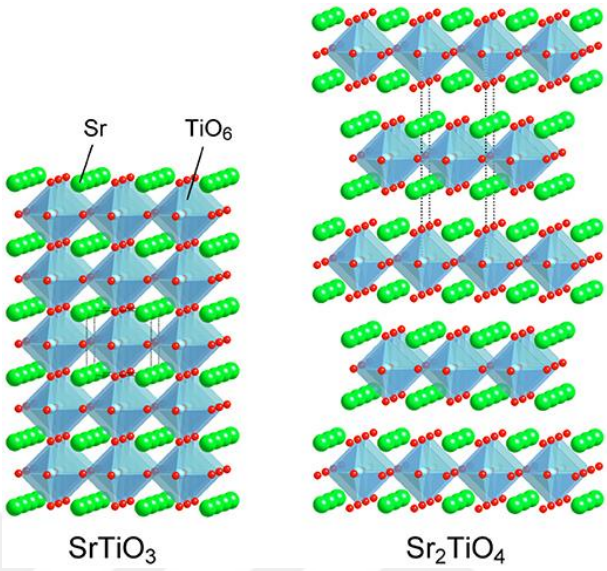

Figure 2.1. Crystal structures of $SrTiO_3$ (left) and Sr_2TiO_4 (right) [120]

Interest in Sr_2TiO_4 also has researchers try to change the electronic structure, ergo the material's bandgap. A distinctive approach to this purpose was substituting cations and anions with different elements [30,31,118,119,121,122]. Specifically, doping the structure with different anions impacts the absorbance capability of the materials. For the anion part, nitrogen [11] and fluorine [29] doping is known methods for enhancing the photoelectrochemical hydrogen production rates. Nitrogen doping allows the material to absorb in the visible region. Thus, it leads materials to work with the visible spectrum of light. Copper is a known cation for its ability to create recombination centers. It has a 2.7 eV conduction band value lower than the conduction band of pristine Sr_2TiO_4; therefore, it leads to the formation of recombination centers and has a positive impact on photocatalytic hydrogen production [20]

By utilizing copper and nitrogen co-doping, the photocatalytic activity for the hydrogen production of Sr_2TiO_4 can be enhanced in the visible range. In this part of the dissertation, the effects of these dopants are inspected with different combinations to give insight into the photocatalytic hydrogen production via this material. The samples were prepared as pristine, only nitrogen-doped, only copper-doped, and co-doped to discuss this subject. The photocatalytic hydrogen production experiments were performed under the full-range spectrum, also under the “perfect light” by using AM 1.5 filter. By doing

so, the sunlight was replicated, and the photocatalytic activities of these specimens were recorded. Since doping the material with Cu is relatively cheaper than using a co-catalyst such as Pt, samples were inspected without the co-catalyst addition.

2.2 Experimental Section

2.2.1 Materials and Synthesis

Since the chemicals used for this synthesis were purchased in analytical grade, the reagents were not further purified. 8.0 mmol of Sr_2TiO_4 desired to be synthesized with the Pechini method. Stoichiometry of the Sr_2TiO_4 indicates a 2:1 molar ratio of Sr:Ti. Therefore, 8.0 mmol $Sr(NO_3)_2$ (Sigma, ≥99.0%) and 4.0 mmol of Titanium isopropoxide (Aldrich, TYZOR® organic titanate, 97%) were used as the primary synthesis materials. As it was stated earlier, ethylene glycol (Merck, EMPLURA) and citric acid (Bioultra, anhydrous, ≥99.5%) were used as a solvent and chelating agent for further esterification and polymerization reactions. For the preparation of 4.0 mmol of Sr_2TiO_4, 1.18 mL of titanium isopropoxide was added dropwise onto 25.0 mL of ice-cold ethylene glycol while vigorously stirred. The solution was observed if there is any white precipitation of TiO_2, which may be formed due to its sensitive nature to humidity, to add the citric acid into the solution. After making sure that there was no precipitation, 14.96 g of citric acid was added to the solution, and the temperature of the solution was set to 65 °C to dissolve the citric acid completely. 1.69 g of $Sr(NO_3)_2$ was dissolved in another beaker with 14.68 mL of ice-cold distilled water while the citric acid was dissolving. When the citric acid was dissolved in the main beaker, $Sr(NO_3)_2$ solution was added dropwise into the first beaker. After adding the $Sr(NO_3)_2$ solution, the heater's temperature was set to 115 °C, and the mixture was polymerized to have a gel. When the color of the gel turned reddish dark brown, the gel was placed into a furnace (Protherm PLF 150/15) at 400 °C for 1 hour with a heating rate of 5 °C per minute. Next, charred remains of the sample were put into agate mortar, and it was mixed and ground for 30 minutes to homogenize the sample. The ground sample was placed into an alumina crucible, and the crucible was placed into the furnace, and it was heated at 550 °C for 5 hours with a heating rate of 5 °C per minute. Finally, the precursor was pelletized using a hydraulic press (Specac Hydraulic Press) under 5 tons of pressure, and the obtained pellet was calcined in a furnace at 1100 °C for 5 hours.

For the Cu dopped Sr_2TiO_4, the stoichiometry of the copper was chosen as 0.05 % in moles. The appropriate amount of copper (II) acetate (Alfa-Aesar, anhydrous, 98%) was added together with $Sr(NO_3)_2$ in 14.68 mL of ice-cold distilled water then added to the Titanium isopropoxide and citric acid in 25 mL of ethylene glycol solution in the synthesis step to form $Sr_2Ti_{0.95}Cu_{0.05}O_4$. Next, the ammonolysis procedure was performed for nitrogen doping at 750 °C for 5 hours with a heating rate of 7 °C per minute for both pristine and copper doped samples [123]. Finally, the samples with elemental compositions of $Sr_2TiO_{4-x}N_x$ and $Sr_2Cu_{0.05}Ti_{0.95}O_{4-x}N_x$ were obtained.

2.2.2 Structural Analysis

The crystal structure of samples was analyzed using Bruker D8 Advance X-Ray Diffractometer between 2θ values of 10° to 70° using Cu Kα radiation (λ=1.5406 Å). Zeiss Ultra Plus field emission scanning device is used for FESEM images. The magnification ratio was 20,000 and 100,000. Secondary electron and In-lens detectors were used for imaging. 5.00 kV accelerating voltage and working distances between 5.4 to 5.8 mm were preferred under ultra-vacuum. Thermo Scientific K-Alpha Spectrometer with Al Kα (1486.6 eV) source was used for the XPS analysis. The XPS data acquired was deconvoluted using Thermo Avantage v5.973. All XPS spectra were corrected for any shift as a result of charging according to C1s at 284.5 eV. Shimadzu UV-3600 UV-VIS-NIR Spectrophotometer was used for UV-VIS measurements between 200 to 800 nm wavelengths. The measurements were performed using diffuse reflectance spectra, and the results were transformed into absorbance spectra using the Kubelka-Munk function.

2.2.3 Photoelectrochemical Analysis

Fluorine-doped tin oxide (FTO) coated glasses with 25 x 10 mm dimensions were used as electrodes. These FTO-coated electrodes were cleaned with a mixture of distilled water and ethanol in an ultrasonic bath. All films from samples for photoelectrochemical characterization were prepared by the electrophoretic deposition technique. 40 mg of sample powder and 10 mg of Iodine (Sigma-Aldrich, 99.8% ACS reagent) were mixed into 50 mL of acetone in a beaker. Then, the beaker was placed into an ultrasonic bath for 15 minutes. FTO-coated glasses were dipped into the solution, and they were coated via

electrophoretic deposition at 40 V potential for 30 seconds by using a DC power source (RIGOL DP811). Finally, these electrodes were heated to 400 °C for an hour with a heating rate of 5 °C per minute to improve adhesion to the surface of the FTO-coated glass. A working electrode (sample coated on FTO glass), Pt foil 10 x 10 mm as the counter, and the saturated calomel electrode (SCE) as the reference electrode in the solution of 0.5 M K_2SO_4 with 0.02 points per second scan rate at 1.2 V were used for photoelectrochemical characterizations. The light illumination was provided using a 500 W xenon light source (Newport, 66901). The thin films were also used for Mott Schottky analysis between -1.6 to 0 V at 1000 Hz. The measurements were done using a potentiostat (Princeton Applied Research VersaSTAT MC).

2.2.4 Photocatalytic Hydrogen Production

For the hydrogen production experiment, 30 mg of sample powder and 15 mL of the methanol-water mixture (10% volume MeOH) were placed into a quartz vessel with a total volume of 25 mL with a rubber stopper. Then, the air inside the vessel was removed by purging the vessel via argon for 30 minutes. Next, another stopper was placed on the vessel with an outlet, and the argon flow was introduced between the two stoppers to inhibit air contamination. The vessel illuminated horizontally using a 500 W xenon light source (Newport, 66901) equipped with and without AM 1.5 filter and it was stirred with a speed of 200 rpm. The hydrogen amount inside the vessel was determined using a gas chromatogram (Shimadzu, GC-2014) using a 100 μL gas-tight syringe. The inlet temperature was 150 °C, the temperature of the MS 5A column (Teknokroma, NF-38427-FS) was 75 °C, and the temperature of the thermal conductivity detector (TCD) was 150 °C with a bridge current of 40 mA. The ideal gas equation was used for the calculation of hydrogen production amount, where it was accepted as 1.0 mol of gas occupying 22.4 L of volume. The headspace volume was 10 mL, and the intensities of the GC peaks were determined according to the calibration line that was made with different volumes of hydrogen gas.

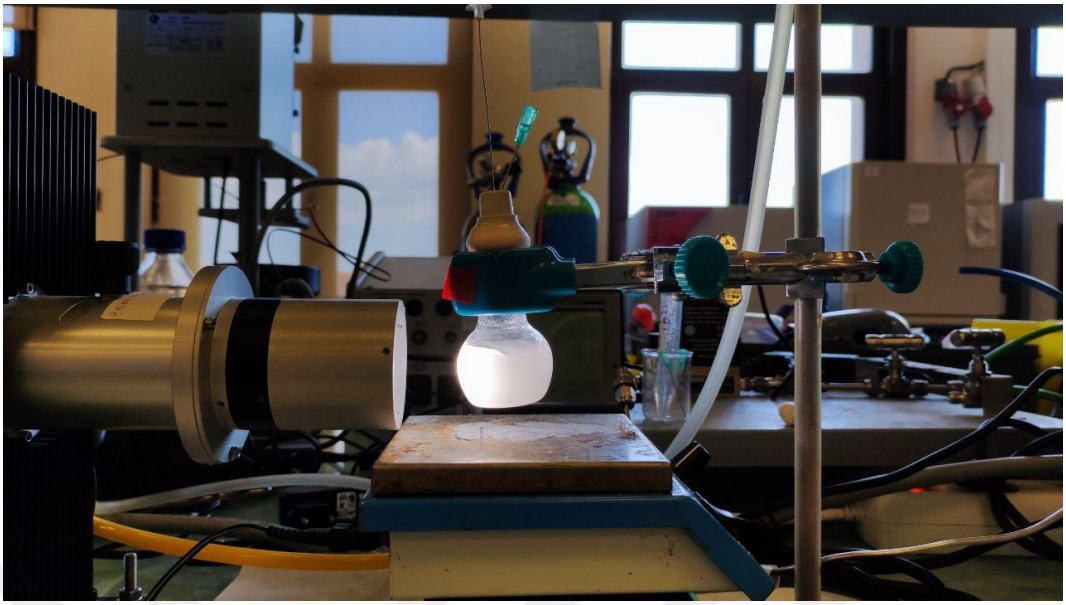

Figure 2.2. Experimental setup

2.3 Results and Discussion

2.3.1 X-Ray Diffraction Spectroscopy (XRD)

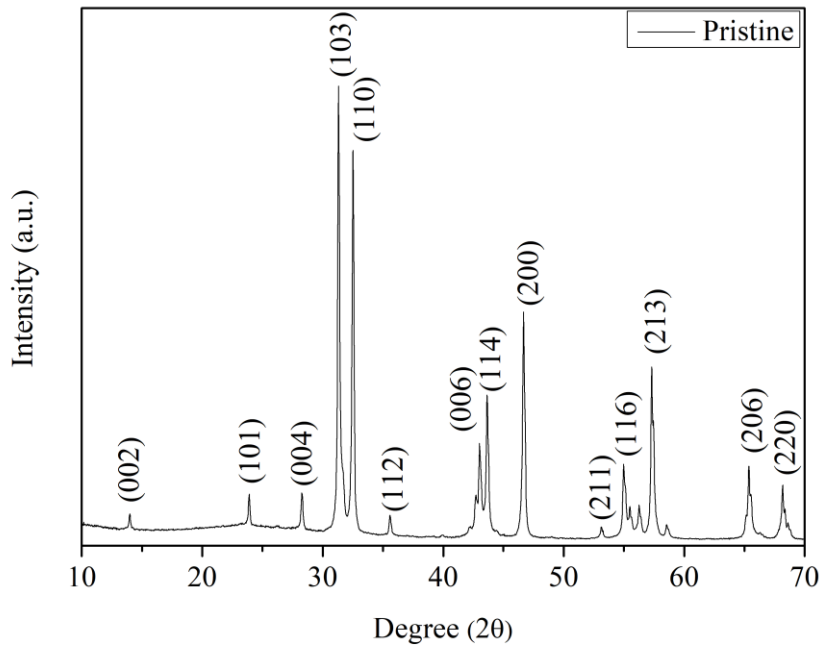

Figure 2.3. XRD pattern with planes of the pristine Sr_2TiO_4.

The Sr_2TiO_4 has a tetragonal structure with a group number of I4mm. The planes of the structure are shown in the Figure 2.3. XRD patterns of doped samples are identical to the pristine materials, which can be seen from Figure 2.4. These results indicate that the structural integrity remains preserved. The shift to the smaller 2θ values by doping copper into the structure, in order to see the effect of the doping on to sample, can be observed in Figure 2.5. The ionic radius of Ti^{4+}, which has the coordination number of 6, is 74.5 pm. In contrast, the ionic radius of Cu^{2+} is 87.0 pm, and the ionic radius of Cu^{+} is 91.0 pm for a coordination number of 6 [124]. Since the ionic radiuses of both copper variants are larger than the ionic radius of the titanium, the interplanar spacing increases, which leads to a shift of the (103) peak between 31.0 to 31.6 2θ degrees. Because of this reason, it can be stated that the copper was successfully doped to the structure. Figure 2.5 also shows the effect of nitrogen doping on the XRD patterns. Pristine and nitrogen-doped sample, with or without the addition of the copper, indicates that there is no evidence that nitrogen doping was successful or not. This is caused by the similar ionic radiuses of both oxygen and nitrogen. It is clear from the XRD data that nitrogen doping did not change the crystal structure of the perovskite. In addition, all samples are compatible with JCPDS: 00-039-1471 pattern, which can be observed from the Figure 2.4 below.

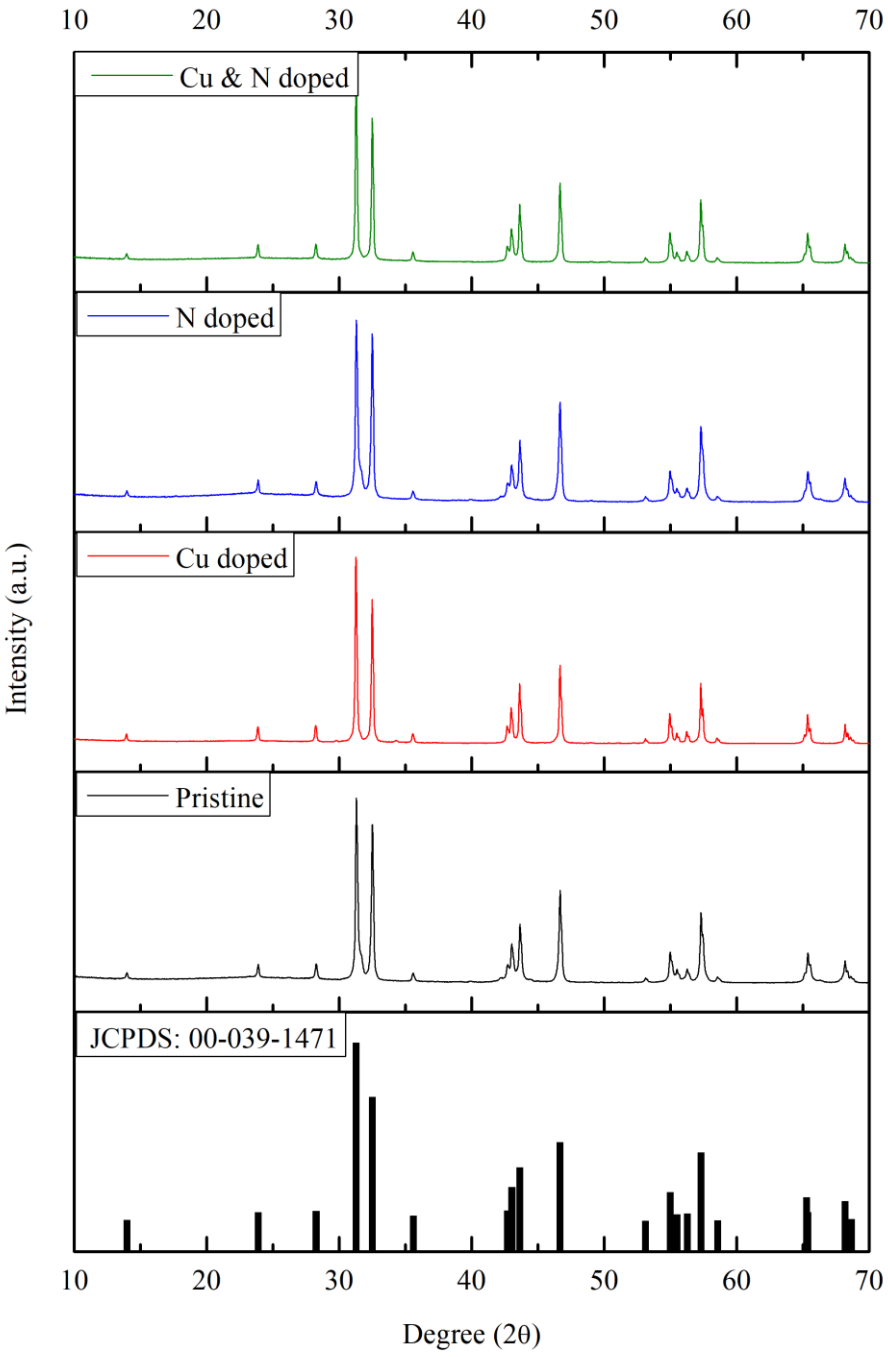

Figure 2.4. XRD patterns of all samples between 10-70 2θ.

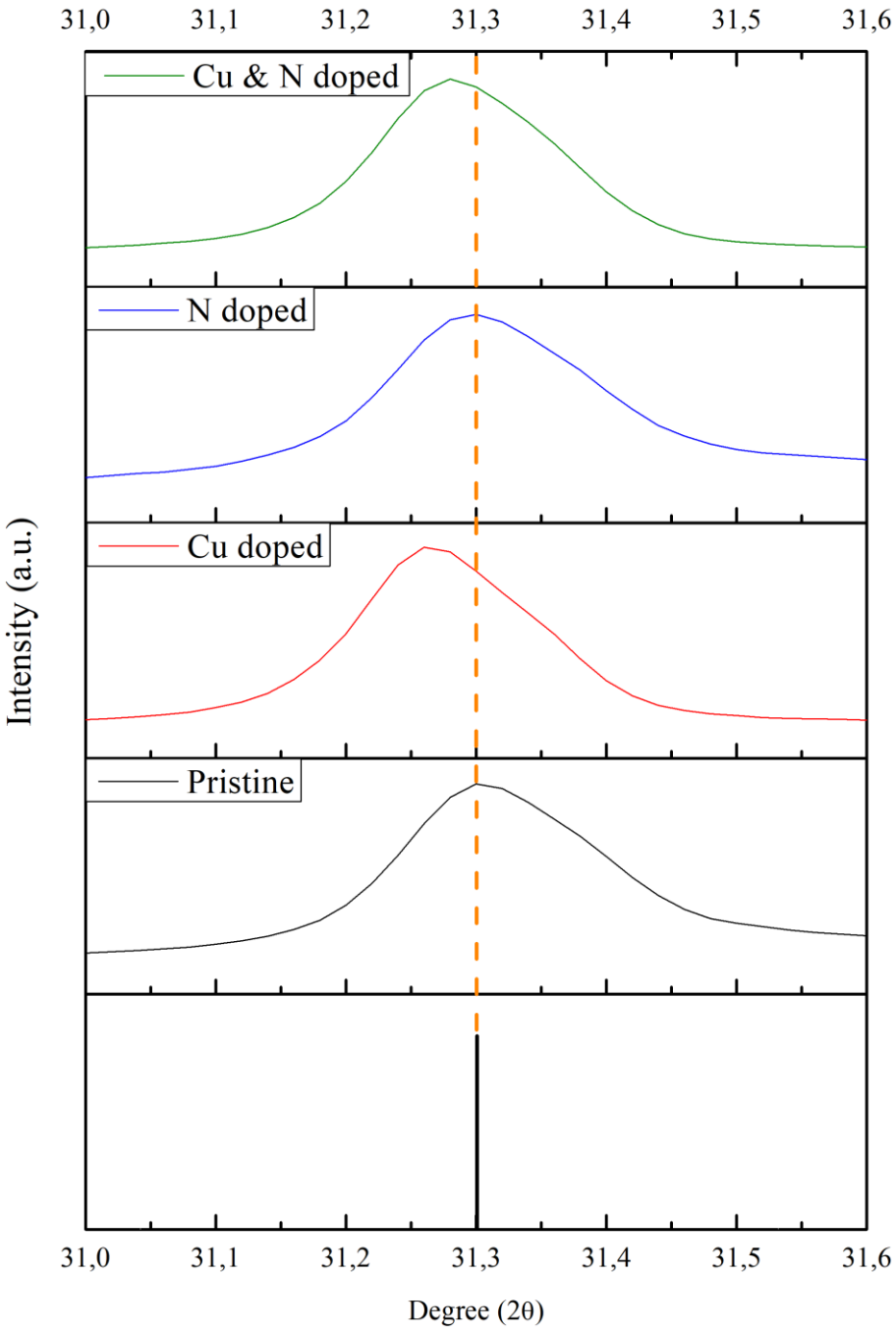

Figure 2.5. XRD patterns of all samples between 31.0-31.6 2θ.

2.3.2 X-ray Photoelectron Spectroscopy (XPS)

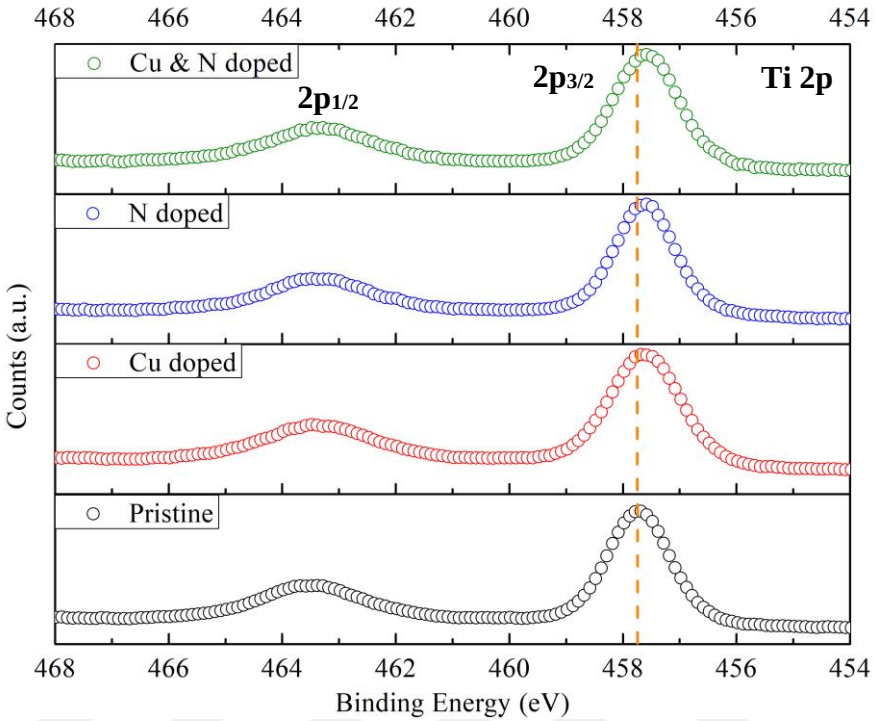

Figure 2.6. XPS spectra of Ti 2p orbital of specimens.

The XPS spectra, which are shown in Figure 2.6, exhibit a shift of both $2p_{1/2}$ and $2p_{3/2}$ peaks to lower binding energy levels. This phenomenon can be seen detailed in the table below. Pristine material has the highest binding energies, whereas the Cu & N doped sample has the lowest. Both only Cu coped and only N doped samples' peak energies are approximately 0.10 eV lower than the pristine one. The binding energy difference between Cu & N doped and the pristine samples is 0.13 eV for $2p_{3/2}$, whereas it is 0.14 eV. Xu et al. state that the Ti^{3+} energy level is lower than the energy level of the Ti^{4+} [123]. They also state that the shift to Ti^{3+} energy level indicates the oxygen vacancy formation. Chen et al. claim that co-doping causes an increase in the number of oxygen vacancies [125]. Thus, the addition of dopants positively correlates with the number of oxygen vacancies.

	$2p_{3/2}$ (eV)	**$2p_{1/2}$ (eV)**
Pristine	457.7	463.4
Cu	457.61	463.3
N	457.6	463.29
Cu & N	457.57	463.26

Table 2.1. Ti 2p orbital peak positions

XPS spectra of Cu 2p were inspected for Cu doped, and Cu & N doped samples were inspected (see Figure 2.7) to determine Cu presence, the charge of Cu in the lattice, and the effect of nitrogen doping on maximum peak values. The peaks at 932.39 eV for $2p_{3/2}$ and 952.22 eV for $2p_{1/2}$ show copper present in both samples. Even though copper acetate was used to synthesize this material, the charge of Cu inside the matrix was determined as +1. Satellites are essential for charge determination. The weak satellites prove Cu's charge, as found in a previous study [126]. The peak positions were the same for both specimens, which indicates that the addition of nitrogen did not cause any peak shift. Thus, the nitrogen atoms most likely did not bond with the Cu.

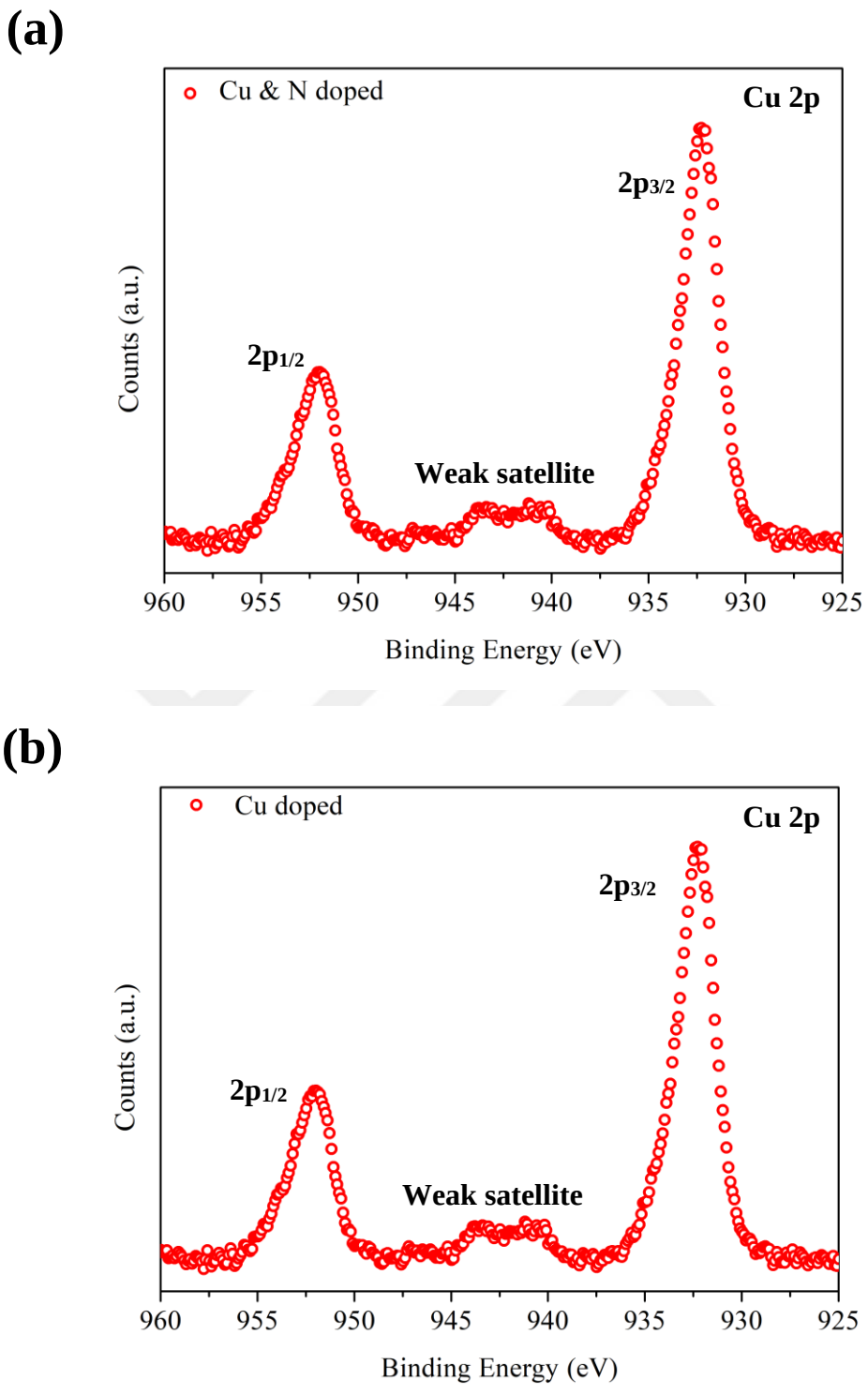

Figure 2.7. XPS spectra of Cu 2p of: (a) Cu doped and (b) Cu & N doped samples.

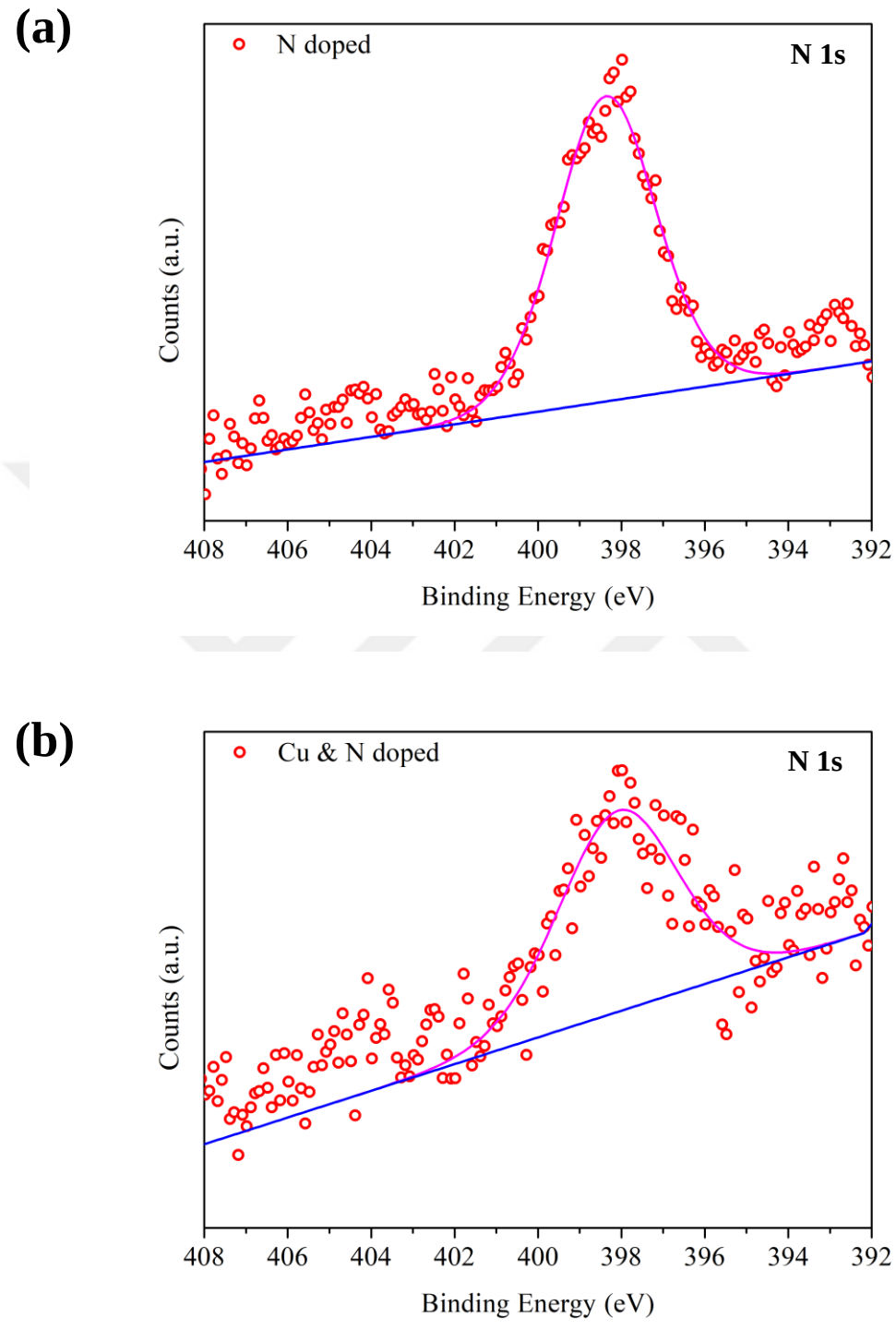

Figure 2.8. XPS spectra of of N 1s of: (a) N doped and (b) Cu & N doped samples.

According to the fig, the N 1s peaks were found at 398.37 eV for N doped sample, whereas it was found at 398.08 eV for Cu & N doped sample. These results show that the N is present in the structure. The peak position aligns with the literature, as well [123].

(a)

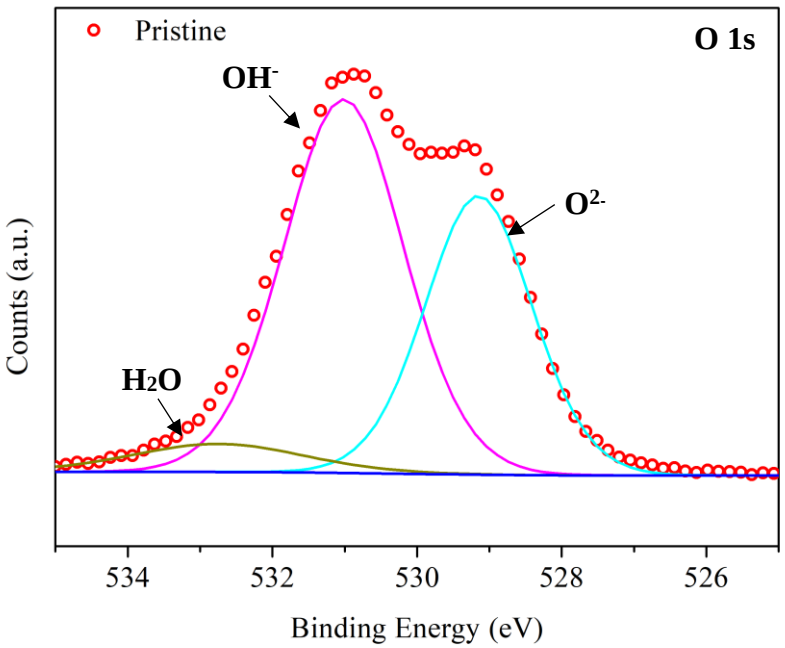
Pristine
O 1s
OH-
O2-
H2O
Counts (a.u.)
534
532
530
528
526
Binding Energy (eV)

(b)

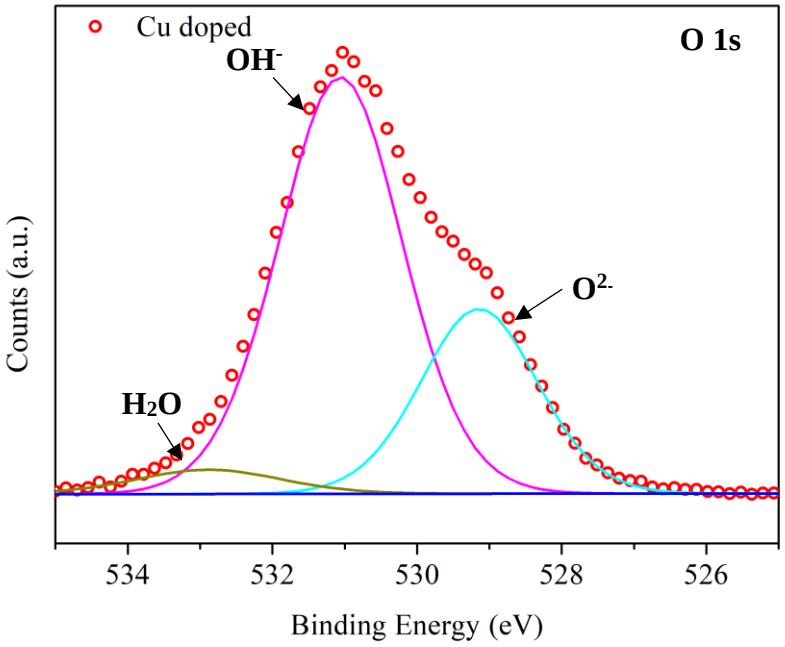
Cu doped
O 1s
OH-
O2-
H2O
Counts (a.u.)
534
532
530
528
526
Binding Energy (eV)

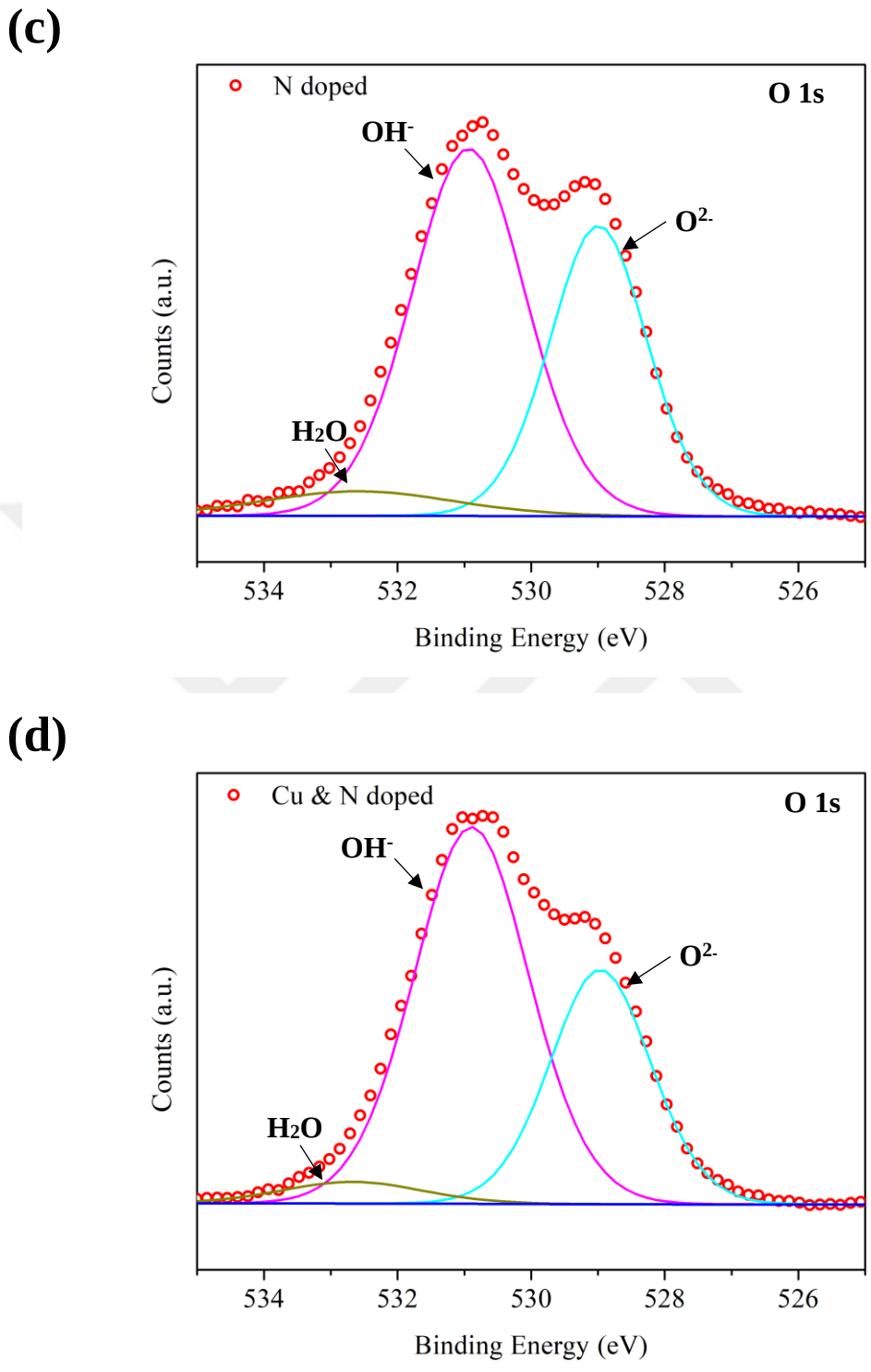

Figure 2.9. XPS spectra of O 1s orbital of specimens: (a) Pristine, (b) Cu doped, (c) N doped, and (d) Cu & N doped.

O 1s orbital may have different peaks due to the O-containing functional groups, which can be seen from the Figure 2.9. In this case, lattice oxygen was shown with O^{2-}, adsorbed O_2 and hydroxyl groups were shown with OH^-, and finally H_2O peak was indicated [123,127]. The Table 2.2 below, which exhibits the peak maxima binding energies and area ratios for peaks, was prepared to evaluate the data correctly. The OH^-/O^{2-} ratios for the samples indicate that copper doping causes lattice oxygen groups (O^{2-}) area to decrease, which is expected due to the charge of copper in the lattice is +1. Thus, it can be stated that copper doping causes the formation of oxygen vacancies.

	Pristine		**Cu doped**		**N doped**		**Cu & N doped**	
	Peak Maxima (eV)	Peak Area ratios	Peak Maxima (eV)	Peak Area ratios	Peak Maxima (eV)	Peak Area ratios	Peak Maxima (eV)	Peak Area ratios
O^{2-}	529.15	0.75	529.14	0.44	528.99	0.79	528.96	0.62
OH^-	531.01	1.00	531.06	1.00	530.94	1.00	530.89	1.00
H_2O	532.75	0.08	532.88	0.06	532.59	0.07	532.88	0.06

Table 2.2. Peak maxima and number of counts of O 1s species

2.3.3 Morphological Analysis

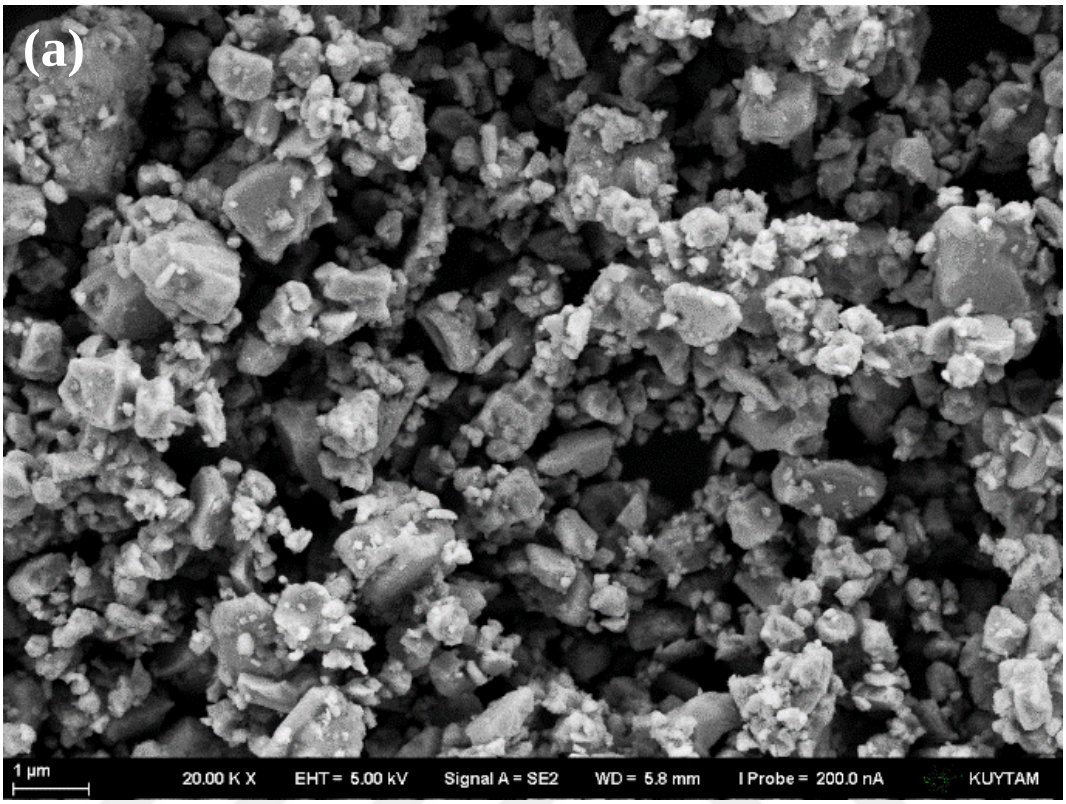

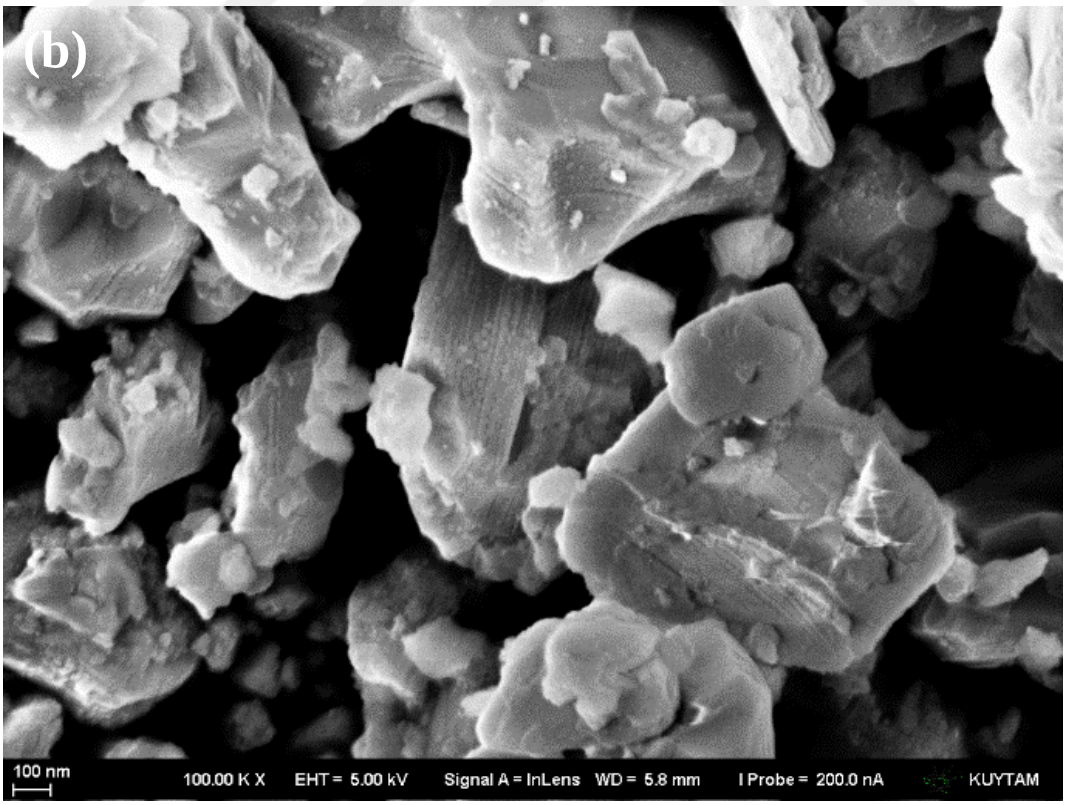

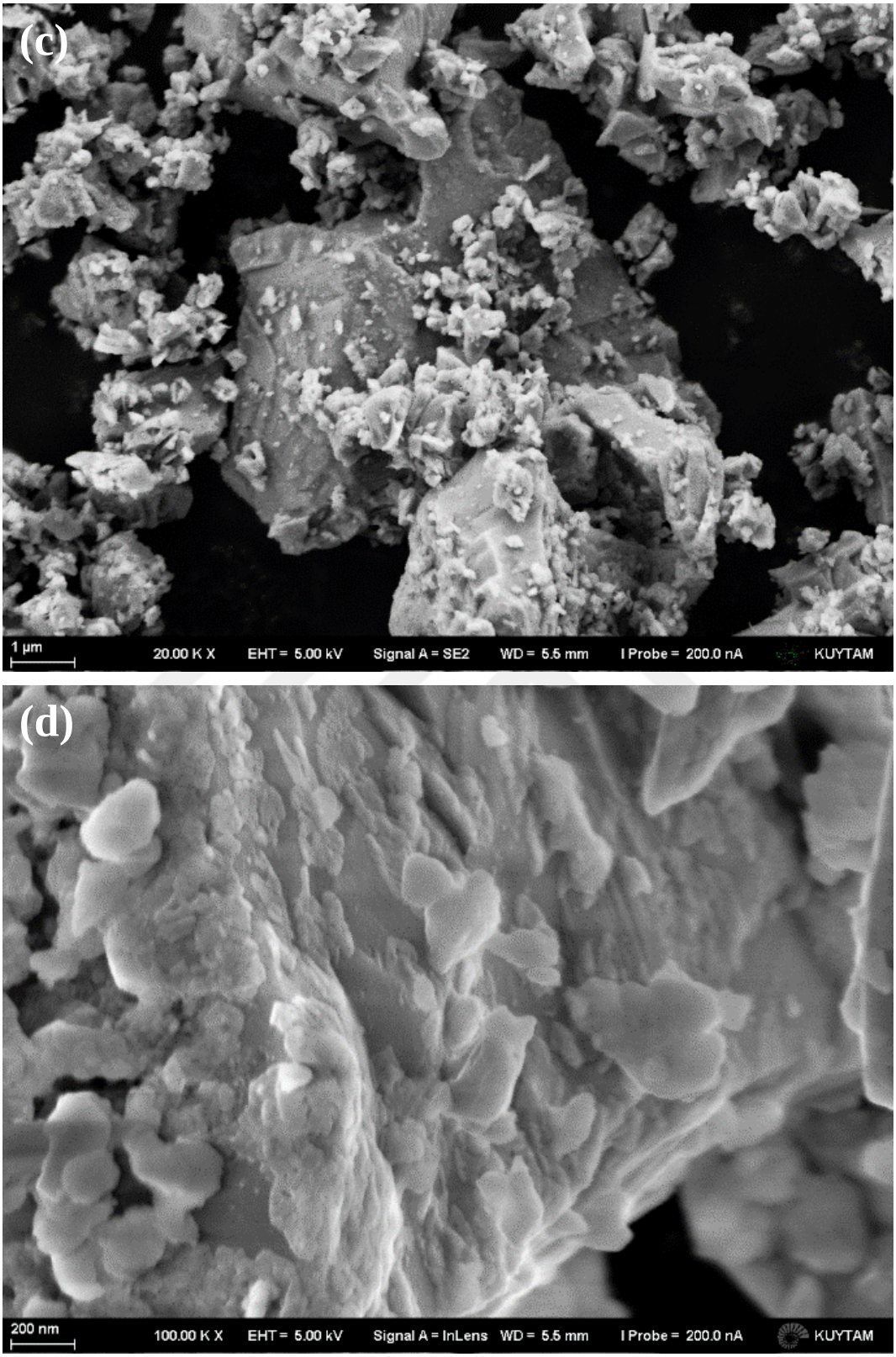

Figure 2.10. FESEM Images of (a) Sr_2TiO_4 larger scale, (b) Sr_2TiO_4 zoomed in, (c) $Sr_2Cu_{0.05}Ti_{0.95}O_4$ larger scale, (d) $Sr_2Cu_{0.05}Ti_{0.95}O_4$ zoomed in.

FESEM images of the samples before the nitrogen doping show that the copper's introduction to the system does not significantly impact the structure morphology. Figure 2.10a shows the Sr_2TiO_4 larger scale, indicating that the particle size distribution is mostly even. However, the Figure 2.10c exhibits the image of larger bulky particles, which may influence the hydrogen evolution rates due to smaller particle size causing higher surface area, which positively correlates with the efficiency of a catalyst. This might happen because the sample was calcined in pellet form, and this pellet was ground afterward. Since this process is mechanical, it is possible to have larger particles. However, the Figure 2.10b and Figure 2.10d give a clear view of the layered structure. They also show that the particle structure is similar. Thus, the material obtained has the same morphology.

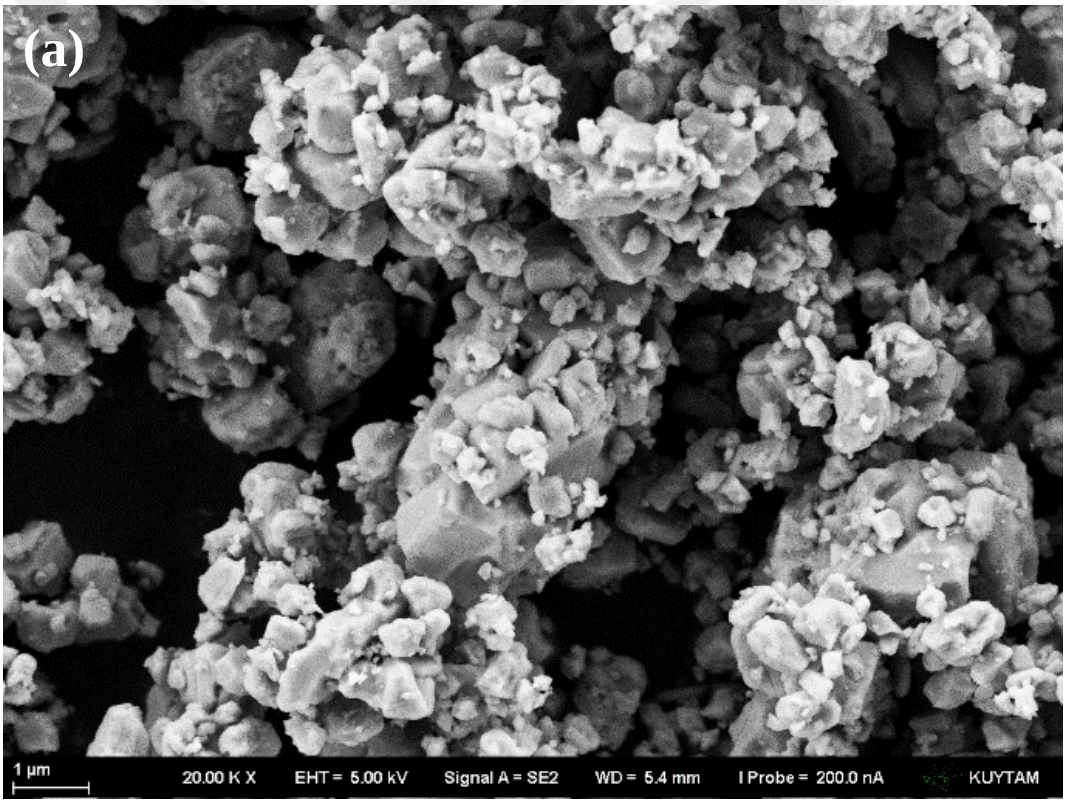

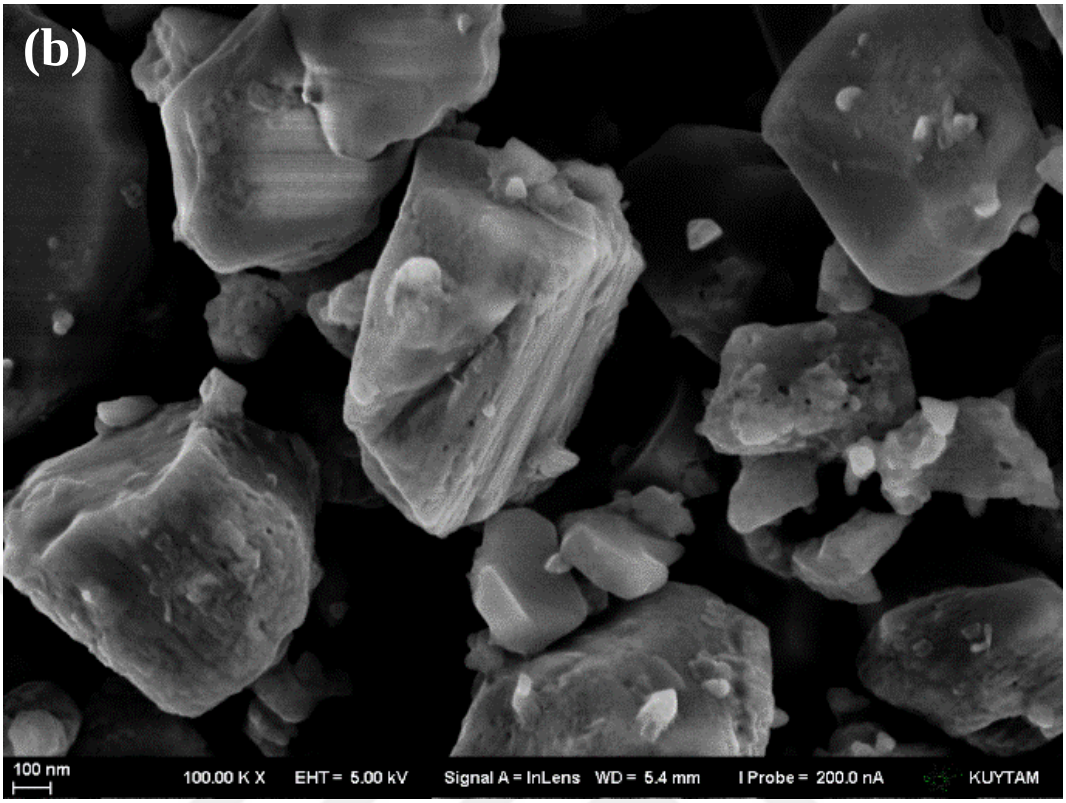
(b)
100 nm
100.00 K X
EHT = 5.00 kV
Signal A = InLens
WD = 5.4 mm
I Probe = 200.0 nA
KUYTAM

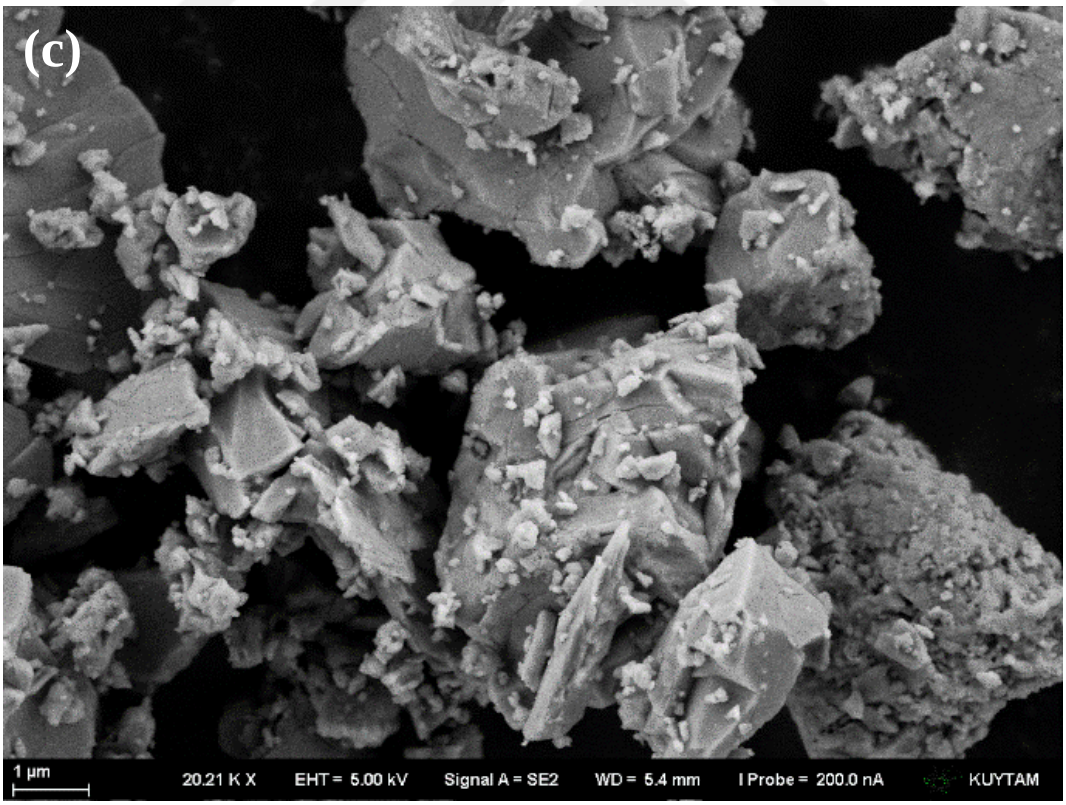
(c)
1 µm
20.21 K X
EHT = 5.00 kV
Signal A = SE2
WD = 5.4 mm
I Probe = 200.0 nA
KUYTAM

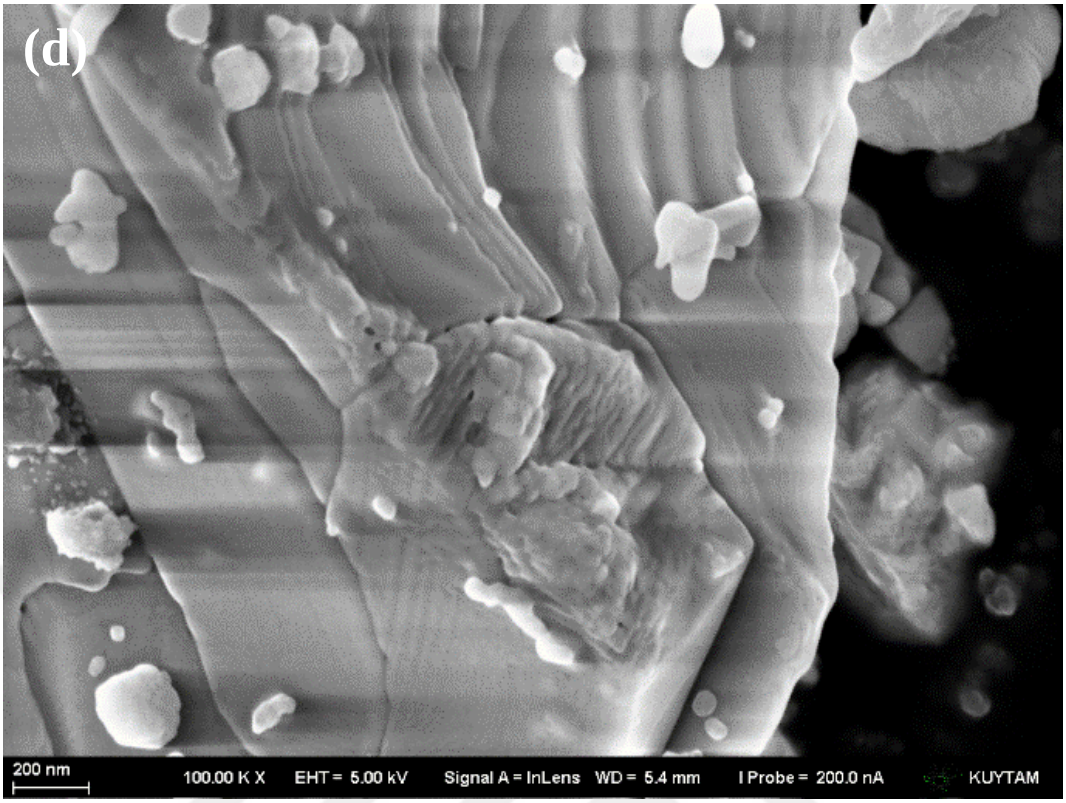

Figure 2.11. FESEM Images of (a) $Sr_2Ti\ O_{4-x}N_x$ larger scale, (b) $Sr_2Ti\ O_{4-x}N_x$ zoomed in, (c) $Sr_2Cu_{0.05}Ti_{0.95}O_{4-x}N_x$ larger scale, (d) $Sr_2Cu_{0.05}Ti_{0.95}O_{4-x}N_x$ zoomed in.

The images of the nitrogen-doped sample Figure 2.11a and Figure 2.11c show the macro-scale view of the powders, and the images indicate different particle size distribution, which may be caused by the mechanical grinding process, which was stated earlier. Also, it should be noted that the ammonolysis was performed on the pristine (Sr_2TiO_4**)** and copper doped ($Sr_2Cu_{0.05}Ti_{0.95}O_4$) samples. Thus, it is expected that they have the same morphology. The Figure 2.11b and Figure 2.11d, which show only nitrogen-doped and co-doped samples, respectively, reveal that the layered structure was preserved after the ammonolysis. Therefore, it can be stated that the structural integrity of the samples remained the same after the nitrogen introduction. All the samples have the same morphological properties.

2.3.4 Optical Properties

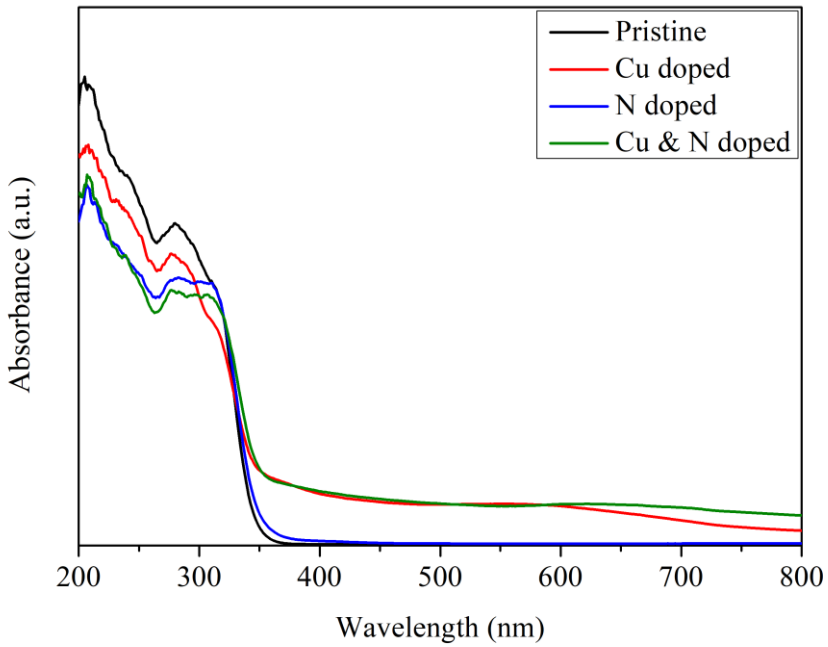

Figure 2.12. UV-VIS Spectra of the samples.

The absorbance spectra of the samples were obtained by Kubelka-Munk transformation of diffuse reflectance spectra, and it can be seen from the Figure 2.12. The absorbance spectrum indicates that the introduction of copper to the system increases light absorbance for wavelengths above 350 nm. It can be observed that the absorbance was increased for the whole possible spectrum, yet after the 600 nm, the absorbance rate of the copper doped sample was slightly decreased. Even though there is a declination of absorbance, the copper doped sample still has more absorbance capability than the samples that do not contain copper dopant. When the effect of nitrogen doping is increased, it can be stated that nitrogen doping has a positive effect on absorbance for both pristine and copper-doped samples. The absorbance edge was slightly shifted to a higher wavelength, where it was slightly shifted to a lower wavelength for the copper doped sample. Nevertheless, the impact of nitrogen doping, which increases absorbance for the copper doped sample, can be observed for the wavelengths higher than 600 nm. While the absorbance decreases for the copper doped sample, adding nitrogen to the chemical structure allowed the sample to absorb at higher wavelengths. This occurrence

might be related to increased nitrogen uptake due to doping [11]. Sun et al. claim that the amount of nitrogen doping is relevant to the dopant concentration in the structure. This may be why there is no visible increase in absorbance percentage for the pristine sample after the nitrogen doping.

(a)

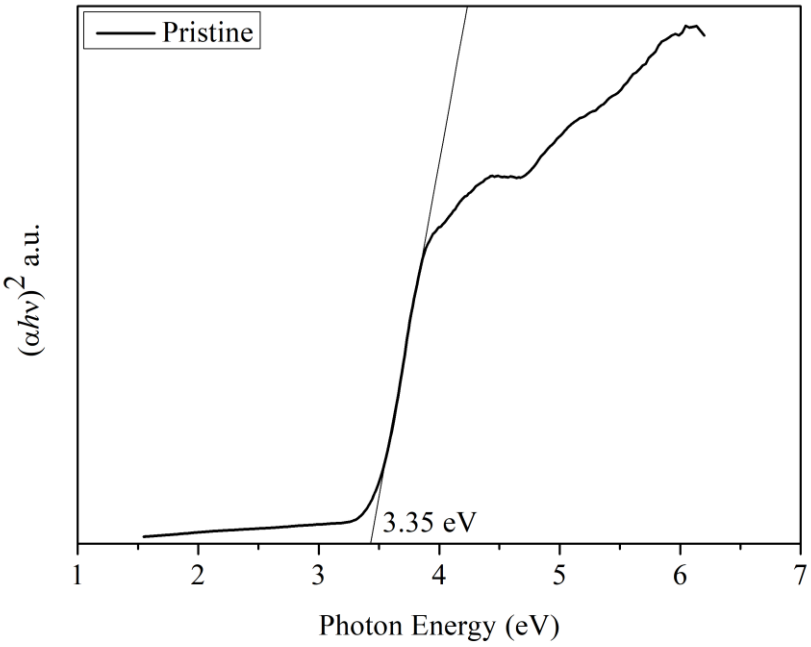

(b)

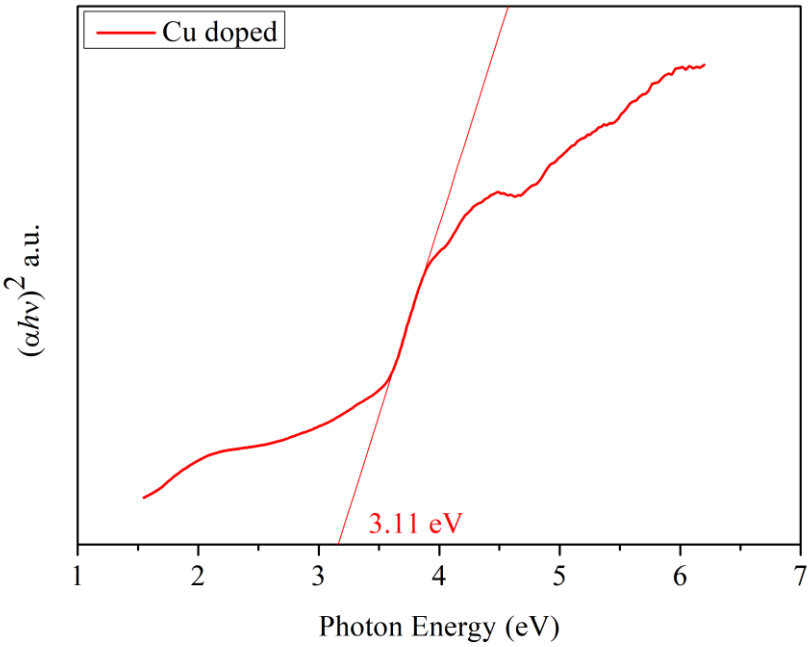

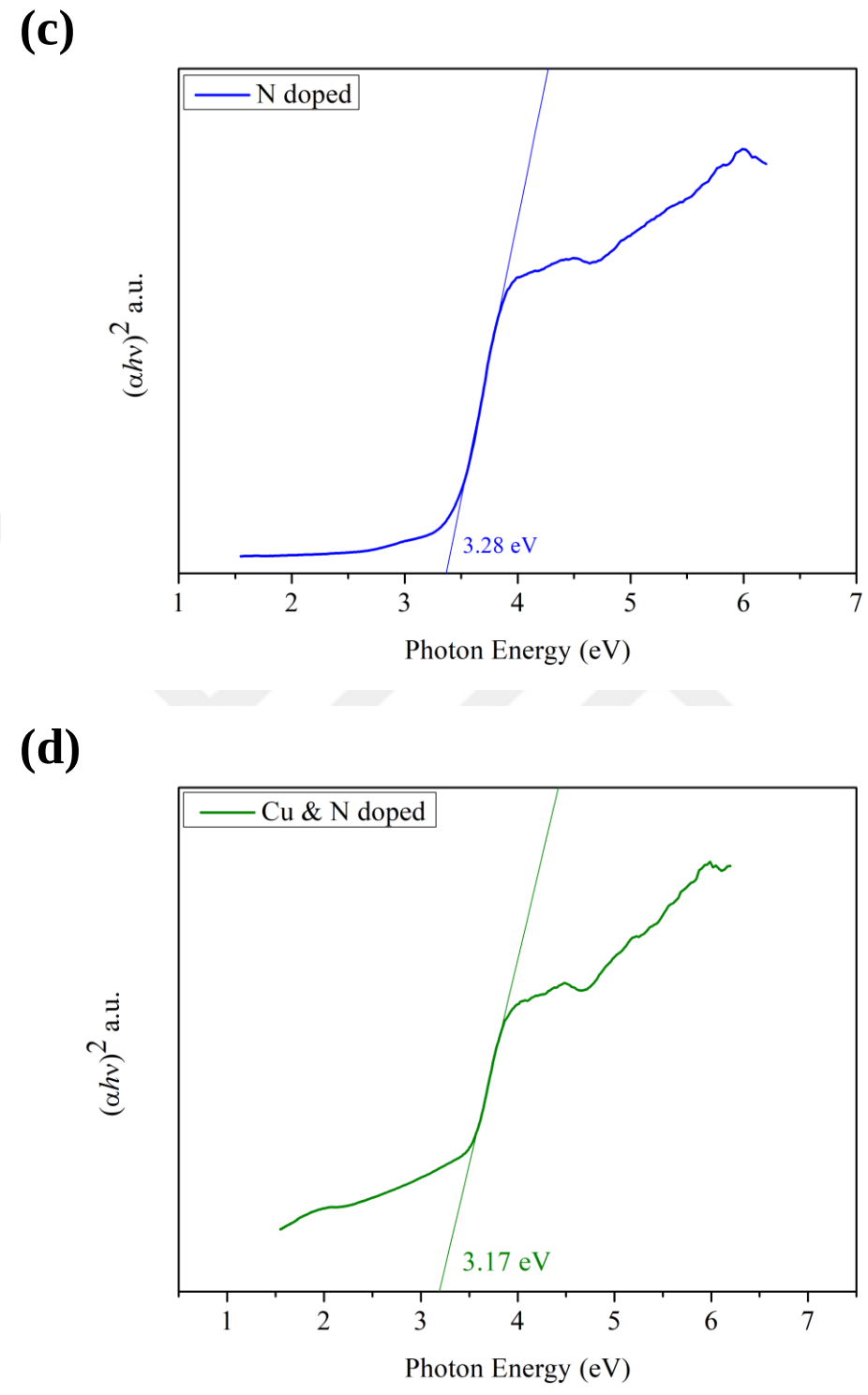

Figure 2.13. TAUC plots of samples: (a) Pristine, (b) Cu doped, (c) N doped, and (d) Cu & N doped. (a) Pristine, (b) Cu doped, (c) N doped, and (d) Cu & N doped.

Sample Content	Band gap (eV)
Pristine	3.43
Copper doped	3.16
Nitrogen doped	3.37
Co-doped	3.19

Table 2.3. Estimated band gap values for samples

TAUC plot is used to calculate the optical bandgap of semiconductor materials. The equation, which can be seen below, consists of α as the adsorption coefficient, *h* as the Planck constant, ν stands for frequency, γ indicates transmission type (direct or indirect), A is energy dependent constant, and E_g stands for bandgap. The interception to 0 on x-axis is used for determination of the bandgap value, in which the equation is plotted $(\alpha h\nu)^{\gamma}$ against the photon energy (eV).

$$(\alpha h\nu)^{\gamma} = A(h\nu - E_g) \tag{15}$$

Figure 2.13 shows the TAUC plots of the samples, which were calculated for direct allowed transitions due to Kwak et al. also calculated the band gap by using ½ as the γ value [12]. Their calculation for pristine Sr_2TiO_4 is 3.33 eV, whereas our results show it is 3.35 eV. These values are remarkably close to each other, and therefore using direct allowed transitions (r = 1/2) for the calculations is correct. Because of this reason, the other calculations made for the doped samples are also confirmed. The Table 2.3 shows the calculated band gap values for the samples. The doping of only copper or nitrogen decreases the band gap in both cases. However, copper doing has more impact on the band gap due to the band gap of the sample decreasing from 3.35 eV (Pristine) to 3.11 eV (Copper doped). On the other hand, the co-doped sample has a band gap of 3.17 eV, whereas the copper doped sample has a band gap of 3.11 eV. This indicates that the bandgap value was increased when the nitrogen was introduced to the chemical structure while copper was also present in the structure. Xin-Guo et al. give the reason for this occurrence as band gap width increases because of shorter N—Cu bonds and higher energy N 2p levels, which causes an upward shift of the conduction band bottom [128].

2.3.5 Photoelectrochemical Analysis (PEC)

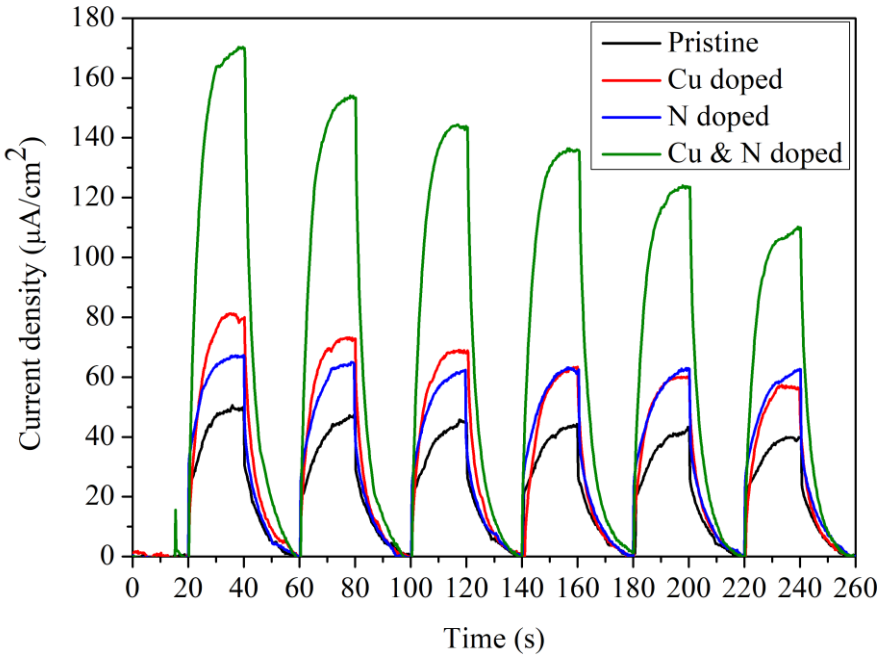

Figure 2.14. Chronoamperometric measurements of samples

	Maximum Amplitude (μA/cm^2)			
# of peak	**Pristine**	**Cu**	**N**	**Cu & N**
1	49.4	81.4	66.0	168.1
2	45.9	72.7	64.0	153.1
3	43.5	68.3	61.8	144.0
4	43.5	63.6	62.6	136.2
5	40.7	62.8	62.5	123.5
6	40.0	57.7	60.9	107.4

Table 2.4. Current density magnitudes of samples

The current density vs. time plots, which can be seen from the Figure 2.14, of the materials exhibit the amplitude magnitude order of co-doped, Cu doped, N doped, and pristine from highest to the lowest. Specifically, the increase in the co-doped material's

current density is significantly higher compared to the others. The current density amplitudes for all the samples can be seen from the Table 2.4. The remarkable part is that the copper-free samples' current density values change at a lower rate (for N doped material, it starts from 66.0 $\mu A/cm^2$ and ends at 60.9 $\mu A/cm^2$). In contrast, the current densities of the copper-doped samples decrease significantly in time for each peak (for the co-doped sample, it starts from 168.1 $\mu A/cm^2$ and ends at 107.4 $\mu A/cm^2$. It should also be considered that the initial current density value of each sample was set to 0, and they were all background subtracted due to their constantly decreasing baseline current density values of theirs. The formation of charge carriers (electron and holes) and the recovery time of the system takes a while due to the current density decreasing in time rather than going to the baseline right after 20 seconds of illumination time ends (see Figure 2.14). As a result, the non-recombined electrons are trapped on the surface of the electrode. Because of this reason, the baseline current and peak intensity values are decreasing in this case. In addition, the Table 2.3 shows that the photocurrent density is not only associated with the band gap value [129].

(a)

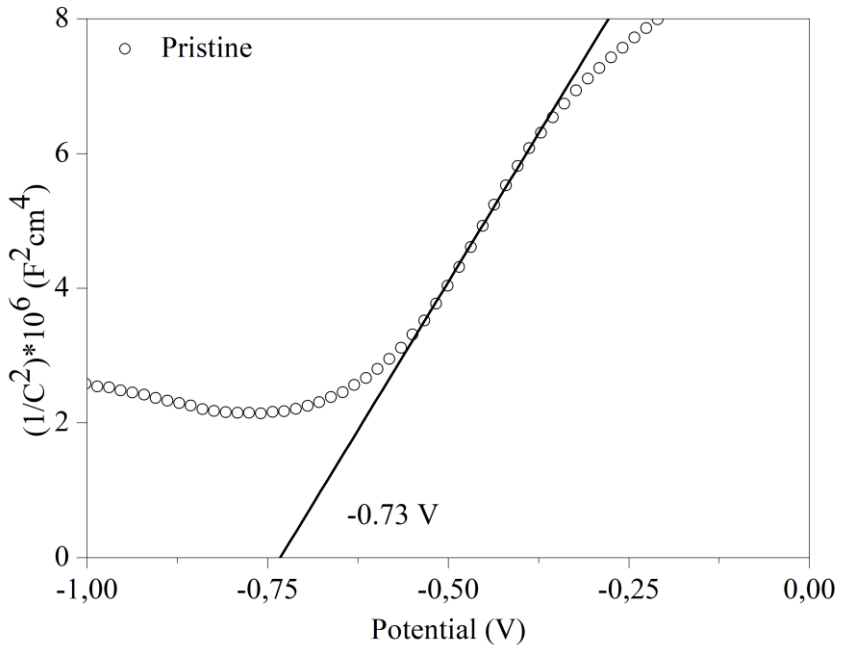
Pristine
-0.73 V
$(1/C^2)*10^6\ (F^2cm^4)$
Potential (V)
8
6
4
2
0
-1,00
-0,75
-0,50
-0,25
0,00

(b)

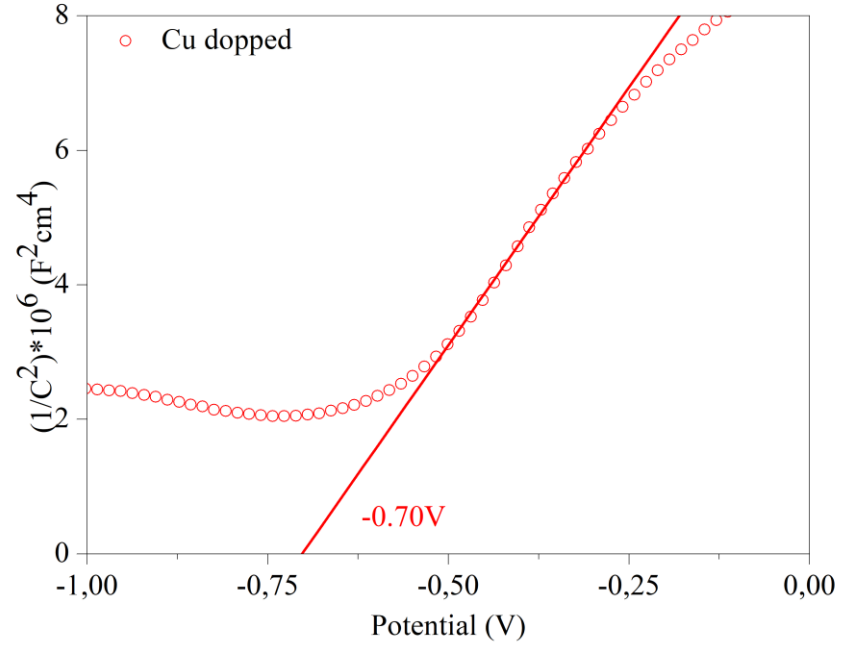
Cu dopped
-0.70V
$(1/C^2)*10^6\ (F^2cm^4)$
Potential (V)
8
6
4
2
0
-1,00
-0,75
-0,50
-0,25
0,00

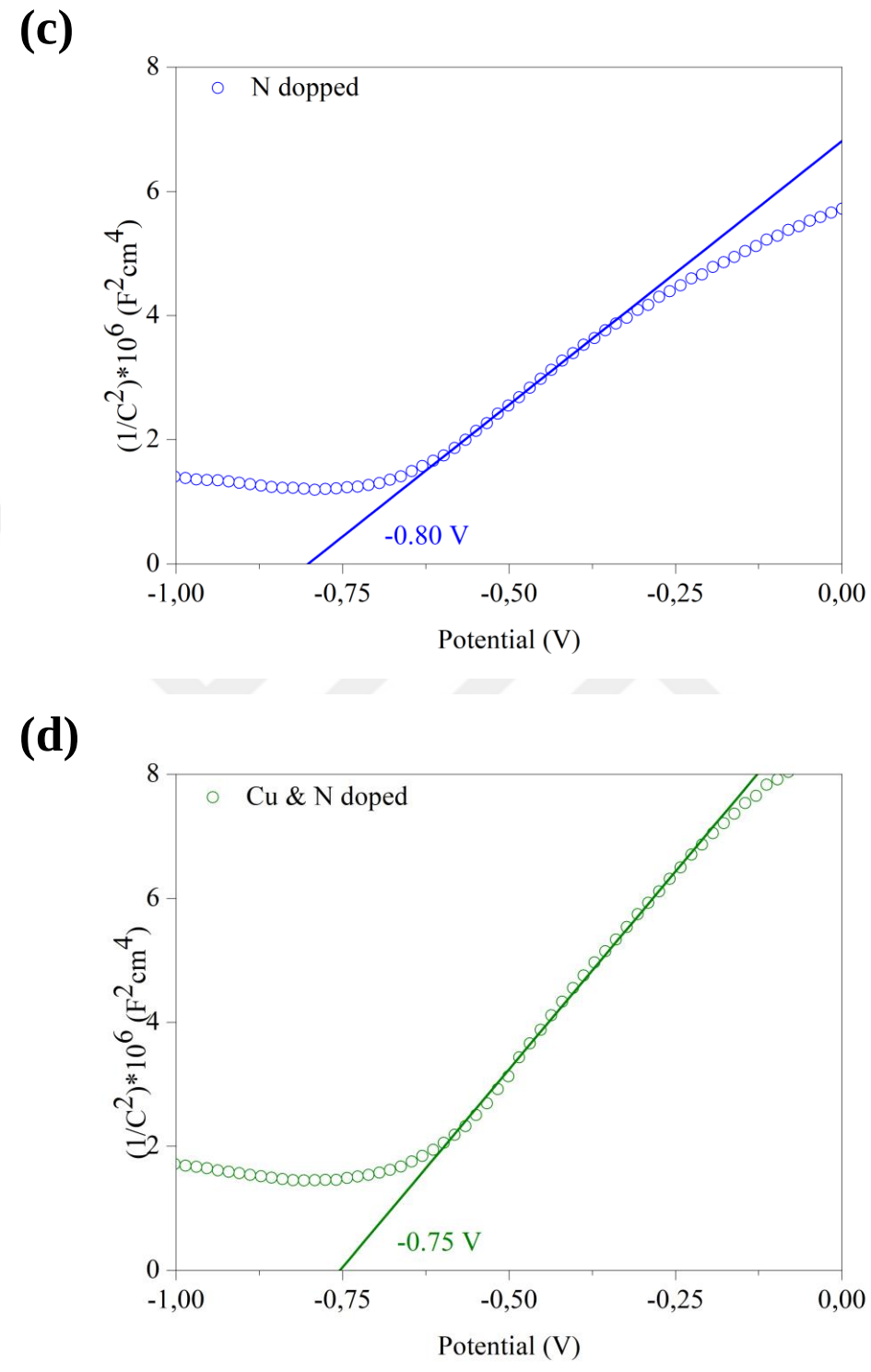

Figure 2.15. Mott-Schottky plots of samples: (a) Pristine, (b) Cu doped, (c) N doped, and (d) Cu & N doped. (a) Pristine, (b) Cu doped, (c) N doped, and (d) Cu & N doped

The Mott-Schottky analysis was also performed using thin films without illumination for the specimens. The results show the flat band potentials for each sample, which can be observed from the Figure 2.15. The positive slopes of the Mott-Schottky plots indicate that these materials are n-type semiconductors [130]. In addition, the type of semiconductor can also be learned from the chronoamperometric results, which are shown in the Figure 2.14. The anodic current indicates the materials type of semiconductor, as well. It should also be considered that the thickness of the thin films also plays a crucial role in the Mott-Schottky analysis. There are publications regarding the effect of the film thickness on the flat band potential [131,132]. Xiao et al. did a Mott-Schottky measurement for Sr_2TiO_4 and calculated its flat band potential as -0.47 V versus Ag/AgCl electrode [133]. Our experiments were done using SCE as the reference electrode. The difference between Ag/AgCl and SCE is around 0.04 V. In addition, Xİeao et al. used the spin coating technique for electrode production. The different results may be related to film thickness, as was stated.

2.3.6 Photocatalytic Hydrogen Production

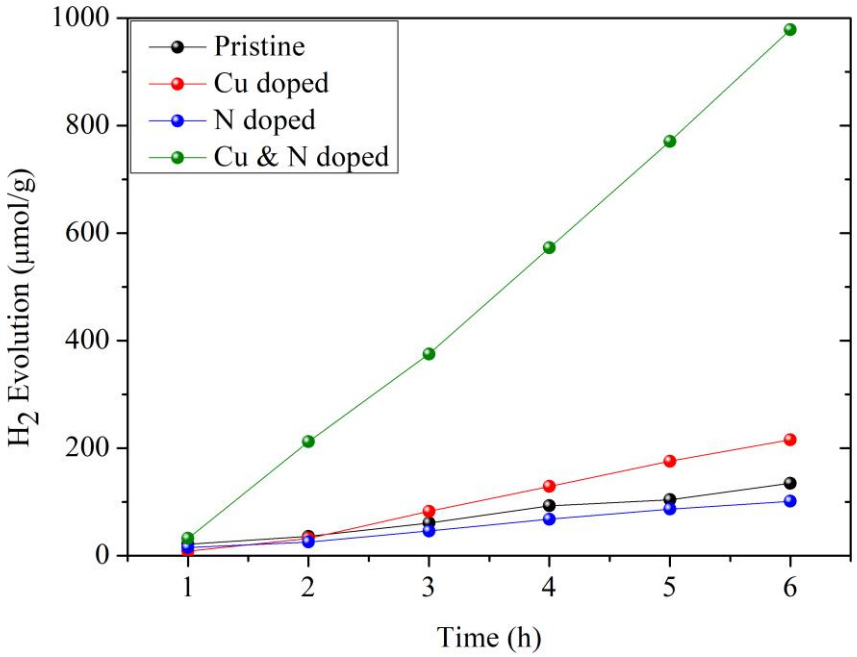

Figure 2.16. H_2 evolution under UV irradiation without co-catalyst

	H_2 amounts for samples (μmol/g)			
Time (h)	**Pristine**	**Cu**	**N**	**Cu & N**
1	21.71	8.50	15.36	32.31
2	35.92	32.31	25.55	212.11
3	60.83	82.49	46.02	375.17
4	92.87	128.93	67.91	572.47
5	104.20	175.82	86.65	770.50
6	134.73	215.67	101.51	978.50

Table 2.5. H_2 production of samples against time under UV illumination

Figure 2.16 exhibits the hydrogen production versus time of specimens under UV irradiation. The Table 2.5 shows the amount of hydrogen produced for the corresponding hour. After the 6 hours of illumination, the highest hydrogen production amount was achieved using the co-doped sample, which yields 978.50 μmol/g of hydrogen, followed by the copper doped sample with a yield of 215.67 μmol/g of hydrogen. There is an approximately 5-fold increase in hydrogen production after 6 hours of reaction time. This significant increase indicates that co-doping has a large impact on photocatalytic hydrogen production with Sr_2TiO_4. On the other hand, the introduction of nitrogen to the pristine sample yielded less hydrogen (134.73 μmol/g for pristine and 101.51 μmol/g for only nitrogen-doped). As was previously stated, the amount of nitrogen doping in the system is related to the chemical composition of the material. A certain amount of nitrogen doping to the system increases the rate of hole hopping; if this nitrogen limit for each specimen is exceeded, the defects formed in the structure increase the recombination rate [134]. Because of this reason, the excessive doping with nitrogen may be the reason for nitrogen-doped pristine sample's ($Sr_2TiO_{4-x}N_x$) low efficiency.

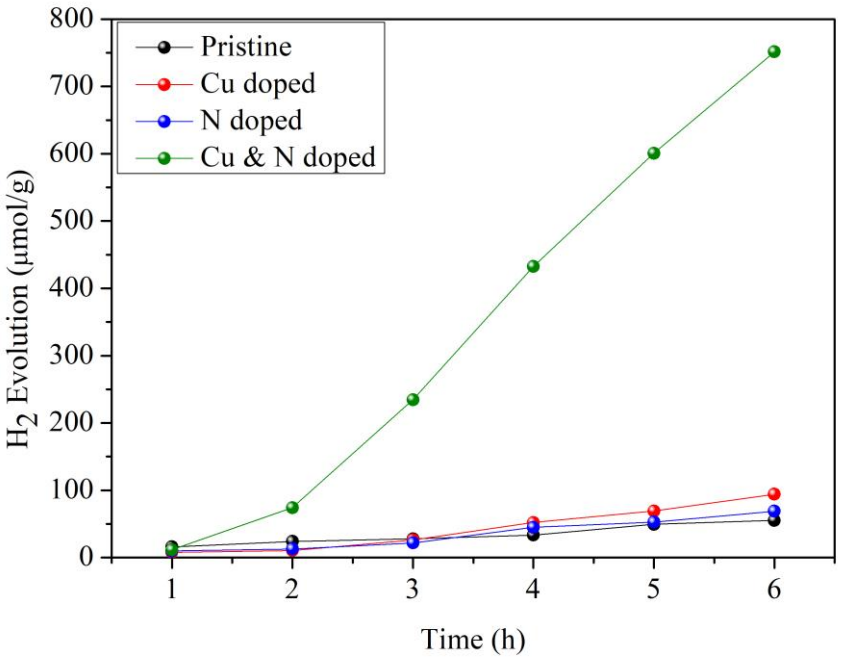

Figure 2.17. H_2 evolution under AM 1.5 filtered illumination without co-catalyst

	H_2 amounts for samples (µmol/g)			
Time (h)	**Pristine**	**Cu**	**N**	**Cu & N**
1	15.98	7.95	9.82	11.70
2	23.93	10.63	12.77	74.20
3	27.86	26.38	21.70	234.51
4	33.48	52.19	45.00	432.41
5	49.46	69.15	52.77	600.71
6	55.31	94.11	68.97	751.52

Table 2.6. H_2 production of samples against time under perfect light (AM 1.5) illumination

The hydrogen production amounts were also recorded using the AM 1.5 filtered light as a source of simulated sunlight. Since the sunlight is readily available in nature, our study aims to have a material that will work in this given range of the spectrum. The

Figure 2.17 shows the hydrogen amount for corresponding hours; the exact results can be seen in the Table 2.6. The results showed that the most hydrogen production was obtained from the co-doped sample with a yield of 751.52 μmol/g after 6 hours. This result indicates that the hydrogen production amount, which shows the lowest change, decreased by 23.2 % for the co-doped sample compared to result obtained from non-filtered UV light. For the others, the decreasing percentages were 58.9 % for pristine, 56.4 % for copper doped, and 32.1 % for the nitrogen-doped sample. As was expected, the introduction of nitrogen to the system allowed the absorption at higher wavelengths. Thus, the nitrogen-doped samples' change percentages are lower than the other samples. According to the first measurement, which took place under UV illumination (see Table 2.5), the pristine sample outperformed the nitrogen-doped sample, yet for the sunlight measurement, this was reversed. On the other hand, the pristine and only nitrogen doped samples yield 55.31 μmol/g and 69.97 μmol/g of hydrogen accordingly after 6 hours of illumination. These amounts indicate that hydrogen production was increased when sunlight illumination was introduced.

2.4 Conclusions

In this chapter, pristine (Sr_2TiO_4) and ($Sr_2Ti_{0.95}Cu_{0.05}O_4$) were tried to be synthesized, then doped with nitrogen to see the effect of single and co-doping on the bandgap and the hydrogen production by obtaining $Sr_2TiO_{4-x}N_x$ and $Sr_2Cu_{0.05}Ti_{0.95}O_{4-x}N_x$.

The XRD results indicate the peak shift to the lower angles, which can be associated with copper doping. The XPS results confirmed the presence of nitrogen and copper in the corresponding samples. The most important discovery from this part was the assessment of the charge of the copper introduced, which was determined as +1. These materials were successfully synthesized and doped according to the overall results obtained. The SEM results showed that the materials have the same layered morphology, indicating structural integrity.

The UV-VIS spectrum results demonstrated that the addition of copper to the lattice increases the absorbance in the visible range. In addition, using dopants altered the bandgap of the pristine material from 3.43 eV to 3.16 eV, 3.37 eV, and 3.19 eV for only copper doped, only nitrogen doped, and co-doped correspondingly. The photoelectrochemical measurements showed that the highest photocurrent values were

obtained from the copper and nitrogen doped sample, which correlates with photocatalytic hydrogen production. Also, the flat band values against SCE were found as -0.73 V for pristine, -0.70 V for only copper doped, -0.80 V for only nitrogen doped, and -0.75 V for co-doped with Mott-Schottky analysis.

Finally, the photocatalytic hydrogen production experiments resulted in 22.45, 35.95, 16.92, and 163.08 $g\mu mol^{-1}h^{-1}$ for pristine, only copper doped, only nitrogen doped, and co-doped correspondingly under UV illumination. These experiments were also performed using simulated sunlight equipping AM-1.5 filter. The results showed that the rates of 9.22, 15.69, 11.50, and 125.25 $g\mu mol^{-1}h^{-1}$ for pristine, only copper doped, only nitrogen doped, and co-doped correspondingly were obtained for the photocatalytic hydrogen production.

All in all, hydrogen production efficiency was increased significantly by introducing two dopants simultaneously. It should also be noted that no co-catalyst was used to improve the rates further. The aim, which was having cost-efficient materials works under solar light, was achieved in this work.

Chapter 3: **Photocatalytic Hydrogen Evolution from Noble Metal Doped Layered Potassium Niobate**

3.1 Introduction

Conventional perovskite oxides are used as semiconductor materials for photocatalytic purposes [76,88,135–138]. The three different layered phases of perovskite oxides are Aurivillius, Ruddlesden-Popper, and Dion-Jacobson. The Dion-Jacobson phase has the structural formula of $A'A_{n-1}B_nO_{3n+1}$ [139], which is used for photocatalytic water-splitting applications [100,140,141]. It is possible to encounter Dion-Jacobson niobates with a different number of layers [142], dopants [143], and principal components [104,144] in the literature.

Many examples of photocatalytic hydrogen production processes take place with a co-catalyst [91]. Co-catalyst acts as an active site, and it promotes charge separation when used [143]. If the co-catalyst is not introduced to the system, most of the time, the hydrogen production rate will be relatively lower than its counterpart with a co-catalyst [145]. Since the addition of the co-catalyst is performed after the synthesis of the semiconductor material, the effect of the co-catalyst will be limited, and it will not cause to change in the electronic properties of the material. Because of this reason, the introduction of the dopants to the system allows for manipulation of the electronic structure and thus change of the bandgap [143].

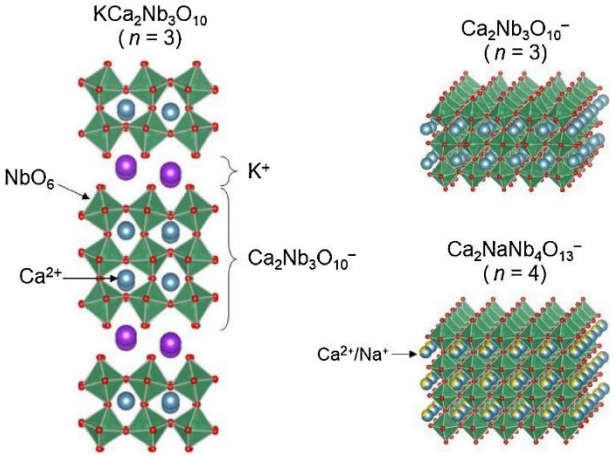

Figure 3.1. Illustrations of $KCaNb_3O_{10}$ (left), $CaNb_3O_{10}^-$ (upper right), and $Ca_2Nb_4O_{13}^-$ (lower right) [146]

In order to obtain an effective photocatalyst, efficient metals promote hydrogen evolution such as Pt can be doped to the system to increase the hydrogen production capability of the pristine material. Metal doped octahedral acts as an active site, and the water-splitting process can occur on them. However, these active sites might be entrapped inside the crystal structure because of their introduction to the system prior to synthesis. The hydrogen exchange process disrupts the bulk layers, and therefore, it may cause an increased likelihood of active sites partaking in the photochemical process. In addition, replacing a cation with a hydrogen atom will change the chemical structure, thus, the optoelectronic properties. Okamoto et al. did research regarding doping the n = 3 calcium niobate with different Rh dopant ratios; their research showed that the Rh was successfully doped to the perovskite oxide structure, and it caused superior hydrogen production activity [143]. By utilizing this information, photochemically active metals: Pd, Pt, Ru, and Rh were used as dopants in an n = 4 calcium niobate system ($KCa_2NaNb_4O_{13}$), and a proton exchange procedure was performed on these materials to increase their hydrogen production rates. This part of the dissertation discussed the synthesized materials' structural evaluation and photocatalytic performance.

3.2 Experimental Section

3.2.1 Materials Preparation

Due to the chemicals used for this synthesis being purchased in analytical grade, the reagents were not further purified. The solid-state method was used for the synthesis of materials. Since the calcination temperature is higher than the melting point of both calcium and potassium, carbonates of these materials were added to 20% mol excess. $CaCO_3$ (Merck, precipitated GR for analysis), Na_2CO_3 (Merck, anhydrous for analysis), K_2CO_3 (Alfa Aesar, 99.0% min Granular), and Nb_2O_5 (Merck, 99+) were ground in an agate mortar for 30 minutes for the synthesis. Next, the prepared powder was pelletized using a hydraulic press (Specac Hydraulic Press) under 10 tons of pressure. The obtained pelletized sample was placed into an alumina crucible to be calcined in a high-temperature furnace (Protherm PLF 150/15). The furnace temperature was set to 1300 °C for 12 hours with a heating rate of 5 °C per minute. The pellet was re-ground until it turned into fine powder after the calcination process. The procedure stated above was also used to

synthesize doped materials by arranging their stoichiometry to have a 1.5% dopant ratio to niobium (E.g., $Kca_2NaNb_{3.94}Pt_{0.06}O_{13}$).

The hydrogen exchange process was performed by adding 0.5 grams of synthesized powders in 25 mL of 5 M HNO_3 solution. This mixture was stirred for 72 hours using a shaker (CAPP, CRP-3X) with 200 rpm. The suspension was washed with distilled water to remove excess ions and HNO_3 using centrifuge with 7500 rpm (Hettich, Rotina 380) for 5 times, and it was dried at 80 °C.

3.2.2 Structural Analysis

The crystal structure of samples was analyzed using Bruker D8 Advance X-Ray Diffractometer between 2θ values of 2° to 50° using Cu Kα radiation (λ=1.5406 Å). Zeiss Ultra Plus field emission scanning microscope is used to investigate the morphology of structures. The magnification ratio was between 500 to 1000 as minimum and between 10,000 to 20,000 as maximum. Secondary electron and In-lens detectors were used for imaging. 3.00 kV accelerating voltage and working distances between 5.5 to 4.8 mm were preferred under ultra-vacuum. Thermo Scientific K-Alpha Spectrometer, which has radiation source of Al Kα (1486.6 eV), was used for the XPS analysis. The XPS data acquired was deconvoluted using Thermo Avantage v5.973. All XPS spectra were corrected for any shift as a result of charging according to C1s at 284.5 eV. Shimadzu UV-3600 UV-VIS-NIR Spectrophotometer was used for UV-VIS measurements between 200 to 800 nm wavelengths. The measurements were performed using diffuse reflectance spectra, and the results were transformed to absorbance spectra using Kubelka-Munk function.

3.2.3 Photoelectrochemical Analysis

The films for photoelectrochemical characterizations were prepared using electrophoretic deposition technique. Electrodes were produced by cutting the fluorine-doped tin oxide (FTO) coated glasses with dimensions of 25 x 10 mm. Next, these glasses were cleaned with a mixture of distilled water and ethanol in an ultrasonic bath. 40 mg of sample powder and 10 mg of Iodine (Sigma-Aldrich, 99.8% ACS reagent) were mixed into 50 mL of acetone in a beaker. Then, the beaker was placed into an ultrasonic bath for 15 minutes. FTO-coated glasses were used as both cathode and anode and dipped into the

solution. The distance between electrodes were 1.0 cm. The films onto electrodes were deposited at 40 V potential for 10 minutes by using a DC power source (RIGOL DP811). Finally, these electrodes were heated to 400 °C with a heating rate of 5 °C per minute and kept at this temperature for an hour to improve adhesion of the films to the surface of the FTO coated glass.

A working electrode (sample coated on FTO glass), Pt foil 10 x 10 mm as the counter, and the saturated calomel electrode as the reference electrode in the solution of 0.5 M K_2SO_4 with 0.02 points per second scan rate at 1.2 V were used for photoelectrochemical characterizations. The light illumination was provided using a 500 W xenon light source (Newport, 66901).

3.2.4 Photocatalytic Hydrogen Production

For the hydrogen production experiment, 30 mg of sample powder and 15 mL of the methanol-water mixture (10% volume MeOH) were placed into a quartz vessel with a total volume of 25 mL with a rubber stopper. Then, the air inside the vessel was removed by purging the vessel via argon for 30 minutes. Next, another stopper was placed on the vessel with an outlet, and the argon flow was introduced between the two stoppers to inhibit air contamination. The vessel illuminated horizontally using a 500 W xenon light source (Newport, 66901) equipped with and without AM 1.5 filter and it was stirred with a speed of 200 rpm. The hydrogen amount inside the vessel was determined using a gas chromatogram (Shimadzu, GC-2014) using a 100 μL gas-tight syringe. The inlet temperature was 150 °C, the temperature of the MS 5A column (Teknokroma, NF-38427-FS) was 75 °C, and the temperature of the thermal conductivity detector (TCD) was 150 °C with a bridge current of 40 mA. The ideal gas equation was used for the calculation of hydrogen production amount, where it was accepted as 1.0 mol of gas occupying 22.4 L of volume. The headspace volume was 10 mL, and the intensities of the GC peaks were determined according to the calibration line that was made with different volumes of hydrogen gas.

3.3 Results and Discussion

3.3.1 X-Ray Diffraction Spectroscopy (XRD)

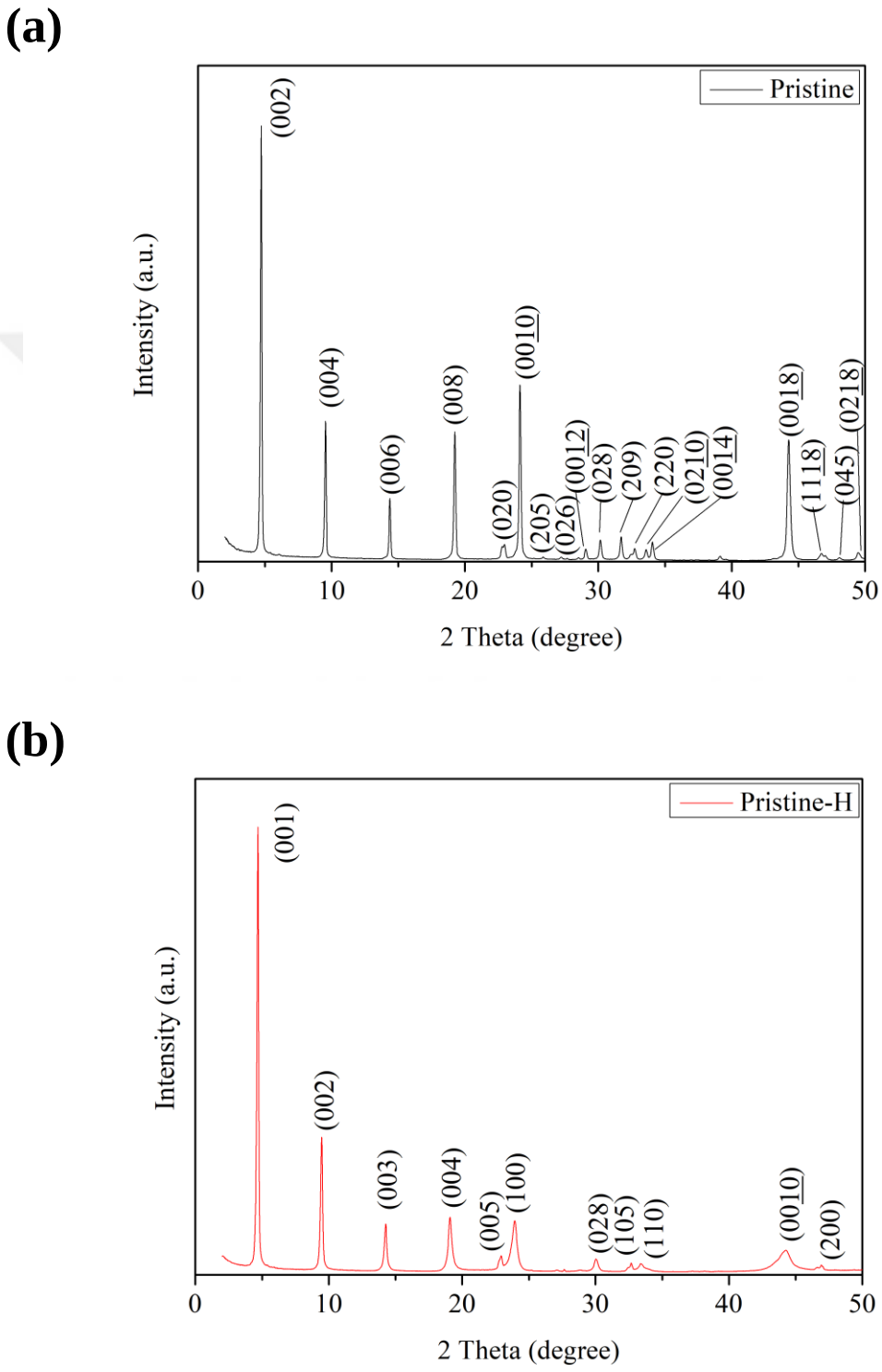

Figure 3.2. XRD patterns of pristine sample (a) before, (b) after hydrogen exchange

From the Figure 3.2, the XRD results of the pristine samples before and after the hydrogen exchange treatment indicate that the synthesis was successful due to the pattern obtained being the same as the literature[147]. The region between 0° to 20° indicates the number of the layers in the structure. No other distinguishable peak exists in this 0° to 20° region, indicating no phase impurities. Figure 3.2b shows the XRD pattern of the pristine sample after the hydrogen exchange. This pattern indicates that the primary (002), (004), (006), and (008) planes of the n = 4 phase were transformed into different planes such as (002) to (001), (002) to (004) due to hydration of the molecules and opening of the interlayer space between perovskite layers during the proton exchange process. According to previous research on $K[Ca_2Na_{n-3}Nb_nO_{3n+1}]$ phases, the amount of water in the structure affects the lattice parameter along the c-axis. Thus, it gives information regarding the effect of water molecules on XRD patterns [14,148].

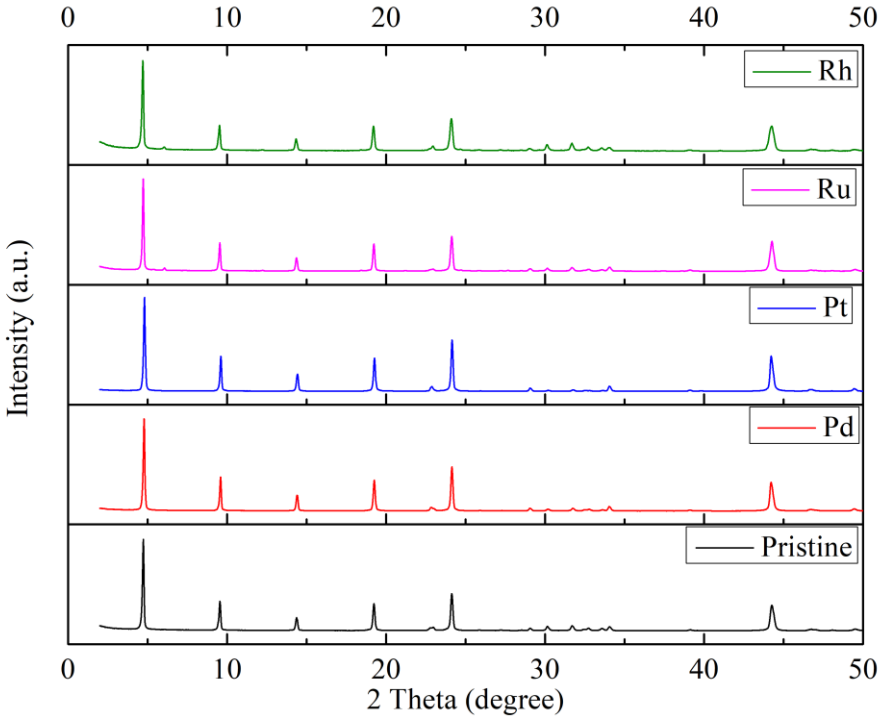

Figure 3.3. XRD patterns of untreated powders with different dopants

Figure 3.3 indicates the XRD patterns of the sample powders before the hydrogen exchange treatment. The patterns have four primary peaks between 0° and 20°, as it was stated earlier. These peaks indicate that 4-layered perovskite oxide was successfully synthesized [149]. XRD patterns of pristine, Ru, and Rh doped samples have more intense peaks around 30° to 35°. These peaks are also available for the pristine, Pd, and Pt doped

samples, yet because of the crystallinity of the samples, the peaks seem smaller compared to others. The dopant preferred for each sample may have an impact on crystallization. Since this reaction takes place at 1300 °C, potassium and calcium sources evaporate, which causes this reaction to be challenging to obtain same crystallinity. The Figure 3.3 indicates that the crystal structures of the materials are the same due to their XRD patterns alignment. XRD patterns of all the samples, which can be observed from Figure 3.4, illustrate that all the peak positions are correlated after the proton exchange treatment.

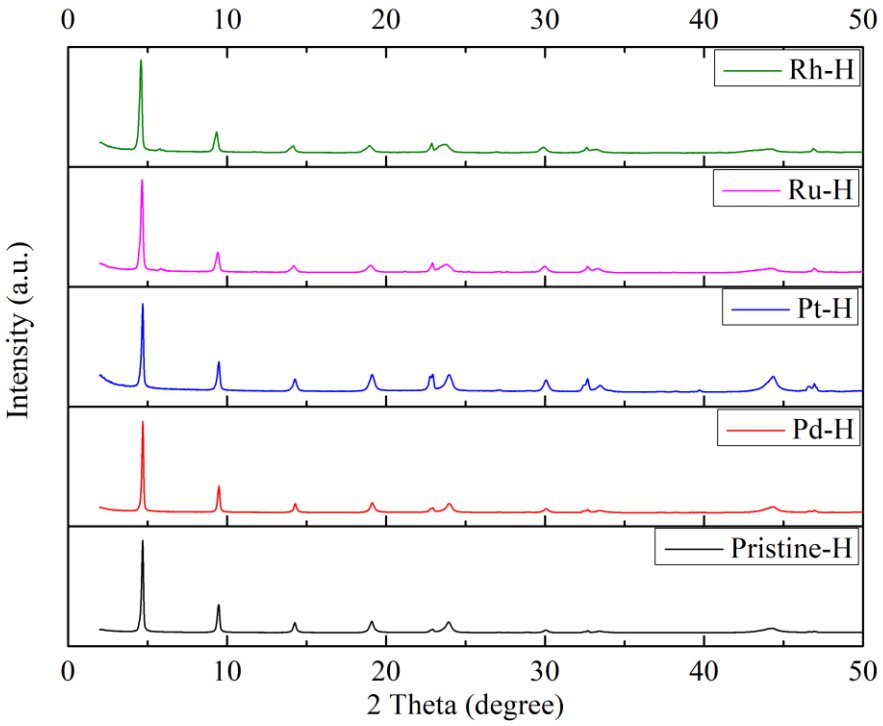

Figure 3.4. XRD patterns of proton exchanged powders with different dopants

3.3.2 Morphological Analysis

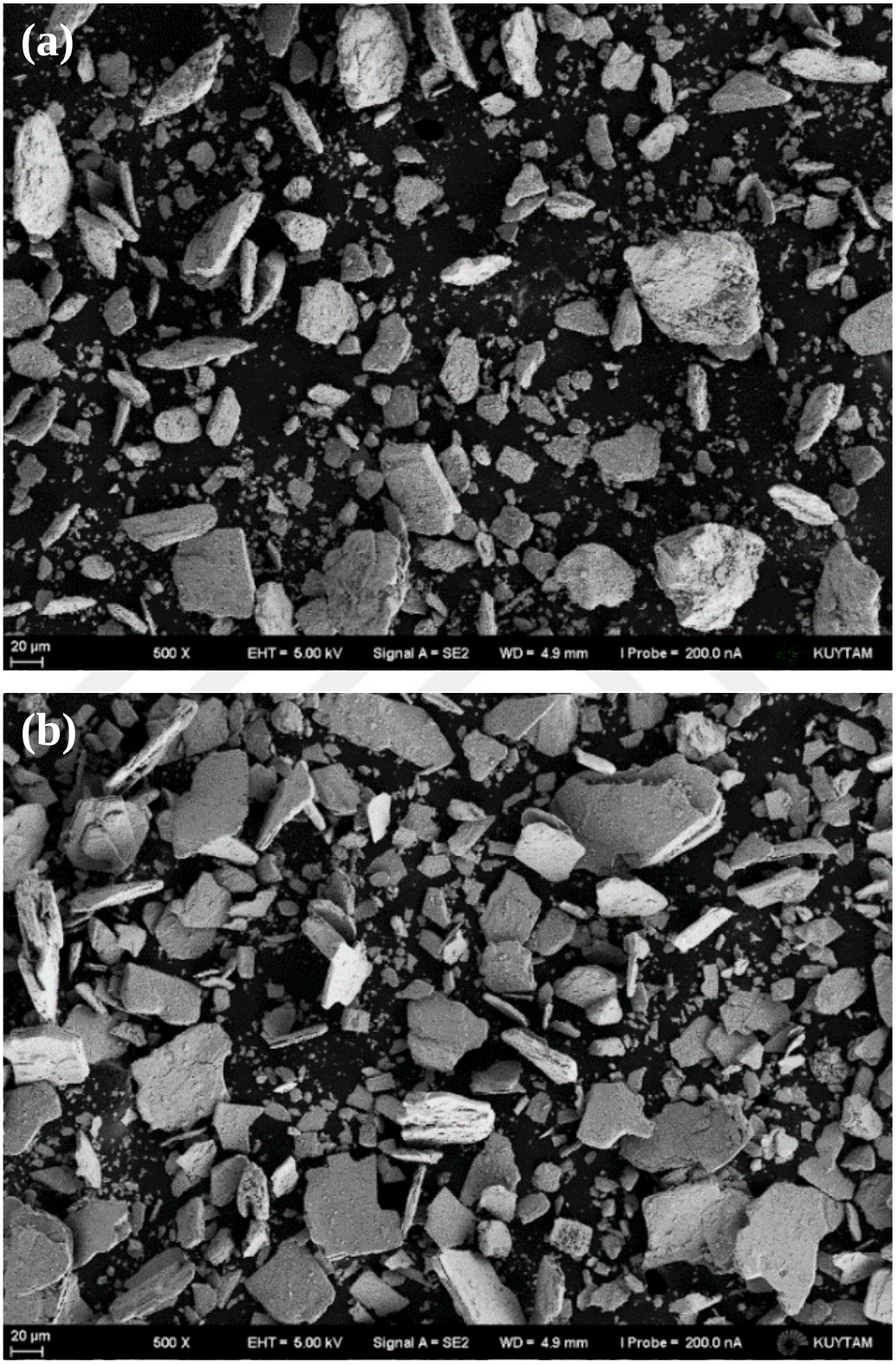

Figure 3.5. FESEM Images of pristine sample before (a), and after (b) hydrogen exchange treatment

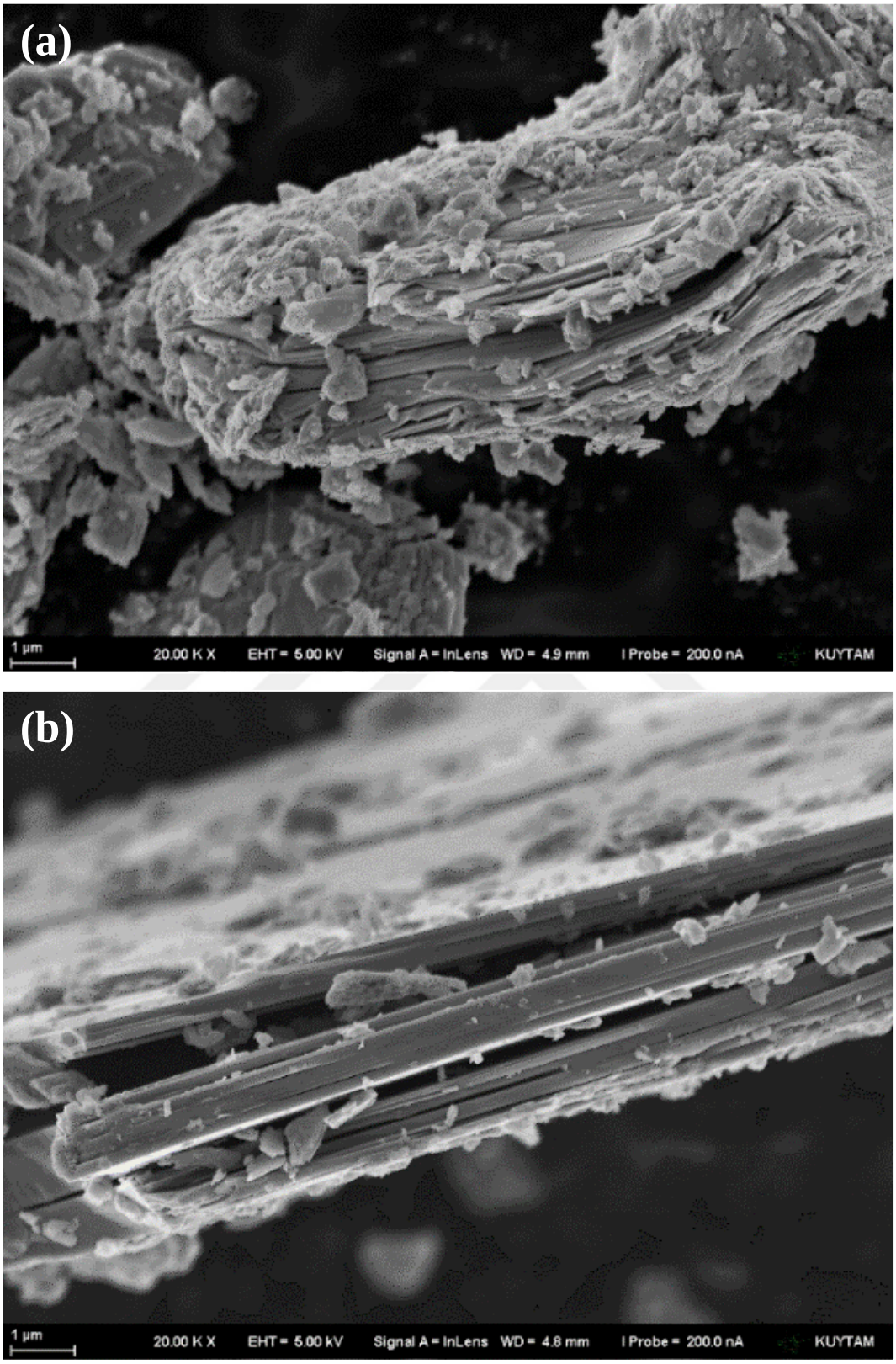

Figure 3.6. FESEM Images of pristine sample before (a), and after (b) hydrogen exchange treatment with higher magnification

Figure 3.5 and Figure 3.6 shows that the morphology of the pristine sample slightly changed after the hydrogen exchange treatment. According to Figure 3.5b, the particles appear as flakes compared to the pristine sample. Figure 3.6 indicates that this material has a layered structure. When the two images are compared, the sample before the hydrogen exchange has more small broken residues that cover the crystals' surface. On the other hand, the density of the small residues decreased after the hydrogen exchange process. Also, the alignment of the layers looks more linear, and some of the layers are separated from each other after the hydrogen exchange process. While the H^+ replaces the K^+ cations, bulky particles may divide into smaller plates. However, the morphologies of the materials were preserved due to the layered structure being intact. Figures below give general information regarding the particle size, shapes, and layered structures of the samples. The dopants did not affect the particle structure, the layers of the material are visible. This indicates that the morphology of the materials preserved. In addition, there are visible gaps between the layers after the proton exchange.

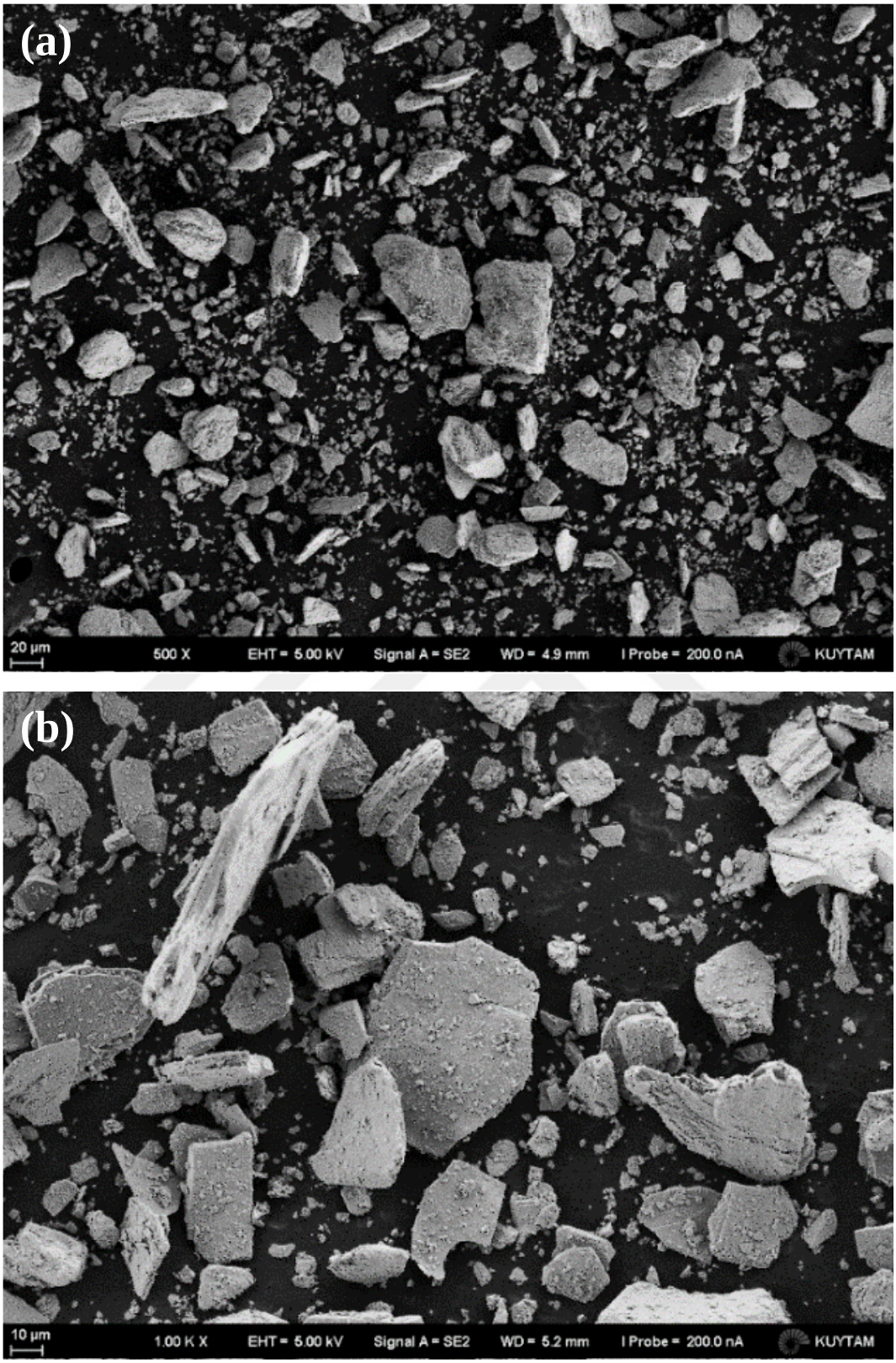

Figure 3.7. FESEM Images of Pd doped sample before (a), and after (b) hydrogen exchange treatment

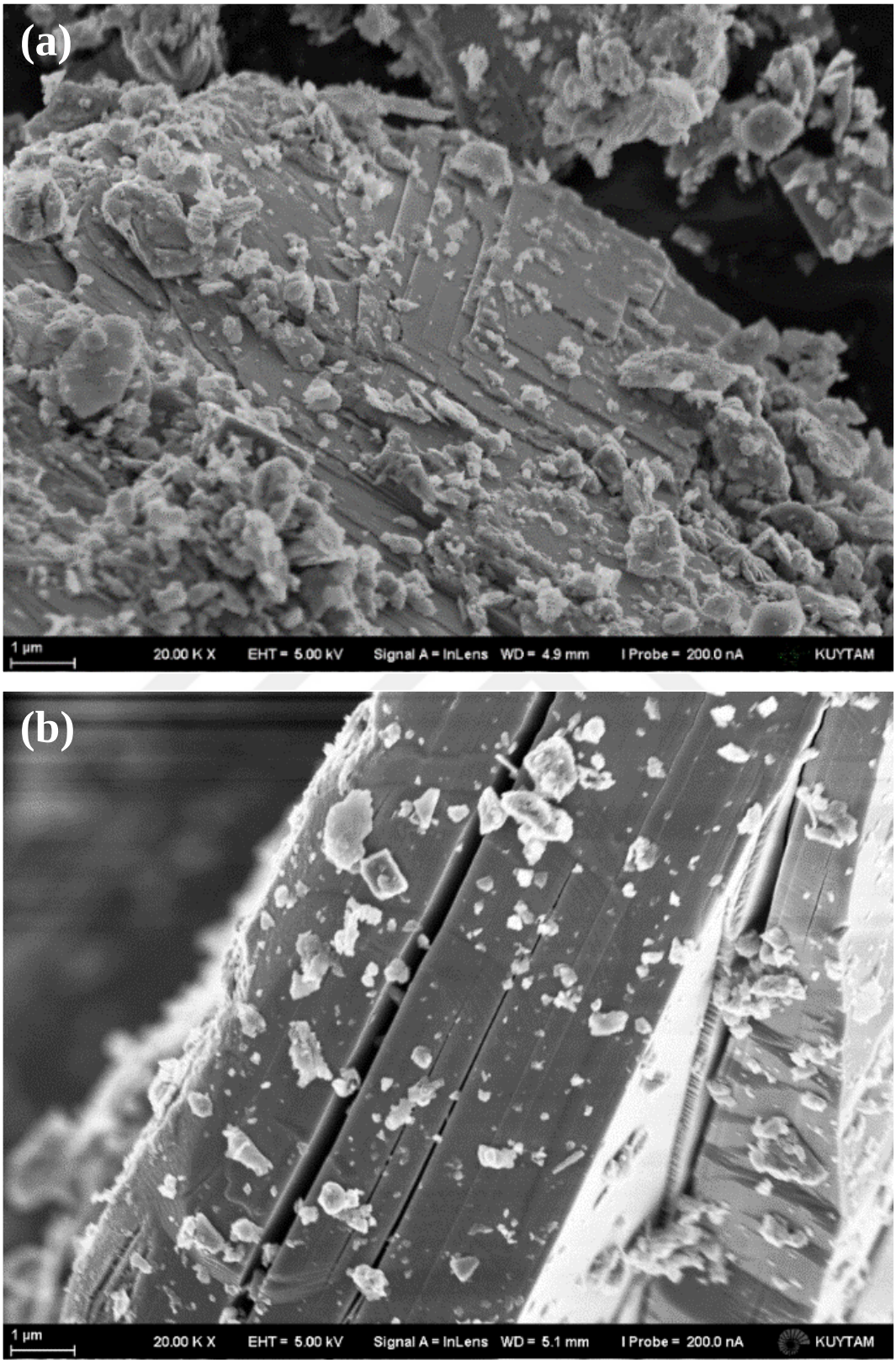

Figure 3.8. FESEM Images of Pd doped sample before (a), and after (b) hydrogen exchange treatment with higher magnification

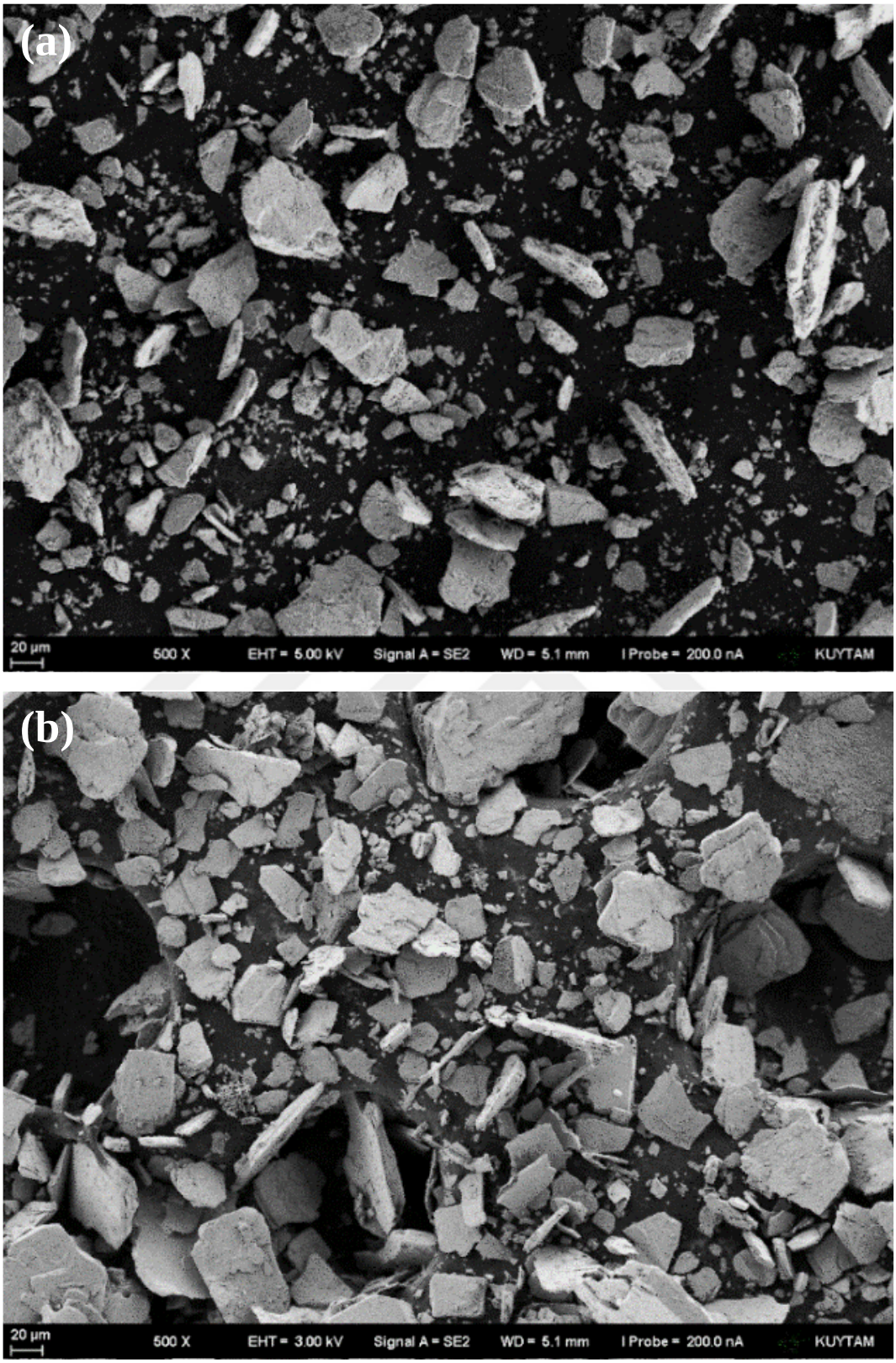

Figure 3.9. FESEM Images of Pt doped sample before (a), and after (b) hydrogen exchange treatment

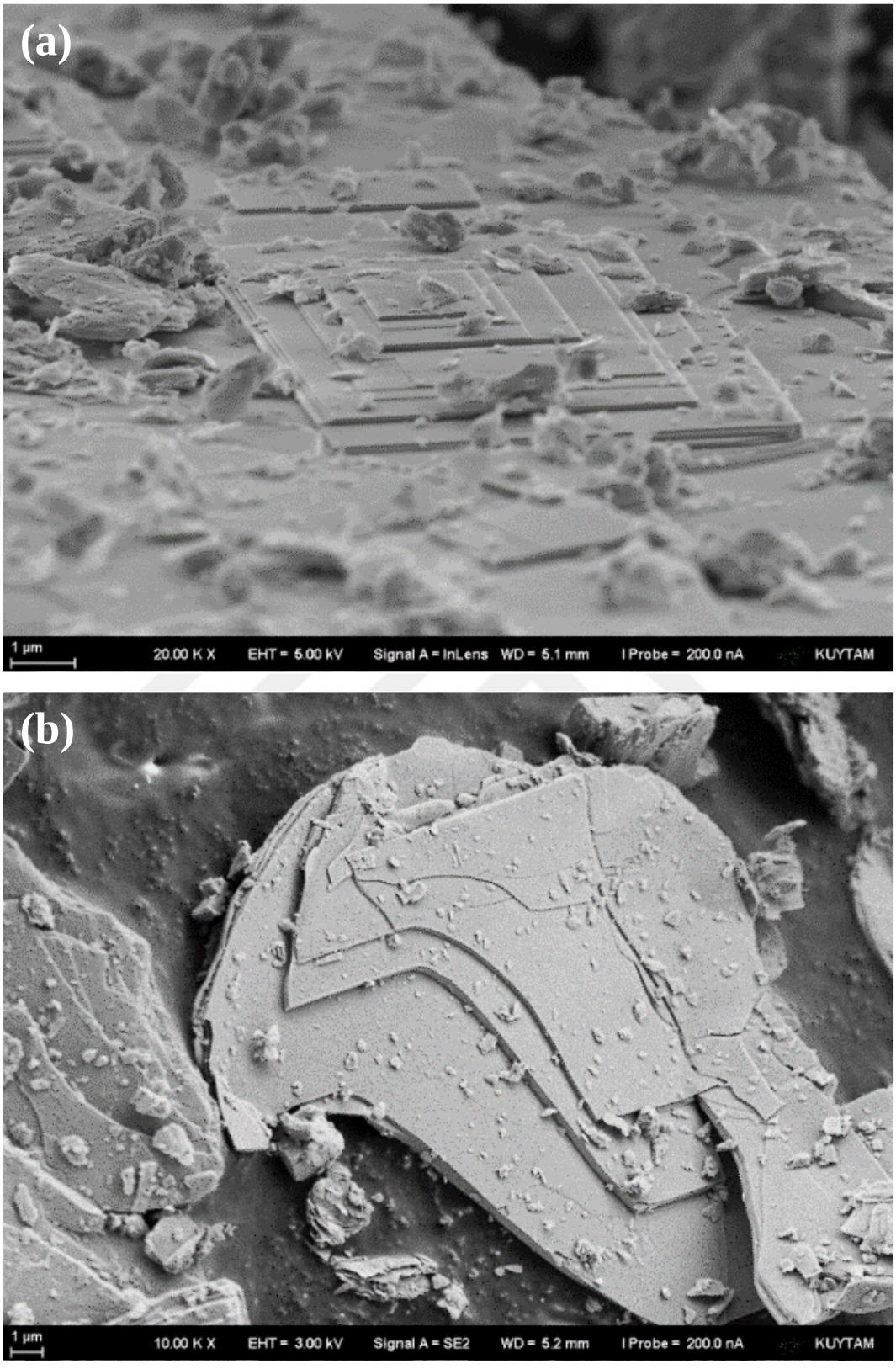

Figure 3.10. FESEM Images of Pt doped sample before (a), and after (b) hydrogen exchange treatment with higher magnification

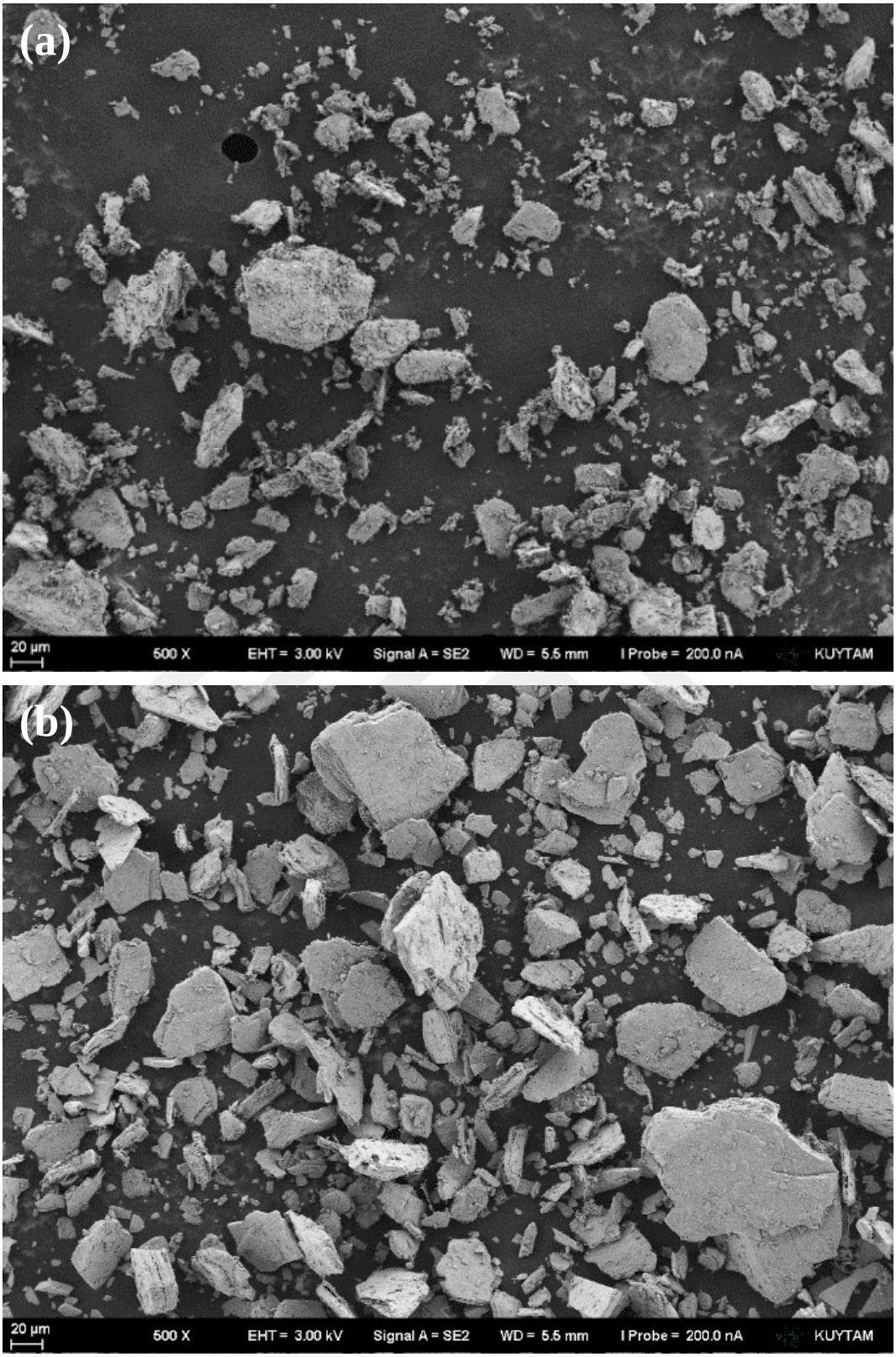

Figure 3.11. SEM Images of Ru doped sample before (a), and after (b) hydrogen exchange treatment

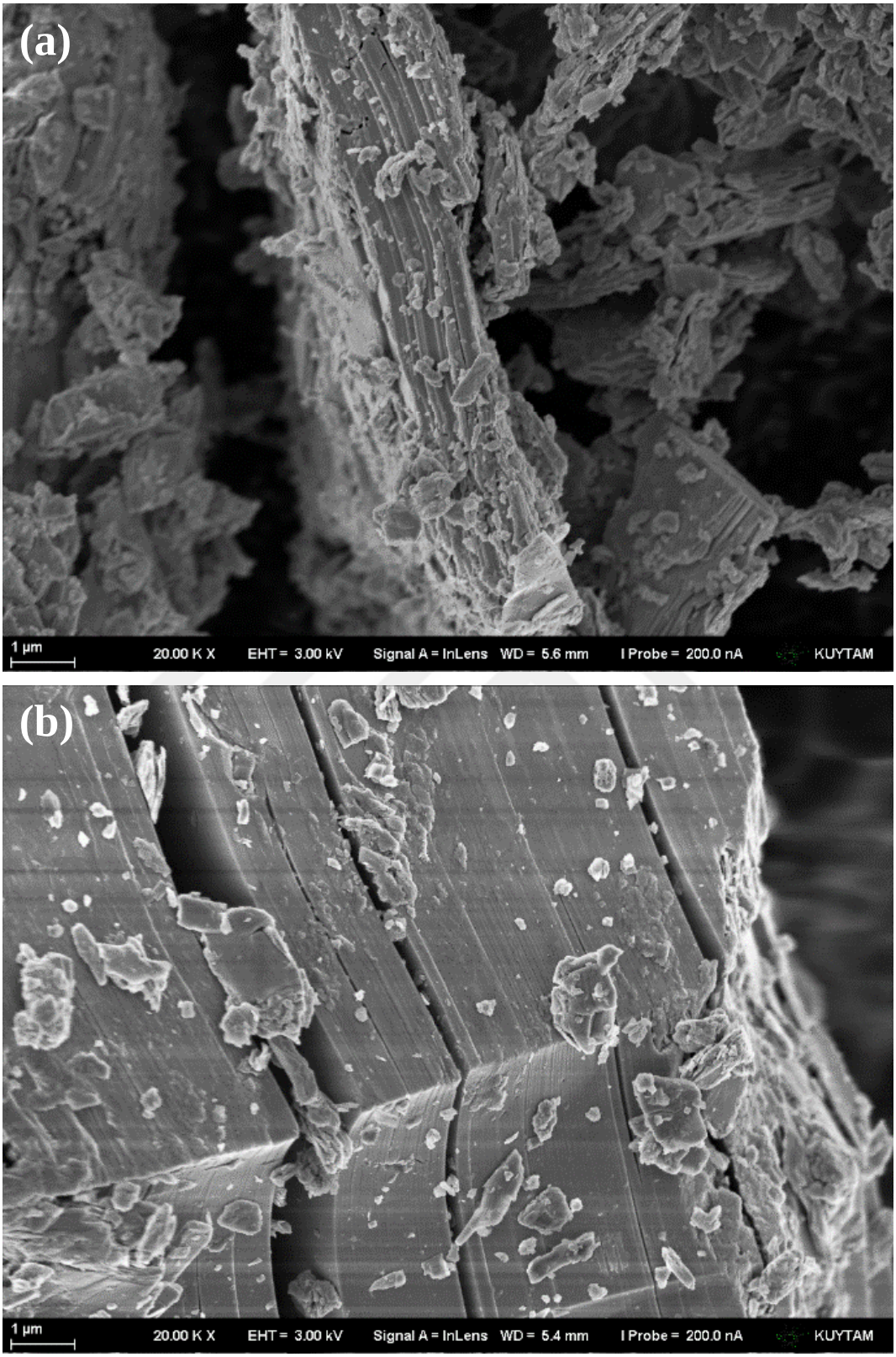

Figure 3.12. SEM Images of Ru doped sample before (a), and after (b) hydrogen exchange treatment

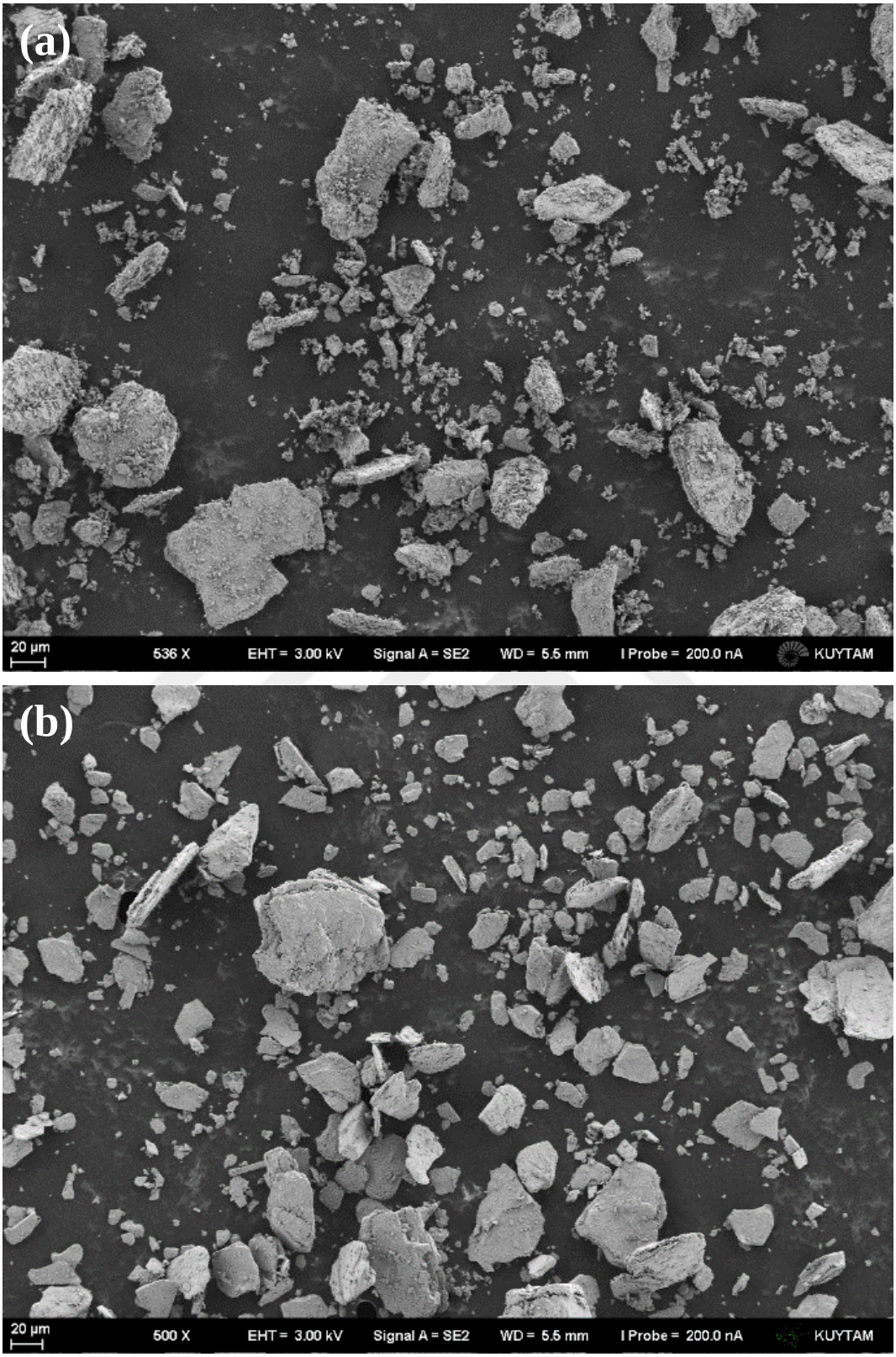

Figure 3.13. SEM Images of Rh doped sample before (a), and after (b) hydrogen exchange treatment

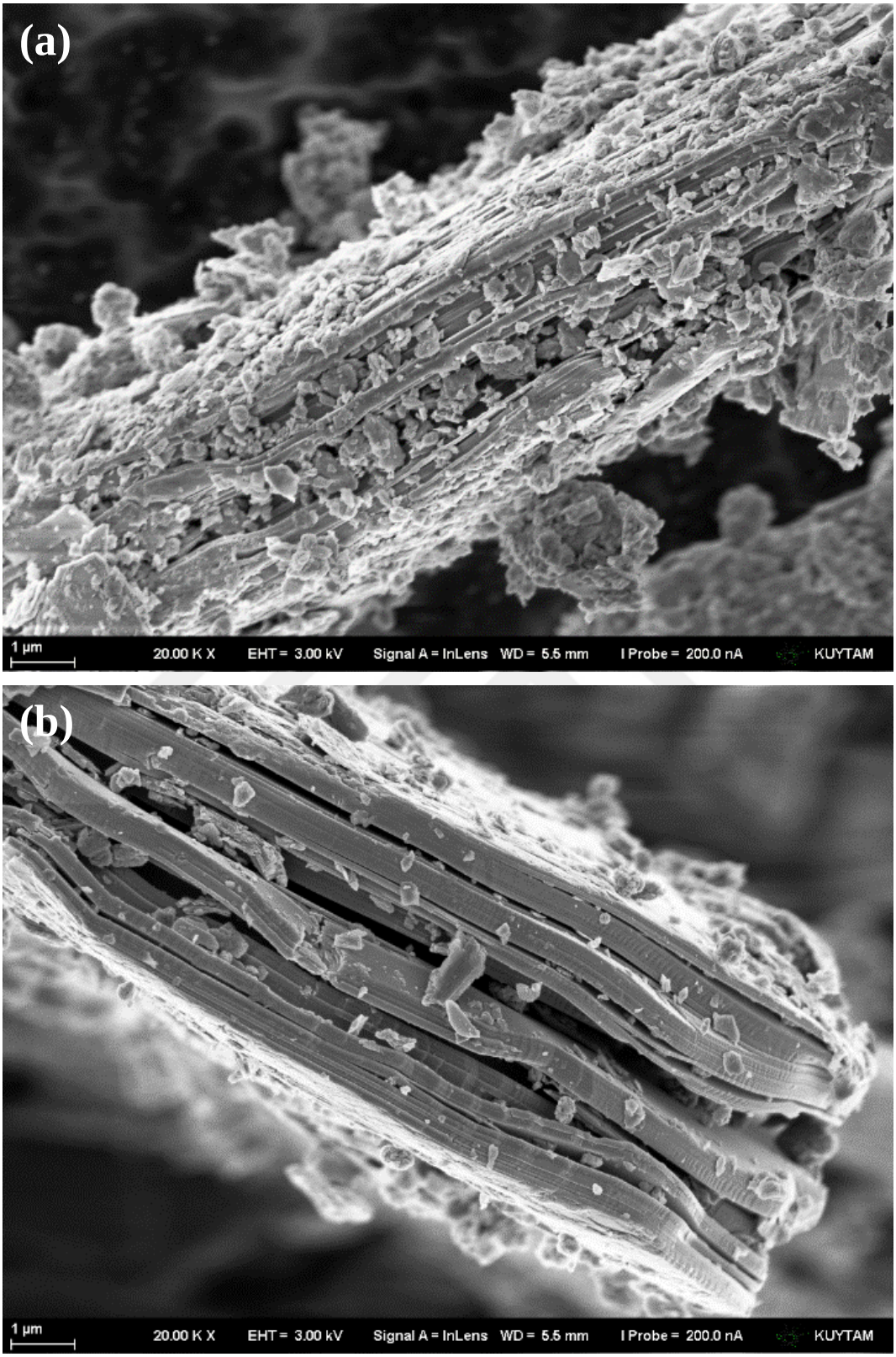

Figure 3.14. SEM Images of Rh doped sample before (a), and after (b) hydrogen exchange treatment with higher magnification

3.3.3 X-ray Photoelectron Spectroscopy (XPS)

(a)

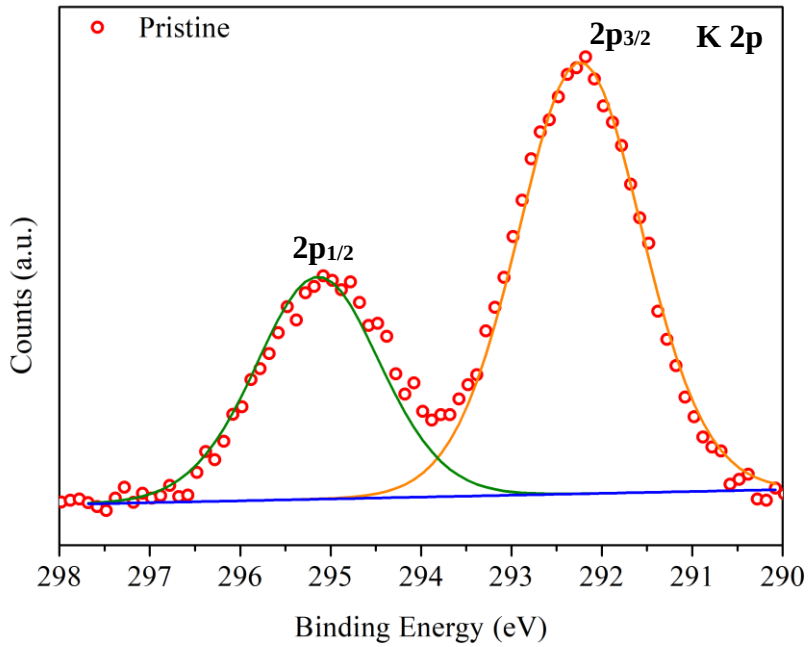

(b)

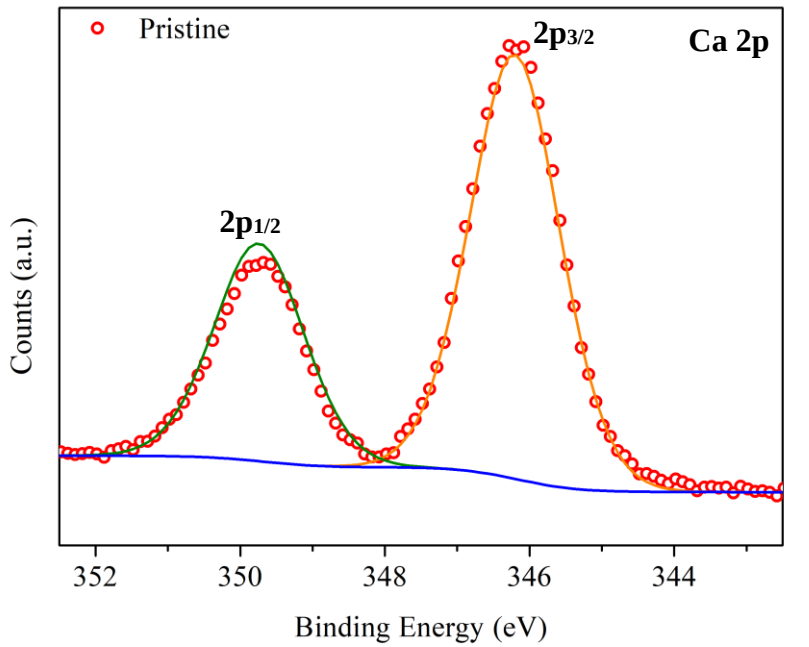

(c)

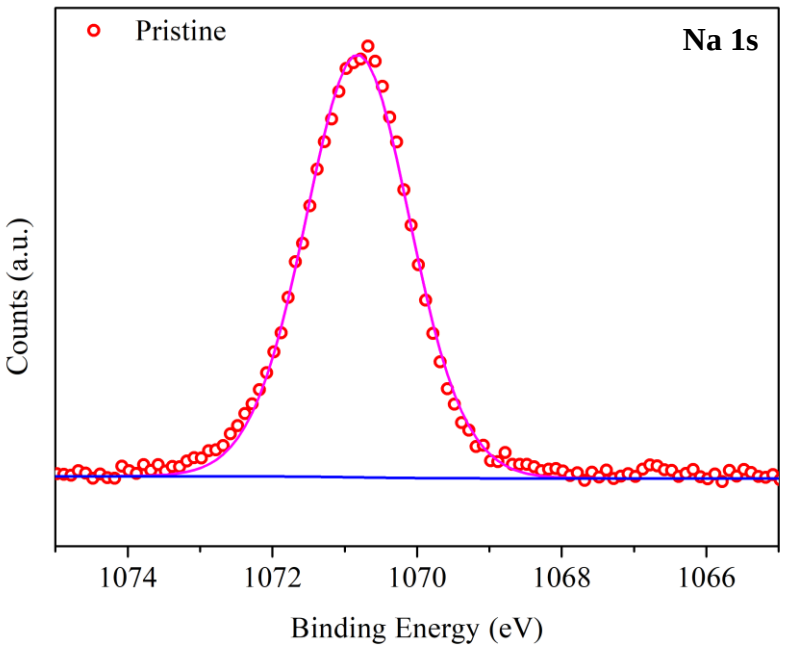
Pristine
Na 1s
Counts (a.u.)
1074
1072
1070
1068
1066
Binding Energy (eV)

(d)

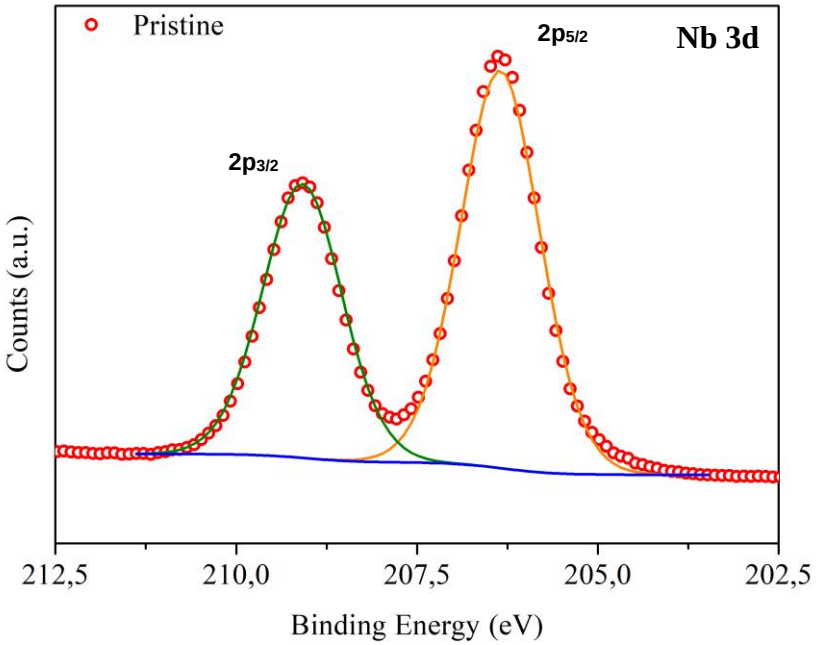
Pristine
Nb 3d
2p5/2
2p3/2
Counts (a.u.)
212,5
210,0
207,5
205,0
202,5
Binding Energy (eV)

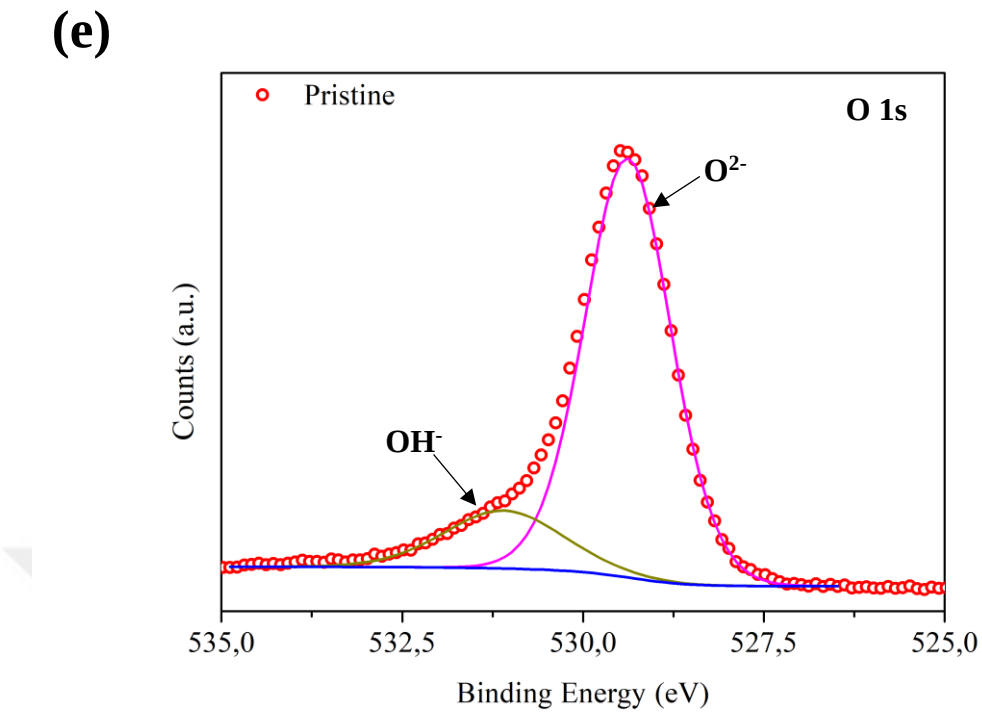

Figure 3.15. XPS spectrum of pristine material: (a) K 2p, (b) Ca 2p, (c) Na 1s, (d) Nb 3d, and (e) O 1s orbitals

We have studied the XPS data to see the effect of doping on the chemical state of the elements in the structure. It should also be noted that K, Ca, and Na elements cannot have other than their specific charges because they are in the 1A and 2A groups. The crucial elements here to evaluate with XPS characterization are Nb and O. Nb may have different charges other than +5, which is the expected charge in the perovskite structure [146]. O may have different peaks due to different oxygen-containing species with different chemical states [127]. According to the XPS spectrum of pristine material, which is shown on the fig, the K 2p scan resulted in $2p_{1/2}$ at 295.14 eV and $2p_{3/2}$ at 292.24 eV. These results indicate that the potassium present in the sample and the peak positions are consistent with the previous study [150]. For Ca 2p state, the peak positions are at 349.74 eV for $2p_{1/2}$ and at 364.20 eV $2p_{3/2}$, which are close to the values given in the literature [151,152]. Na 1s has a single peak at 1070.82 eV, which can be justified by literature [153]. There are two peaks for Nb 3d orbital. Their positions are at 206.35 eV for $3d_{5/2}$ and 209.09 eV for $3d_{3/2}$. According to the plot, the deconvolution of the peaks exactly fits the measurement. Because of this reason, it can be stated that there is single charge phase of Nb present in the structure, which is +5 [154]. O 1s orbital has two

different peaks at 529.38 eV for O^{2-} as the lattice oxygen specie, whereas there is another peak at 531.10 eV for surface adsorbed O_2 and OH^- anion [127].

3.3.4 Energy-dispersive X-ray spectroscopy (EDX)

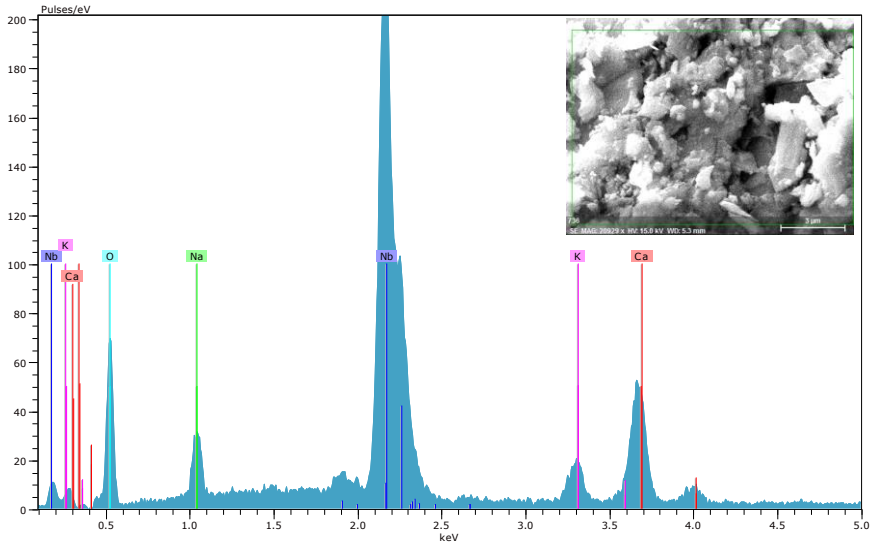

Figure 3.16. EDX result of pristine sample before hydrogen exchange

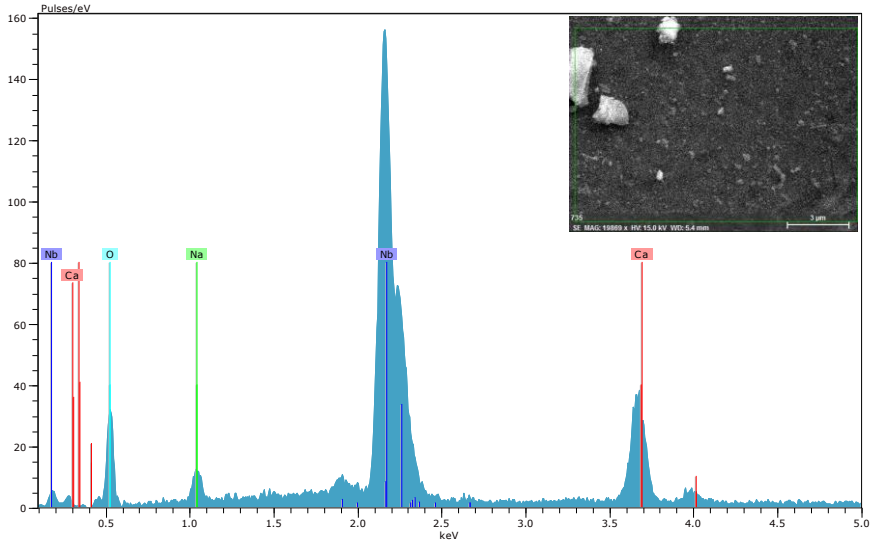

Figure 3.17. EDX result of pristine sample after hydrogen exchange

EDX results for pristine sample before (Figure 3.16) and after (Figure 3.17) proton exchange indicates that the potassium cations were successfully replaced with hydrogen element due to Figure 3.16 shows the fingerprint $K_{\alpha 1}$ value of potassium photon energy,

which is around 3.3 keV. On the other hand, Figure 3.17 does not contain $K_{\alpha 1}$ peak of potassium.

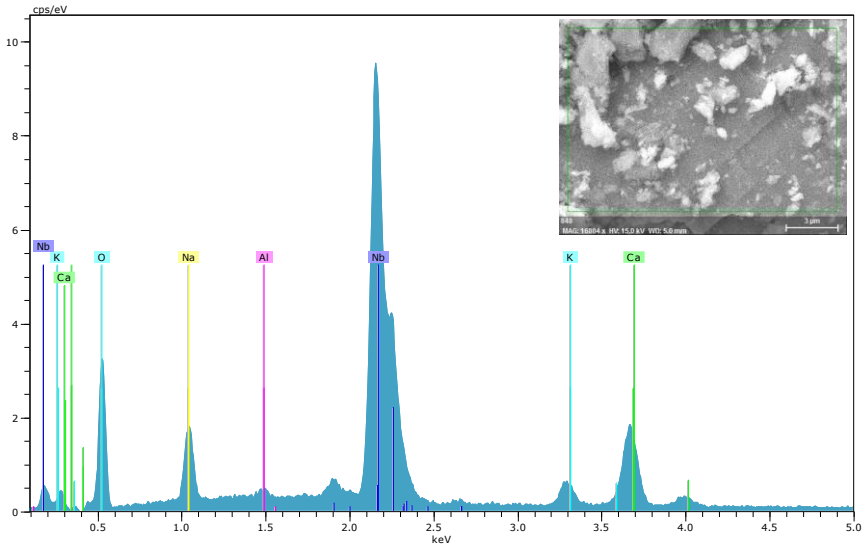

Figure 3.18. EDX result of Pd doped sample before hydrogen exchange

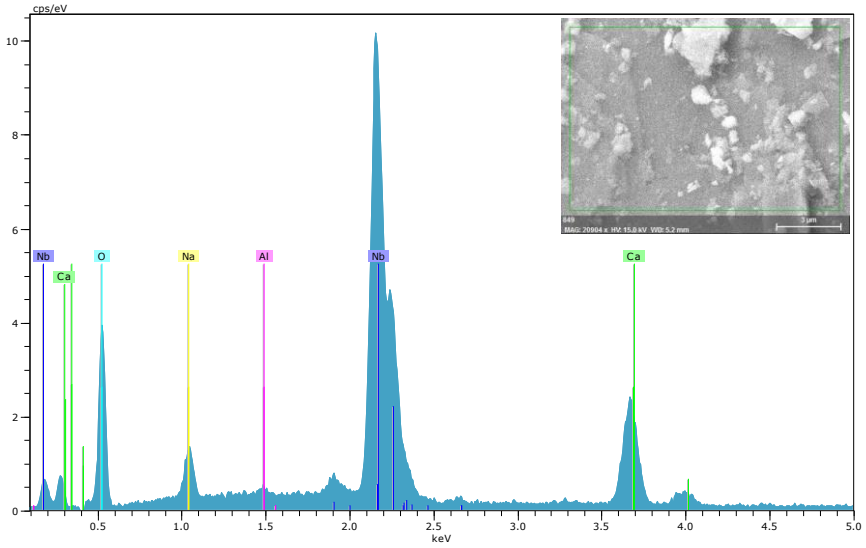

Figure 3.19. EDX result of Pd doped sample after hydrogen exchange

EDX results for Pd doped sample before (Figure 3.18) and after (Figure 3.19) proton exchange indicates that the potassium cations were successfully replaced with hydrogen element due to Figure 3.18 shows the fingerprint $K_{\alpha 1}$ value of potassium photon energy, which is around 3.3 keV. On the other hand, Figure 3.19 does not contain $K_{\alpha 1}$ peak of potassium. However, the Pd presence cannot be observed with this technique due

to percentage of the cation doped was desired as 1.5 % of total Nb atoms in the structure, which is below EDX's detection limit.

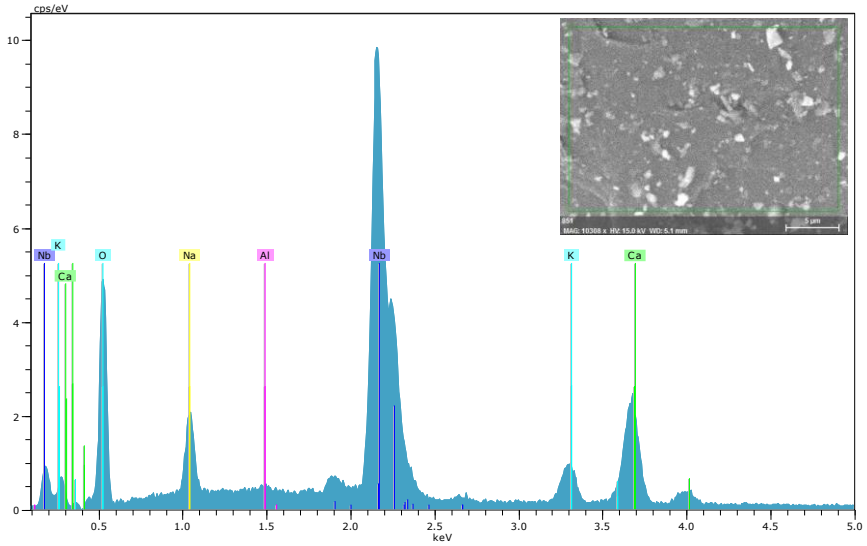

Figure 3.20. EDX result of Pt doped sample before hydrogen exchange

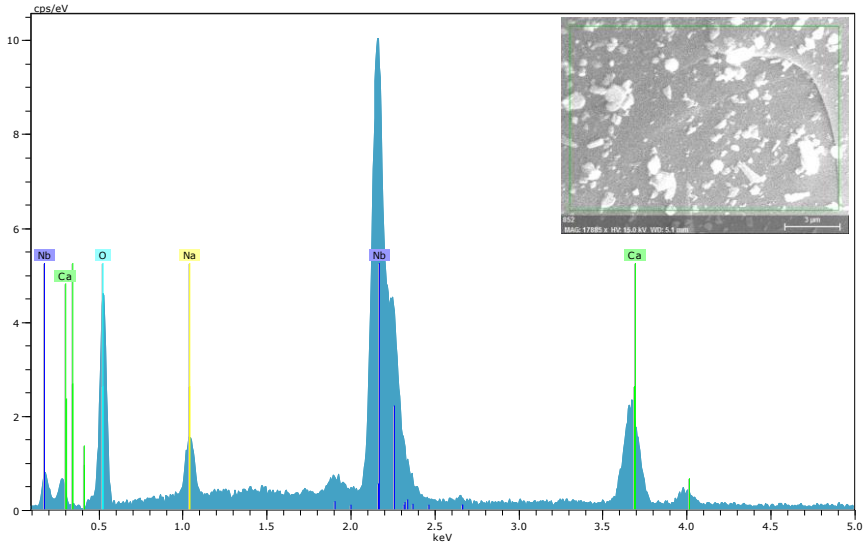

Figure 3.21. EDX result of Pt doped sample after hydrogen exchange

EDX results for Pt doped sample before (Figure 3.20) and after (Figure 3.21) indicates that the potassium cations were successfully replaced with proton due to the Figure 3.20 shows the fingerprint $K_{\alpha 1}$ value of potassium photon energy, which is around 3.3 keV. On the other hand, the Figure 3.21 does not contain $K_{\alpha 1}$ peak of potassium. Pt doping still cannot be observed for this sample, due to dopant percentage being lower than the EDX detection limit.

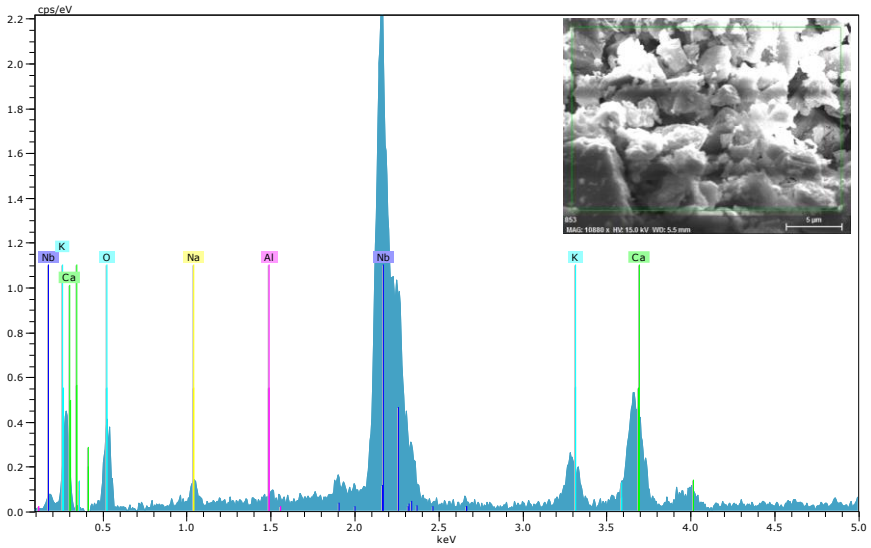

Figure 3.22. EDX result of Ru doped sample before hydrogen exchange

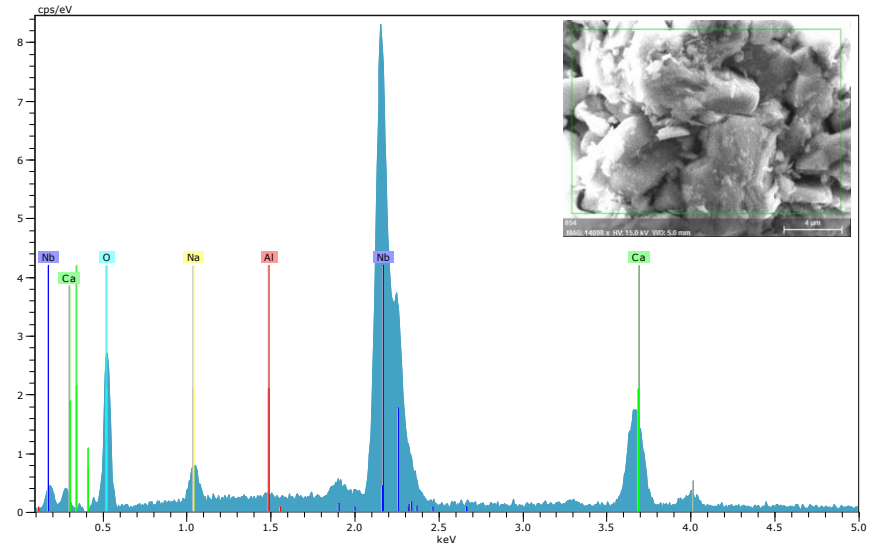

Figure 3.23. EDX result of Ru doped sample after hydrogen exchange

EDX results for Ru doped sample before (Figure 3.22) and after (Figure 3.23) indicates that the potassium cations were replaced with hydrogen element due to the Figure 3.23 shows the intensity of $K_{\alpha 1}$ value of potassium photon energy, which is around 3.3 keV was decreased significantly. Ru doping still cannot be observed for this sample, due to dopant percentage being lower than the EDX detection limit.

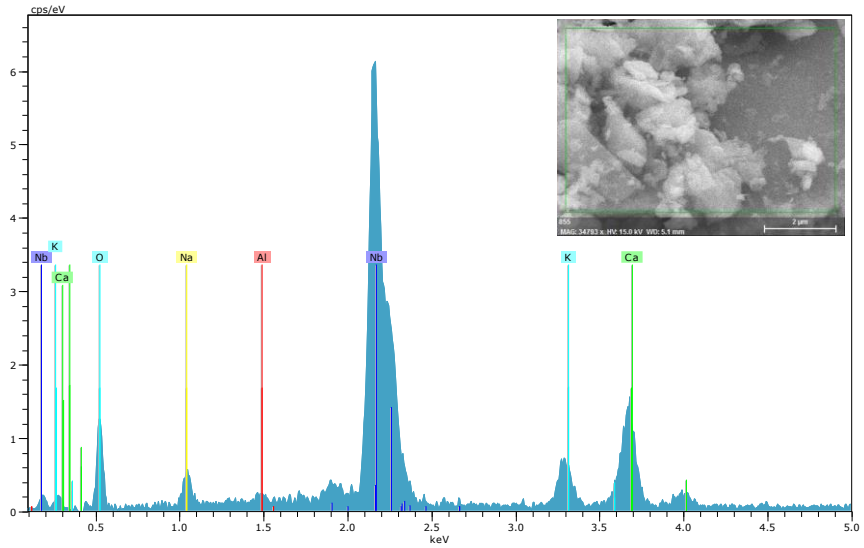

Figure 3.24. EDX result of Rh doped sample before hydrogen exchange

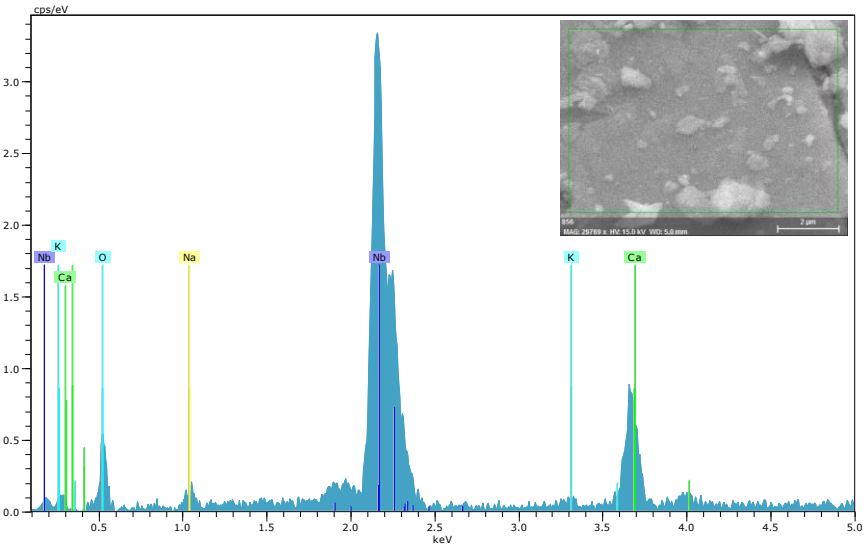

Figure 3.25. EDX result of Rh doped sample after hydrogen exchange

EDX results for Rh doped sample before (Figure 3.24) and after (Figure 3.25) indicates that the potassium cations were mostly replaced with hydrogen element due to Figure 3.25 shows the intensity of $K_{\alpha 1}$ value of potassium photon energy, which is around 3.3 keV was decreased significantly. Rh doping still cannot be observed for this sample, due to dopant percentage being lower than the EDX detection limit.

EDX results of Pristine, Pd doped, and Pt doped samples indicate that there is no potassium remaining after the hydrogen exchange treatment, where EDX results of Ru

and Rh doped samples show there is still small amount of potassium present in the structure after the hydrogen exchange process.

3.3.5 Optical Properties

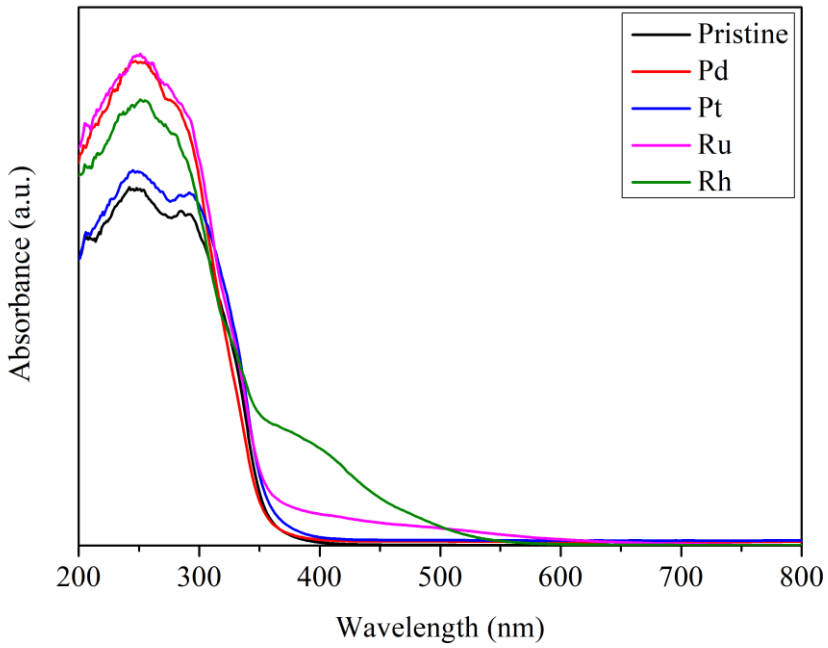

Figure 3.26. UV-VIS spectrum of the samples before the hydrogen exchange

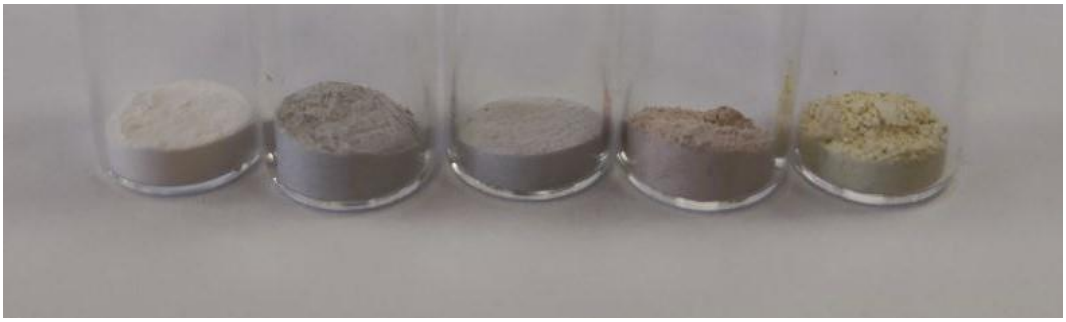

Figure 3.27. Colors of the sample powders: pristine, Pd-doped, Pt-doped, Ru-doped, and Rh-doped (from left to right)

When the colors of the samples are observed in Figure 3.27, the pristine sample has a white color, where Pd and Pt doped samples have a slightly darker white color, Ru doped sample is slightly pink, and the Rh doped sample has a yellow color. Figure 3.26 shows that the absorption edges of the samples are quite similar to each other. When the

graph is inspected in detail, the absorption edge angles of the Pd, Pt, and Rh doped samples have close values to the absorption edge angle of the pristine material. However, this occurrence does not apply to Rh doped sample. The Rh doped samples angle indicates the bandgap of this material should be distinguishably lower than the other materials. The band gap evolution with graphs of the TAUC equation will reveal the approximate band gap of these materials. It can also be seen from the figure that the Ru and Rh doped samples have absorption properties within the visible range. The area under the plot of the Rh doped sample is larger than the Ru doped sample, which may lead the higher activity in the visible region. The higher absorbance capability of the Ru and Rh doped sample may be caused by the samples' distinguishable pink and yellow colors, correspondingly.

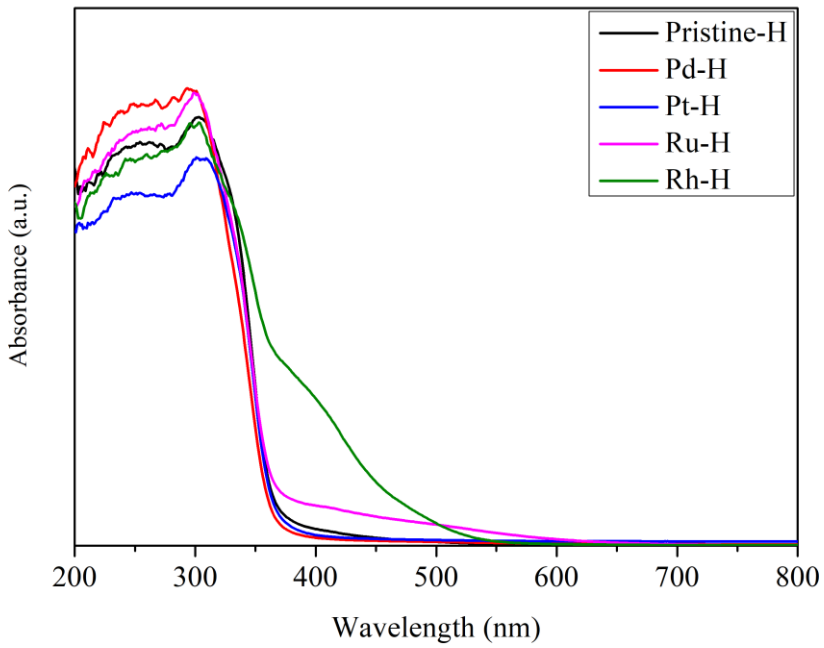

Figure 3.28. UV-VIS spectrum of the samples after the hydrogen exchange

After the hydrogen exchange treatment, the absorption edge angles of the Pd, Pt, and, Rh doped samples still have close values to the absorption edge angle of the pristine material, according to the Figure 3.28. After the proton exchange treatment, the Ru and Rh doped samples still show higher absorption percentage than the other samples after wavelengths above 350 nm. The area below the plot of the Rh doped sample is still more prominent than the Ru doped sample in the visible region. However, there is a visible

effect of the hydrogen exchange treatment on the area below the Rh doped samples plot because the absorbance percentage was slightly increased compared to the untreated Rh doped sample.

(a)

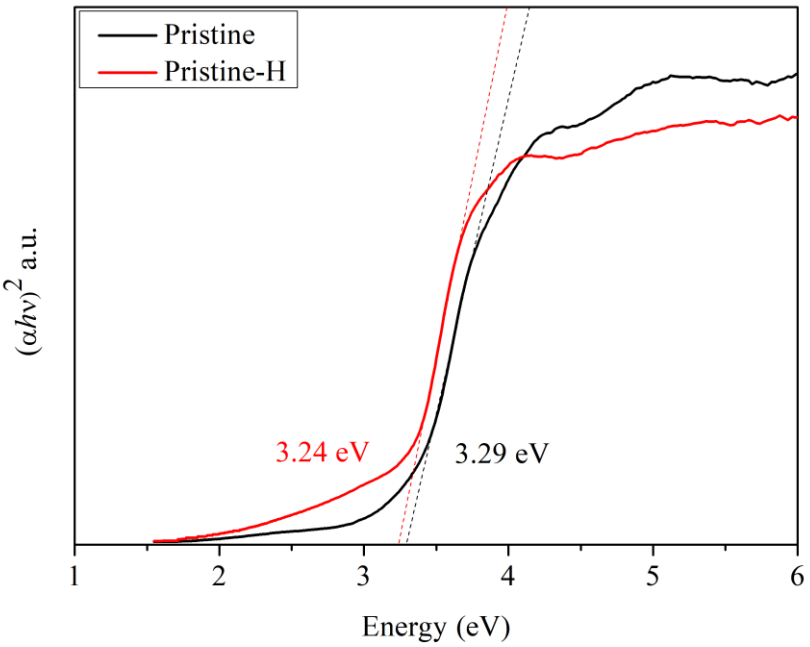

(b)

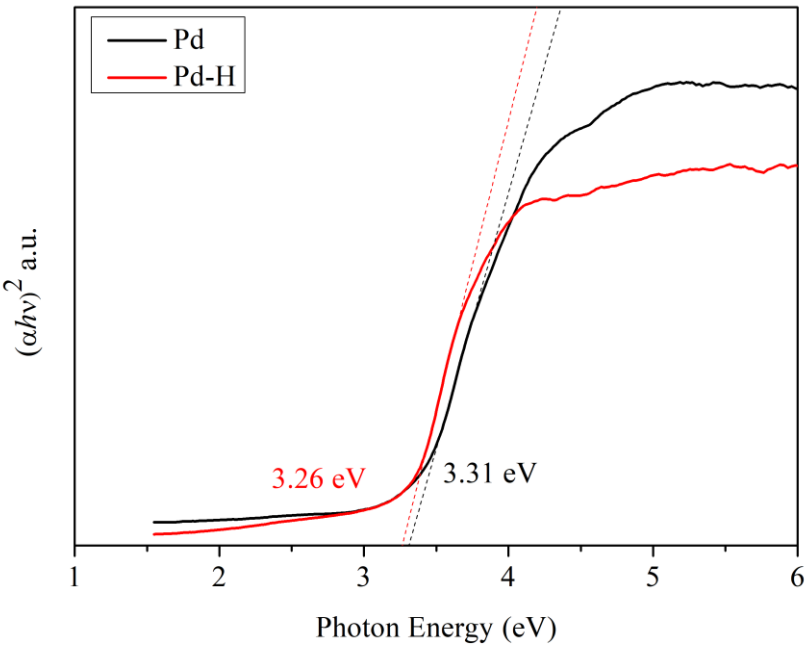

(c)

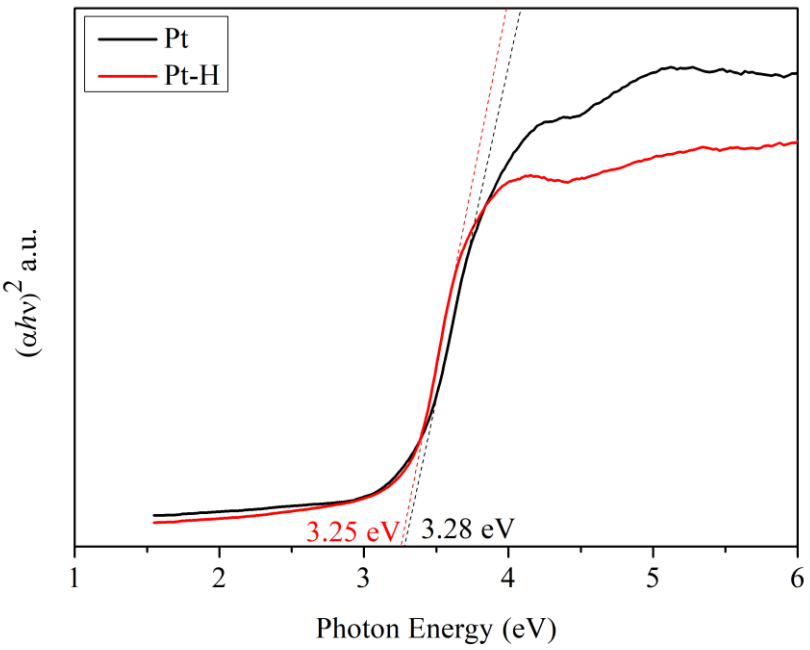
Pt
Pt-H
3.25 eV
3.28 eV
$(\alpha h\nu)^2$ a.u.
Photon Energy (eV)
1
2
3
4
5
6

(d)

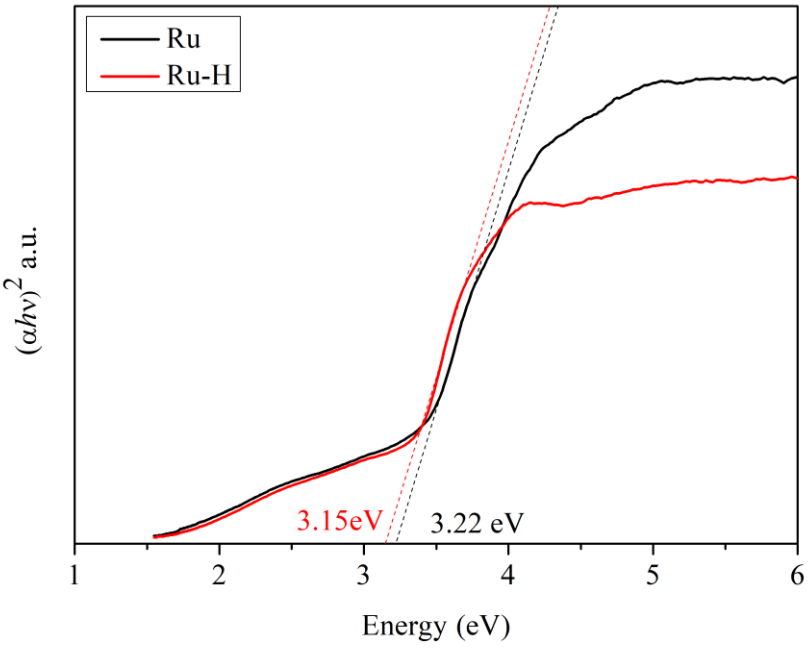
Ru
Ru-H
3.15eV
3.22 eV
$(\alpha h\nu)^2$ a.u.
Energy (eV)
1
2
3
4
5
6

(e)

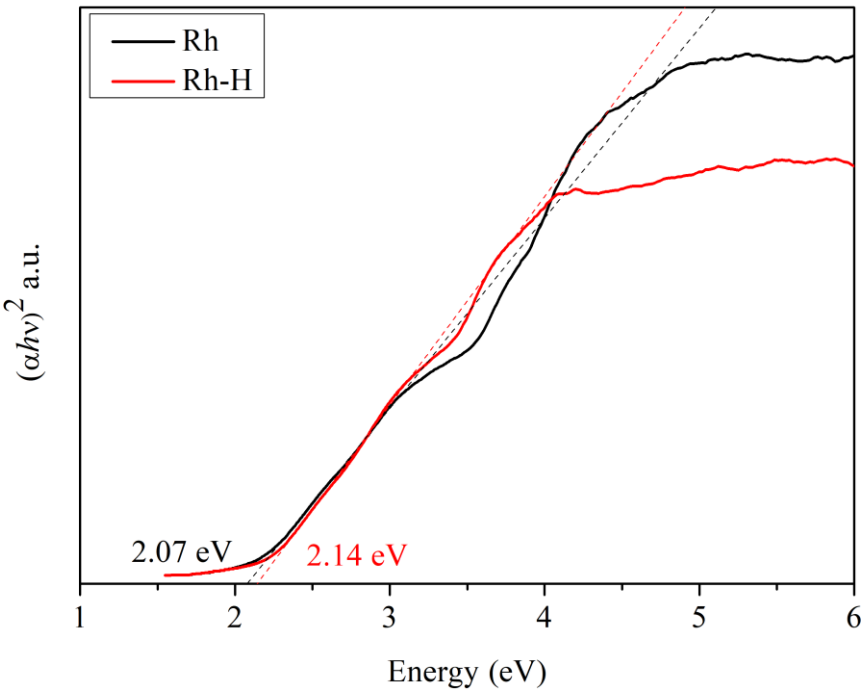

Figure 3.29. TAUC plots and estimated band gap values of samples before and hydrogen exchange treatment: (a) pristine, (b) Pd doped, (c) Pt doped, (d) Ru doped, and (e) Rh doped

Name of Dopant	Band gap – Before Hydrogen Exchange (eV)	Band gap – After Hydrogen Exchange (eV)
Pristine	3.29	3.24
Pd	3.31	3.26
Pt	3.28	3.25
Ru	3.22	3.15
Rh	2.07	2.14

Table 3.1. Estimated band gap values of all samples using TAUC equation

The values obtained from the TAUC plots, which are shown in Table 3.1, exhibit a decreasing trend for all the samples except the Rh doped one after the proton exchange. The Rh doped sample's band gap value was increased slightly after the hydrogen exchange treatment. When band gap values for the samples are compared to the pristine

sample, the changes are minimal. The band value of the Pd doped sample has the largest value both before and after the hydrogen treatment. The results indicate that the Rh doped sample shows the most dramatic band gap change, which is around 1.1 eV compared to the pristine sample. The effect of this band gap change may have a noticeable impact on the hydrogen production rate of this material.

3.3.6 Photoelectrochemical Analysis (PEC)

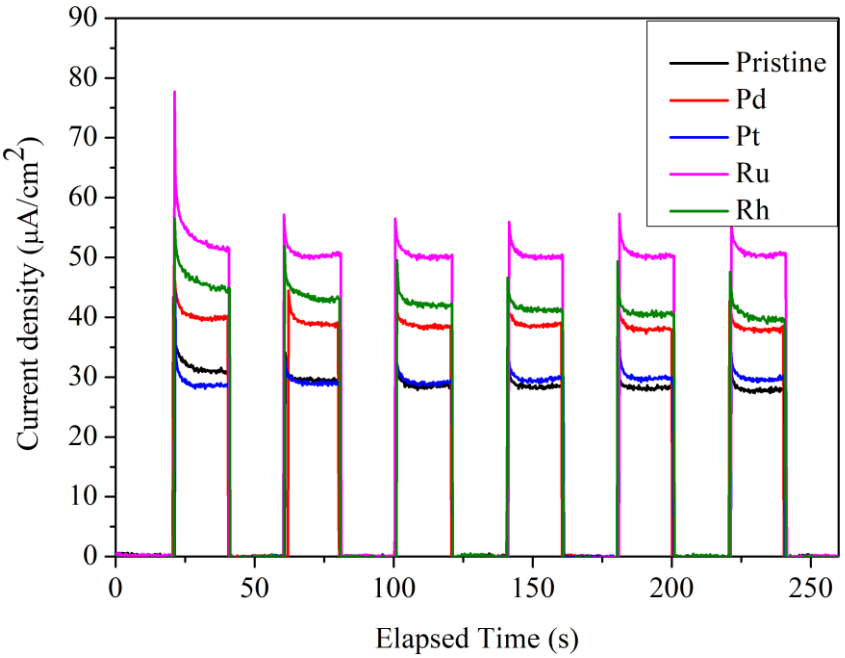

Figure 3.30. Chronoamperometry results of samples before the hydrogen exchange

Chronoamperometry results of the untreated sample can be seen from the Figure 3.30 indicates that Ru doped sample has the highest current density where the Pt doped sample has the lowest which is unexpected due to the dopant introduction should most likely increases the current density. Even though they were coated using the same method in the same period, the thickness of the films may differ. There is a trend of edge pinning for all the samples including the pristine one. Since an electrolyte (aqueous solution of K_2SO_4) is used during these measurements, the current density spikes in the beginning, and after a while, it turns back to its steady-state because of band bending. The holes created migrate to the surface and cause this phenomenon. Band bending is caused by

heterojunction of the sample semiconductor and the ions in the solution [155]. The holes created during illumination migrate to the surface of the electrode and they achieve steady state current after a while. In addition, the anodic current density values indicate that this is an n-type semiconductor.

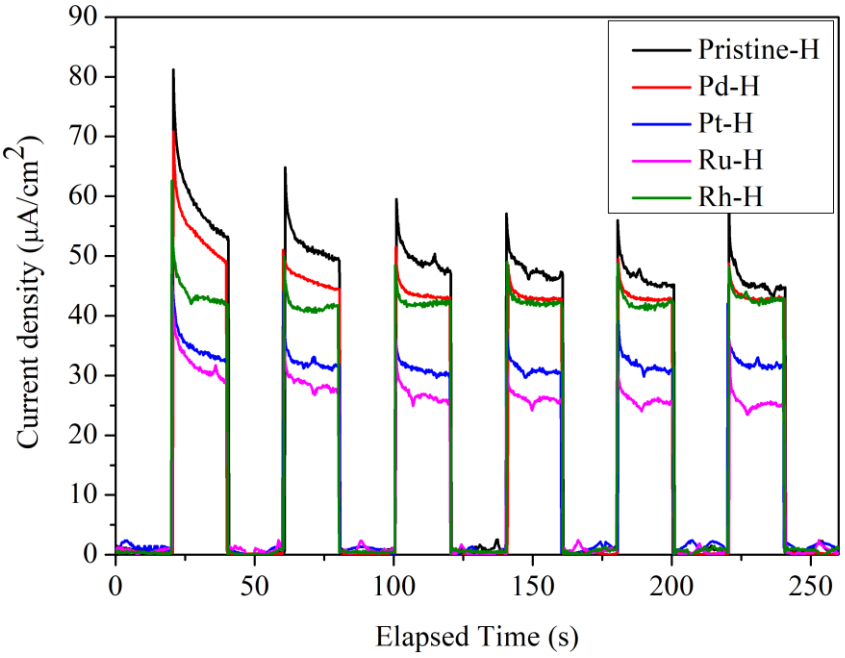

Figure 3.31. Chronoamperometry results of samples before the hydrogen exchange

The current density values after the hydrogen exchange treatment shows the similar positive amplitudes on the Figure 3.31, as well. In addition, it is still possible to observe edge pinning in the beginning of the light illumination specifically for the first peaks. The steady state is seemed to be acquired by time, which can be seen from the pristine sample's current density values due to it has higher amplitude. The high amplitude is caused by the film-thickness' effect on the conductivity. As was previously stated, there is no correlation between current density values due to potential applied and the film-thickness. The film thickness and texture can be seen from the Figure 3.32. The hydrogen exchange process resulted flake-like structures and it is possible to obtain smoother particles during this process. When the potassium was removed, there is a possibility of the separation of the layers from each other. Because of these reasons, the chronoamperometric measurements only gives information regarding the type of the

semiconductor used (n-type) and the corresponding transient photocurrent behavior, which is pinning on the edge of the photocurrent peak.

Figure 3.32. Thin films of pristine materials before proton exchange (left), after proton exchange (right)

3.3.7 Photocatalytic Hydrogen Production

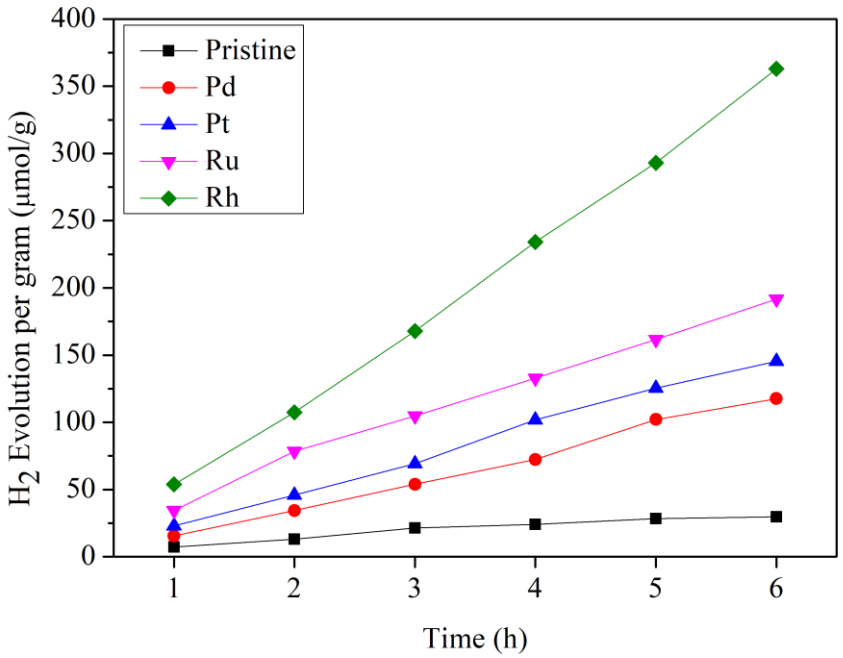

Figure 3.33. H_2 evolution results for pristine and doped $KCa_2NaNb_4O_{13}$ samples.

	H_2 amounts for samples (μmol/g)				
Time (h)	**Pristine**	**Pd**	**Pt**	**Ru**	**Rh**
1	7.22	15.54	22.90	34.41	53.79
2	13.03	34.37	45.89	78.38	107.36
3	21.34	53.88	69.33	104.80	167.77
4	24.04	72.35	101.83	132.90	234.14
5	28.38	102.05	125.36	161.56	293.00
6	29.75	117.59	145.33	191.59	362.93

Table 3.2. H_2 production of samples against time for pristine and doped $KCa_2NaNb_4O_{13}$ samples.

According to Figure 3.33 the best result of hydrogen production was obtained from the Rh doped sample, which makes sense when its band gap value (2.07 eV) is considered. Pristine material was the one that had the lowest production rate, as was expected. Rh doped, Ru doped, Pt doped, Pd doped, and the pristine material, correspondingly 362.93, 191.59, 145.33, 117.59, and 29.75 μmol/g, have the decreasing order of the hydrogen production amounts after 6 hours which can be seen from the Table 3.2. The results indicate that doping has an impact on hydrogen production. Further examination continues with the efficiency of the materials after the hydrogen exchange process.

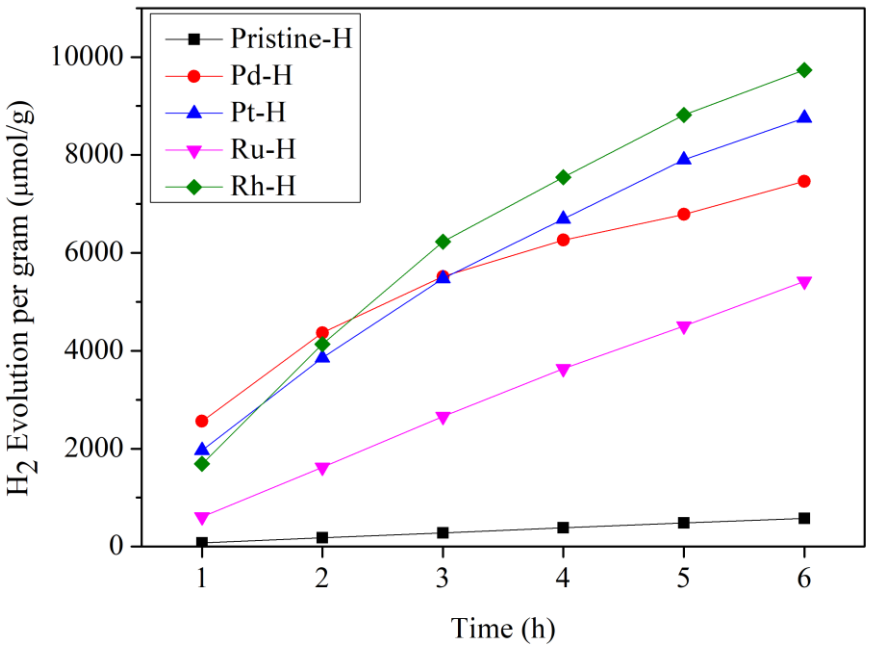

Figure 3.34. H_2 evolution results of samples for pristine and doped $HCa_2NaNb_4O_{13}$ samples.

	H_2 amounts for samples (μmol/g)				
Time (h)	**Pristine-H**	**Pd-H**	**Pt-H**	**Ru-H**	**Rh-H**
1	75.55	2559.49	1964.58	608.17	1688.95
2	178.42	4366.90	3856.17	1617.47	4131.62
3	280.02	5518.43	5478.21	2661.14	6228.24
4	383.63	6260.92	6693.31	3631.50	7547.82
5	481.39	6787.78	7903.66	4506.57	8817.53
6	577.77	7463.59	8754.32	5421.45	9736.16

Table 3.3. H_2 production of samples against time after the hydrogen exchange

Figure 3.34 and Table 3.3 show the photocatalytic hydrogen production efficiencies for the samples have decreasing order of Rh doped with 9736.16 μmol/g, Pt doped with 8754.32 μmol/g, Pd doped with 7463.59 μmol/g, Ru doped with 5421.45 μmol/g, and pristine with 577.77 μmol/g when the performances after 6 hours are evaluated. The highest production rate was achieved with Rh doped sample after the proton exchange, as it was also observed before the hydrogen exchange process. In

addition, the pristine sample exhibited the lowest hydrogen production rate as expected. The hydrogen production with the Ru doped sample, on the other hand, has the lowest rate among doped samples after the hydrogen exchange treatment. It should also be noted that the hydrogen production rates were significantly increased after the proton exchange process due to more active sites being available. Even for the pristine material, the amount of hydrogen produced increased by almost 20 folds. The increase rates are even higher for the Pd and Pt doped materials.

3.4 Conclusions

$KCa_2NaNb_4O_{13}$ and its 5% doped versions with noble metals of Pd, Pt, Ru, and Rh were synthesized in this part of the dissertation. hen, a proton exchange procedure was performed on the synthesized materials to have their hydrogen substituted variants such as $HCa_2NaNb_4O_{13}$. Their morphological, optoelectronic properties and their photocatalytic hydrogen evolution rates were determined.

According to the XRD results that are compatible with the literature, all the materials share the same pattern. The SEM results showed that the materials have the same layered morphology, indicating structural integrity. XPS results showed the presence of the elements in the structure and the charge of the Nb species was determined as +5, which was desired.

The UV-VIS spectroscopy was used to determine the absorbance properties, and the TAUC plots were used to calculate the bandgap values. According to the calculations, the bandgap values for these materials were found as 3.29 eV and 3.24 eV for pristine; 3.31 eV and 3.26 eV for Pd doped; 3.28 eV and 3.25 eV for Pt doped; 3.22 eV and 3.15 eV for Ru doped; 2.07 eV and 2.14 eV for Rh doped before and after proton exchange correspondingly. The PEC measurements showed that these materials are n-type semiconductors.

The photocatalytic hydrogen production rates were determined as 4.96, 19.60, 24.22, 31.93, and 60.49 $g\mu mol^{-1}h^{-1}$ for pristine, Pd doped, Pt doped, Ru doped, and Rh doped correspondingly before hydrogen exchange under UV illumination. 96.30, 1242.27, 1459.05, 903.58, and 1622.69 $g\mu mol^{-1}h^{-1}$ for pristine, Pd doped, Pt doped, Ru doped, and Rh doped correspondingly after hydrogen exchange under UV illumination.

The results showed that Rh doping is the most efficient way to increase hydrogen production rates. In addition, the hydrogen exchange procedure has a significant impact on the hydrogen production rates, as well.

Chapter 4: **Conclusions and Future Works**

Morphological analysis, optical properties, and measurements of photocatalytic hydrogen production rates were determined for Ruddlesden-Popper and Dion-Jacobson layered perovskite oxides. Ruddlesden-Popper type of layered perovskite oxides choice was copper and nitrogen doped Sr_2TiO_4 due to there are many examples of similar work in the literature [12,29,30,125,133]. Nitrogen doping is a known method for increasing photocatalytic water-splitting efficiency [99,123,134,146]. However, there is no example of copper doping to Sr_2TiO_4 studied before, which indicates novelty of this work. The copper and nitrogen co-doping increased the efficiency of hydrogen production under both UV and simulated sunlight equipping AM-1.5 filter. Co-doped sample has the rate of 163.08 $g\mu mol^{-1}h^{-1}$ of hydrogen produced under UV illumination, and 125.25 $g\mu mol^{-1}h^{-1}$ of hydrogen produced under simulated sunlight illumination after 6 hours.

There are still many possible variations that can be tried for the photocatalytic hydrogen production with the Sr_2TiO_4. Both Sr and Ti can be doped with corresponding suitable elements. In addition, the bandgap and the water-splitting efficiencies of the perovskite oxides can be altered by changing the amount of the oxygen in the lattice. Lehuta et al. showed that the electronic properties of Sr_2TiO_4 can be changed reducing it with $NaBH_4$ [156]. Also, perovskite structure allows using different anions of halides [29,157] and chalcogenides [158]. The hydrogen exchange method can also be used for bandgap engineering, as well [12]. Yet according to the previous experiment we conducted, using nitric acid for this purpose is not applicable due to the structure of the material being destroyed completely. There are not many research examples of $Sr_{n+1}Ti_nO_{3n+1}$ and its derivatives in the literature. It may be useful to conduct research regarding this family of strontium titanates for photocatalytic investigation.

The same evaluation methods were also done to the Dion-Jacobson phase pristine and noble metal (Pd, Pt, Ru, and Rh) doped $KCa_2NaNb_4O_{13}$. In addition, these materials were proton exchanged to determine this procedures impact on structural and electronic properties; as well as photocatalytic hydrogen production. The motivation for this study was that there not many examples of n= 4 phase niobate in the literature. Furthermore, there are no examples of Pd and Pd doping to niobates. The results showed that the best sample for photocatalytic hydrogen production was Rh doped proton exchanged one with hydrogen evolution rate of 1622.69 $g\mu mol^{-1}h^{-1}$.

There are similar methods of improvement can be applied for this material to increase its water-splitting efficiency like it was described for the titanate.

Bibliography

[1] E. Grabowska, Selected perovskite oxides: Characterization, preparation and photocatalytic properties—A review, Appl. Catal. B Environ. 186 (2016) 97–126. https://doi.org/10.1016/j.apcatb.2015.12.035.

[2] T. Ishihara, Inorganic Perovskite Oxides, in: 2017: pp. 1–1. https://doi.org/10.1007/978-3-319-48933-9_59.

[3] X. Hou, J. Ren, F. Li, C. Ma, X. Zhang, H. Feng, Research progress of perovskite materials as catalysts, IOP Conf. Ser. Earth Environ. Sci. 295 (2019) 032020. https://doi.org/10.1088/1755-1315/295/3/032020.

[4] S.J. Skinner, Recent advances in Perovskite-type materials for solid oxide fuel cell cathodes, Int. J. Inorg. Mater. 3 (2001) 113–121. https://doi.org/10.1016/S1466-6049(01)00004-6.

[5] W. Zhou, J. Sunarso, M. Zhao, F. Liang, T. Klande, A. Feldhoff, A Highly Active Perovskite Electrode for the Oxygen Reduction Reaction Below 600 °C, Angew. Chemie Int. Ed. 52 (2013) 14036–14040. https://doi.org/10.1002/anie.201307305.

[6] H. Tanaka, M. Misono, Advances in designing perovskite catalysts, Curr. Opin. Solid State Mater. Sci. 5 (2001) 381–387. https://doi.org/10.1016/S1359-0286(01)00035-3.

[7] Y. Hu, L. Mao, X. Guan, K.A. Tucker, H. Xie, X. Wu, J. Shi, Layered perovskite oxides and their derivative nanosheets adopting different modification strategies towards better photocatalytic performance of water splitting, Renew. Sustain. Energy Rev. 119 (2020) 109527. https://doi.org/10.1016/j.rser.2019.109527.

[8] G. Zhang, G. Liu, L. Wang, J.T.S. Irvine, Inorganic perovskite photocatalysts for solar energy utilization, Chem. Soc. Rev. 45 (2016) 5951–5984. https://doi.org/10.1039/C5CS00769K.

[9] S. Tan, F. Sayed, S. Yang, Z. Li, J. Wu, P.M. Ajayan, Strong Effect of B-Site Substitution on the Reactivity of Layered Perovskite Oxides Probed via Isopropanol Conversion, ACS Mater. Lett. 1 (2019) 230–236.

https://doi.org/10.1021/acsmaterialslett.9b00095.

[10] S. Liu, H. Luo, Y. Li, Q. Liu, J.-L. Luo, Structure-engineered electrocatalyst enables highly active and stable oxygen evolution reaction over layered perovskite $LaSr_3Co_{1.5}Fe_{1.5}O_{10-\delta}$, Nano Energy. 40 (2017) 115–121. https://doi.org/10.1016/j.nanoen.2017.08.007.

[11] X. Sun, Y. Mi, F. Jiao, X. Xu, Activating Layered Perovskite Compound Sr_2TiO_4 via La/N Codoping for Visible Light Photocatalytic Water Splitting, ACS Catal. 8 (2018) 3209–3221. https://doi.org/10.1021/acscatal.8b00369.

[12] B.S. Kwak, J.Y. Do, N.-K. Park, M. Kang, Surface modification of layered perovskite Sr_2TiO_4 for improved CO_2 photoreduction with H_2O to CH_4, Sci. Rep. 7 (2017) 16370. https://doi.org/10.1038/s41598-017-16605-w.

[13] G. Zhang, X. Zhang, Y. Meng, G. Pan, Z. Ni, S. Xia, Layered double hydroxides-based photocatalysts and visible-light driven photodegradation of organic pollutants: A review, Chem. Eng. J. 392 (2020) 123684. https://doi.org/10.1016/j.cej.2019.123684.

[14] A.J. Jacobson, J.T. Lewandowski, J.W. Johnson, Ion exchange of the layered perovskite $KCa_2Nb_3O_{10}$ by protons, J. Less Common Met. 116 (1986) 137–146. https://doi.org/10.1016/0022-5088(86)90224-9.

[15] Y. Ebina, Study on exfoliation of layered perovskite-type niobates, Solid State Ionics. 151 (2002) 177–182. https://doi.org/10.1016/S0167-2738(02)00707-5.

[16] J. Yoshimura, Y. Ebina, J. Kondo, K. Domen, A. Tanaka, Visible light-induced photocatalytic behavior of a layered perovskite-type rubidium lead niobate, $RbPb_2Nb_3O_{10}$, J. Phys. Chem. 97 (1993) 1970–1973. https://doi.org/10.1021/j100111a039.

[17] R. Ameta, M.S. Solanki, S. Benjamin, S.C. Ameta, Photocatalysis, in: Adv. Oxid. Process. Waste Water Treat., Elsevier, 2018: pp. 135–175. https://doi.org/10.1016/B978-0-12-810499-6.00006-1.

[18] Z. Wang, H. Huang, G. Li, X. Yan, Z. Yu, K. Wang, Y. Wu, Advances in engineering perovskite oxides for photochemical and photoelectrochemical water

splitting, Appl. Phys. Rev. 8 (2021) 021320. https://doi.org/10.1063/5.0039197.

[19] K. Maeda, Rhodium-Doped Barium Titanate Perovskite as a Stable p-Type Semiconductor Photocatalyst for Hydrogen Evolution under Visible Light, ACS Appl. Mater. Interfaces. 6 (2014) 2167–2173. https://doi.org/10.1021/am405293e.

[20] X. Ma, X. Cui, Z. Zhao, M.A. Melo, E.J. Roberts, F.E. Osterloh, Use of surface photovoltage spectroscopy to probe energy levels and charge carrier dynamics in transition metal (Ni, Cu, Fe, Mn, Rh) doped $SrTiO_3$ photocatalysts for H_2 evolution from water, J. Mater. Chem. A. 6 (2018) 5774–5781. https://doi.org/10.1039/C7TA10934B.

[21] K. Shimizu, Y. Tsuji, T. Hatamachi, K. Toda, T. Kodama, M. Sato, Y. Kitayama, Photocatalytic water splitting on hydrated layered perovskite tantalate $A_2SrTa_2O_7 \cdot nH_2O$ (A = H, K, and Rb), Phys. Chem. Chem. Phys. 6 (2004) 1064–1069. https://doi.org/10.1039/B312620J.

[22] H. Mizoguchi, H.W. Eng, P.M. Woodward, Probing the Electronic Structures of Ternary Perovskite and Pyrochlore Oxides Containing Sn^{4+} or Sb^{5+}, Inorg. Chem. 43 (2004) 1667–1680. https://doi.org/10.1021/ic034551c.

[23] N. Diot, R. Marchand, J. Haines, J.M. Léger, P. Macaudière, S. Hull, Crystal Structure Determination of the Oxynitride Sr_2TaO_3N, J. Solid State Chem. 146 (1999) 390–393. https://doi.org/10.1006/jssc.1999.8369.

[24] D. Ostermann, H. Jacobs, B. Harbrecht, Natriumoxonitridometallate(VI) von Molybdän und Wolfram, $Na_4MO_2N_2$ (M = Mo, W), Zeitschrift Für Anorg. Und Allg. Chemie. 619 (1993) 1277–1282. https://doi.org/10.1002/zaac.19936190721.

[25] S.G. Ebbinghaus, H.-P. Abicht, R. Dronskowski, T. Müller, A. Reller, A. Weidenkaff, Perovskite-related oxynitrides – Recent developments in synthesis, characterisation and investigations of physical properties, Prog. Solid State Chem. 37 (2009) 173–205. https://doi.org/10.1016/j.progsolidstchem.2009.11.003.

[26] C.A. Hancock, T. Herranz, J.F. Marco, F.J. Berry, P.R. Slater, Low temperature

fluorination of $Sr_3Fe_2O_{7-x}$ with polyvinylidine fluoride: An X-ray powder diffraction and Mössbauer spectroscopy study, J. Solid State Chem. 186 (2012) 195–203. https://doi.org/10.1016/j.jssc.2011.12.016.

[27] K. Qiu, Y. Liu, J. Tan, T. Wang, G. Zhang, Z. Liu, W. Jin, Fluorine-doped barium cobaltite perovskite membrane for oxygen separation and syngas production, Ceram. Int. 46 (2020) 27469–27475. https://doi.org/10.1016/j.ceramint.2020.07.235.

[28] D.O. Charkin, A.V. Sadakov, O.E. Omel'yanovskii, S.M. Kazakov, Synthesis, crystal structure, and properties of novel perovskite oxychalcogenides, Ca_2CuFeO_3Ch (Ch=S, Se), Mater. Res. Bull. 45 (2010) 2012–2016. https://doi.org/10.1016/j.materresbull.2010.07.023.

[29] J. Yu, X. Xu, Fluorination over Cr doped layered perovskite Sr_2TiO_4 for efficient photocatalytic hydrogen production under visible light illumination, J. Energy Chem. 51 (2020) 30–38. https://doi.org/10.1016/j.jechem.2020.03.025.

[30] H. Zhang, S. Ni, Y. Mi, X. Xu, Ruddlesden-Popper compound Sr_2TiO_4 co-doped with La and Fe for efficient photocatalytic hydrogen production, J. Catal. 359 (2018) 112–121. https://doi.org/10.1016/j.jcat.2017.12.031.

[31] X. Sun, X. Xu, Efficient photocatalytic hydrogen production over La/Rh co-doped Ruddlesden-Popper compound Sr_2TiO_4, Appl. Catal. B Environ. 210 (2017) 149–159. https://doi.org/10.1016/j.apcatb.2017.03.063.

[32] R. Kadari, G. Ravi, P. Venkataswamy, R. Velchuri, N.R. Munirathnam, M. Vithal, Effect of ion (Ag^+, N^{3-}) doping on the photocatalytic activity of the Ruddlesden–Popper-type layered perovskite $K_2Nd_2Ti_3O_{10}$, Comptes Rendus Chim. 22 (2019) 667–677. https://doi.org/10.1016/j.crci.2019.10.004.

[33] A. Staykov, H. Tellez, J. Druce, J. Wu, T. Ishihara, J. Kilner, Electronic properties and surface reactivity of SrO-terminated $SrTiO_3$ and SrO-terminated iron-doped $SrTiO_3$, Sci. Technol. Adv. Mater. 19 (2018) 221–230. https://doi.org/10.1080/14686996.2018.1440136.

[34] J.I. Pankove, D.A. Kiewit, Optical Processes in Semiconductors, J. Electrochem. Soc. 119 (1972) 156C. https://doi.org/10.1149/1.2404256.

[35] G. Zhao, Y. Sun, W. Zhou, X. Wang, K. Chang, G. Liu, H. Liu, T. Kako, J. Ye, Superior Photocatalytic H_2 Production with Cocatalytic Co/Ni Species Anchored on Sulfide Semiconductor, Adv. Mater. 29 (2017) 1703258. https://doi.org/10.1002/adma.201703258.

[36] T. Hisatomi, J. Kubota, K. Domen, Recent advances in semiconductors for photocatalytic and photoelectrochemical water splitting, Chem. Soc. Rev. 43 (2014) 7520–7535. https://doi.org/10.1039/C3CS60378D.

[37] H. Bantawal, U.S. Shenoy, D.K. Bhat, Vanadium-Doped SrTiO3 Nanocubes: Insight into role of vanadium in improving the photocatalytic activity, Appl. Surf. Sci. 513 (2020) 145858. https://doi.org/10.1016/j.apsusc.2020.145858.

[38] Z. KUANG, F. LI, J. LUO, Y. WANG, D. YUAN, Q. WANG, H. ZHAO, S. WANG, N. ZHAO, F. XIAO, LaCuZnX (X=Al, Zr, Al+Zr) perovskite-like catalysts treated by $NaBH_4$ and their catalytic performance for CO_2 hydrogenation to methanol, J. Fuel Chem. Technol. 48 (2020) 293–301. https://doi.org/10.1016/S1872-5813(20)30012-8.

[39] J. Low, B. Cheng, J. Yu, Surface modification and enhanced photocatalytic CO_2 reduction performance of TiO_2: a review, Appl. Surf. Sci. 392 (2017) 658–686. https://doi.org/10.1016/j.apsusc.2016.09.093.

[40] J. Yu, J. Low, W. Xiao, P. Zhou, M. Jaroniec, Enhanced Photocatalytic CO_2 -Reduction Activity of Anatase TiO_2 by Coexposed {001} and {101} Facets, J. Am. Chem. Soc. 136 (2014) 8839–8842. https://doi.org/10.1021/ja5044787.

[41] T. Kimijima, K. Kanie, M. Nakaya, A. Muramatsu, Solvothermal synthesis of $SrTiO_3$ nanoparticles precisely controlled in surface crystal planes and their photocatalytic activity, Appl. Catal. B Environ. 144 (2014) 462–467. https://doi.org/10.1016/j.apcatb.2013.07.051.

[42] T. Alammar, V. Smetana, H. Pei, I. Hamm, M. Wark, A. Mudring, The Power of Ionic Liquids: Crystal Facet Engineering of $SrTiO_3$ Nanoparticles for Tailored Photocatalytic Applications, Adv. Sustain. Syst. 5 (2021) 2000180. https://doi.org/10.1002/adsu.202000180.

[43] T. Alammar, I. Hamm, V. Grasmik, M. Wark, A.-V. Mudring, Microwave-

Assisted Synthesis of Perovskite $SrSnO_3$ Nanocrystals in Ionic Liquids for Photocatalytic Applications, Inorg. Chem. 56 (2017) 6920–6932. https://doi.org/10.1021/acs.inorgchem.7b00279.

[44] R. Li, C. Li, Photocatalytic Water Splitting on Semiconductor-Based Photocatalysts, in: 2017: pp. 1–57. https://doi.org/10.1016/bs.acat.2017.09.001.

[45] G.H. Zohuri, K. Albahily, E.D. Schwerdtfeger, S.A. Miller, Metallocene Alkene Polymerization Catalysts, in: Polym. Sci. A Compr. Ref., Elsevier, 2012: pp. 673–697. https://doi.org/10.1016/B978-0-444-53349-4.00081-9.

[46] J. Yang, D. Wang, H. Han, C. Li, Roles of Cocatalysts in Photocatalysis and Photoelectrocatalysis, Acc. Chem. Res. 46 (2013) 1900–1909. https://doi.org/10.1021/ar300227e.

[47] H. Yan, J. Yang, G. Ma, G. Wu, X. Zong, Z. Lei, J. Shi, C. Li, Visible-light-driven hydrogen production with extremely high quantum efficiency on Pt–PdS/CdS photocatalyst, J. Catal. 266 (2009) 165–168. https://doi.org/10.1016/j.jcat.2009.06.024.

[48] H. Kato, Y. Sasaki, N. Shirakura, A. Kudo, Synthesis of highly active rhodium-doped $SrTiO_3$ powders in Z-scheme systems for visible-light-driven photocatalytic overall water splitting, J. Mater. Chem. A. 1 (2013) 12327. https://doi.org/10.1039/c3ta12803b.

[49] K. Maeda, D. Lu, K. Domen, Solar-Driven Z-scheme Water Splitting Using Modified $BaZrO_3$ –$BaTaO_2N$ Solid Solutions as Photocatalysts, ACS Catal. 3 (2013) 1026–1033. https://doi.org/10.1021/cs400156m.

[50] R. Niishiro, S. Tanaka, A. Kudo, Hydrothermal-synthesized SrTiO3 photocatalyst codoped with rhodium and antimony with visible-light response for sacrificial H_2 and O_2 evolution and application to overall water splitting, Appl. Catal. B Environ. 150–151 (2014) 187–196. https://doi.org/10.1016/j.apcatb.2013.12.015.

[51] X. Chang, T. Wang, P. Yang, G. Zhang, J. Gong, The Development of Cocatalysts for Photoelectrochemical CO_2 Reduction, Adv. Mater. 31 (2019) 1804710. https://doi.org/10.1002/adma.201804710.

[52] Y. Hori, Electrochemical CO_2 Reduction on Metal Electrodes, in: Mod. Asp. Electrochem., Springer New York, New York, NY, n.d.: pp. 89–189. https://doi.org/10.1007/978-0-387-49489-0_3.

[53] X. Li, J. Wen, J. Low, Y. Fang, J. Yu, Design and fabrication of semiconductor photocatalyst for photocatalytic reduction of CO_2 to solar fuel, Sci. China Mater. 57 (2014) 70–100. https://doi.org/10.1007/s40843-014-0003-1.

[54] S. Zeng, P. Kar, U.K. Thakur, K. Shankar, A review on photocatalytic CO_2 reduction using perovskite oxide nanomaterials, Nanotechnology. 29 (2018) 052001. https://doi.org/10.1088/1361-6528/aa9fb1.

[55] J. Hong, W. Zhang, J. Ren, R. Xu, Photocatalytic reduction of CO_2: a brief review on product analysis and systematic methods, Anal. Methods. 5 (2013) 1086. https://doi.org/10.1039/c2ay26270c.

[56] E. Luévano-Hipólito, L.M. Torres-Martínez, CO_2 photoreduction with H_2O to C1 and C2 products over perovskite films of alkaline niobates $ANbO_3$ (A = Li, Na, K), Fuel. 320 (2022) 123934. https://doi.org/10.1016/j.fuel.2022.123934.

[57] J. Wu, Y. Huang, W. Ye, Y. Li, CO_2 Reduction: From the Electrochemical to Photochemical Approach, Adv. Sci. 4 (2017) 1700194. https://doi.org/10.1002/advs.201700194.

[58] K. Li, B. Peng, T. Peng, Recent Advances in Heterogeneous Photocatalytic CO_2 Conversion to Solar Fuels, ACS Catal. 6 (2016) 7485–7527. https://doi.org/10.1021/acscatal.6b02089.

[59] C. Zhang, Y. Guo, Y. Guo, G. Lu, A. Boreave, L. Retailleau, A. Baylet, A. Giroir-Fendler, $LaMnO_3$ perovskite oxides prepared by different methods for catalytic oxidation of toluene, Appl. Catal. B Environ. 148–149 (2014) 490–498. https://doi.org/10.1016/j.apcatb.2013.11.030.

[60] H. Wang, Q. Zhang, M. Qiu, B. Hu, Synthesis and application of perovskite-based photocatalysts in environmental remediation: A review, J. Mol. Liq. 334 (2021) 116029. https://doi.org/10.1016/j.molliq.2021.116029.

[61] K. Wei, Y. Faraj, G. Yao, R. Xie, B. Lai, Strategies for improving perovskite

photocatalysts reactivity for organic pollutants degradation: A review on recent progress, Chem. Eng. J. 414 (2021) 128783. https://doi.org/10.1016/j.cej.2021.128783.

[62] L. Jing, Y. Xu, M. Xie, J. Liu, J. Deng, L. Huang, H. Xu, H. Li, Three dimensional polyaniline/$MgIn_2S_4$ nanoflower photocatalysts accelerated interfacial charge transfer for the photoreduction of Cr(VI), photodegradation of organic pollution and photocatalytic H_2 production, Chem. Eng. J. 360 (2019) 1601–1612. https://doi.org/10.1016/j.cej.2018.10.214.

[63] C.E. Choong, K.T. Wong, H. Kim, S.B. Jang, S.Y. Yoon, I.W. Nah, W. Kim, S.-H. Kim, B.-H. Jeon, Y. Yoon, M. Jang, Unexpected discovery of superoxide radical generation by oxygen vacancies containing biomass derived granular activated carbon, Water Res. 190 (2021) 116757. https://doi.org/10.1016/j.watres.2020.116757.

[64] E. Jiang, N. Song, G. Che, C. Liu, H. Dong, L. Yang, Construction of a Z-scheme $MoS_2/CaTiO_3$ heterostructure by the morphology-controlled strategy towards enhancing photocatalytic activity, Chem. Eng. J. 399 (2020) 125721. https://doi.org/10.1016/j.cej.2020.125721.

[65] D.Q. Fei, T. Hudaya, A.A. Adesina, Visible-light activated titania perovskite photocatalysts: Characterisation and initial activity studies, Catal. Commun. 6 (2005) 253–258. https://doi.org/10.1016/j.catcom.2005.01.006.

[66] H. Su, L. Jing, K. Shi, C. Yao, H. Fu, Synthesis of large surface area $LaFeO_3$ nanoparticles by SBA-16 template method as high active visible photocatalysts, J. Nanoparticle Res. 12 (2010) 967–974. https://doi.org/10.1007/s11051-009-9647-5.

[67] B. Dong, Z. Li, Z. Li, X. Xu, M. Song, W. Zheng, C. Wang, S.S. Al-Deyab, M. El-Newehy, Highly Efficient $LaCoO_3$ Nanofibers Catalysts for Photocatalytic Degradation of Rhodamine B, J. Am. Ceram. Soc. 93 (2010) 3587–3590. https://doi.org/10.1111/j.1551-2916.2010.04124.x.

[68] S.S.K. Ma, T. Hisatomi, K. Domen, Hydrogen Production by Photocatalytic Water Splitting, J. Japan Pet. Inst. 56 (2013) 280–287.

https://doi.org/10.1627/jpi.56.280.

[69] S. Yang, H. Wang, H. Yu, S. Zhang, Y. Fang, S. Zhang, F. Peng, A facile fabrication of hierarchical Ag nanoparticles-decorated N-TiO_2 with enhanced photocatalytic hydrogen production under solar light, Int. J. Hydrogen Energy. 41 (2016) 3446–3455. https://doi.org/10.1016/j.ijhydene.2015.12.190.

[70] M. Wang, Y. Na, M. Gorlov, L. Sun, Light-driven hydrogen production catalysed by transition metal complexes in homogeneous systems, Dalt. Trans. (2009) 6458. https://doi.org/10.1039/b903809d.

[71] C.A. Linkous, C. Huang, J.R. Fowler, UV photochemical oxidation of aqueous sodium sulfide to produce hydrogen and sulfur, J. Photochem. Photobiol. A Chem. 168 (2004) 153–160. https://doi.org/10.1016/j.jphotochem.2004.03.028.

[72] V. Kumaravel, M. Imam, A. Badreldin, R. Chava, J. Do, M. Kang, A. Abdel-Wahab, Photocatalytic Hydrogen Production: Role of Sacrificial Reagents on the Activity of Oxide, Carbon, and Sulfide Catalysts, Catalysts. 9 (2019) 276. https://doi.org/10.3390/catal9030276.

[73] T. Ohmori, H. Takahashi, H. Mametsuka, E. Suzuki, Photocatalytic oxygen evolution on α-Fe_2O_3 films using Fe^{3+} ion as a sacrificial oxidizing agent, Phys. Chem. Chem. Phys. 2 (2000) 3519–3522. https://doi.org/10.1039/b003977m.

[74] S. Fukuzumi, D. Hong, Y. Yamada, Bioinspired Photocatalytic Water Reduction and Oxidation with Earth-Abundant Metal Catalysts, J. Phys. Chem. Lett. 4 (2013) 3458–3467. https://doi.org/10.1021/jz401560x.

[75] J. Schneider, D.W. Bahnemann, Undesired Role of Sacrificial Reagents in Photocatalysis, J. Phys. Chem. Lett. 4 (2013) 3479–3483. https://doi.org/10.1021/jz4018199.

[76] C.-C. Hu, C.-C. Tsai, H. Teng, Structure Characterization and Tuning of Perovskite-Like $NaTaO_3$ for Applications in Photoluminescence and Photocatalysis, J. Am. Ceram. Soc. 92 (2009) 460–466. https://doi.org/10.1111/j.1551-2916.2008.02869.x.

[77] H. Hayashi, Y. Hakuta, Y. Kurata, Hydrothermal synthesis of potassium niobate

photocatalysts under subcritical and supercritical water conditions, J. Mater. Chem. 14 (2004) 2046. https://doi.org/10.1039/b400130n.

[78] G. Li, Z. Yi, Y. Bai, W. Zhang, H. Zhang, Anisotropy in photocatalytic oxidization activity of $NaNbO_3$ photocatalyst, Dalt. Trans. 41 (2012) 10194. https://doi.org/10.1039/c2dt30593c.

[79] C.M. Cho, J.H. Noh, I.-S. Cho, J.-S. An, K.S. Hong, J.Y. Kim, Low-Temperature Hydrothermal Synthesis of Pure $BiFeO_3$ Nanopowders Using Triethanolamine and Their Applications as Visible-Light Photocatalysts, J. Am. Ceram. Soc. 91 (2008) 3753–3755. https://doi.org/10.1111/j.1551-2916.2008.02689.x.

[80] T.-N. Ye, M. Xu, W. Fu, Y.-Y. Cai, X. Wei, K.-X. Wang, Y.-N. Zhao, X.-H. Li, J.-S. Chen, The crystallinity effect of mesocrystalline $BaZrO_3$ hollow nanospheres on charge separation for photocatalysis, Chem. Commun. 50 (2014) 3021–3023. https://doi.org/10.1039/C4CC00101J.

[81] W.F. Zhang, J. Tang, J. Ye, Photoluminescence and photocatalytic properties of $SrSnO_3$ perovskite, Chem. Phys. Lett. 418 (2006) 174–178. https://doi.org/10.1016/j.cplett.2005.10.122.

[82] S. Fu, H. Niu, Z. Tao, J. Song, C. Mao, S. Zhang, C. Chen, D. Wang, Low temperature synthesis and photocatalytic property of perovskite-type $LaCoO_3$ hollow spheres, J. Alloys Compd. 576 (2013) 5–12. https://doi.org/10.1016/j.jallcom.2013.04.092.

[83] Y. Li, S. Yao, W. Wen, L. Xue, Y. Yan, Sol–gel combustion synthesis and visible-light-driven photocatalytic property of perovskite $LaNiO_3$, J. Alloys Compd. 491 (2010) 560–564. https://doi.org/10.1016/j.jallcom.2009.10.269.

[84] Y. Li, G. Chen, C. Zhou, Z. Li, Photocatalytic Water Splitting Over a Protonated Layered Perovskite Tantalate $H_{1.81}Sr_{0.81}Bi_{0.19}Ta_2O_7$, Catal. Letters. 123 (2008) 80–83. https://doi.org/10.1007/s10562-008-9397-5.

[85] S. Ikeda, M. Hara, J.N. Kondo, K. Domen, H. Takahashi, T. Okubo, M. Kakihana, Preparation of $K_2La_2Ti_3O_{10}$ by Polymerized Complex Method and Photocatalytic Decomposition of Water, Chem. Mater. 10 (1998) 72–77. https://doi.org/10.1021/cm970221c.

[86] J. Sato, N. Saito, H. Nishiyama, Y. Inoue, New Photocatalyst Group for Water Decomposition of RuO_2 -Loaded p-Block Metal (In, Sn, and Sb) Oxides with d 10 Configuration, J. Phys. Chem. B. 105 (2001) 6061–6063. https://doi.org/10.1021/jp010794j.

[87] D. Arney, L. Fuoco, J. Boltersdorf, P.A. Maggard, Flux Synthesis of $Na_2Ca_2Nb_4O_{13}$: The Influence of Particle Shapes, Surface Features, and Surface Areas on Photocatalytic Hydrogen Production, J. Am. Ceram. Soc. 96 (2013) 1158–1162. https://doi.org/10.1111/jace.12122.

[88] S. NISHIMOTO, Y. OKAZAKI, M. MATSUDA, M. MIYAKE, Photocatalytic H_2 evolution by layered perovskite Ca3Ti2O7 codoped with Rh and Ln (Ln = La, Pr, Nd, Eu, Gd, Yb, and Y) under visible light irradiation, J. Ceram. Soc. Japan. 117 (2009) 1175–1179. https://doi.org/10.2109/jcersj2.117.1175.

[89] Z. Liang, K. Tang, Q. Shao, G. Li, S. Zeng, H. Zheng, Synthesis, crystal structure, and photocatalytic activity of a new two-layer Ruddlesden–Popper phase, $Li_2CaTa_2O_7$, J. Solid State Chem. 181 (2008) 964–970. https://doi.org/10.1016/j.jssc.2008.01.042.

[90] H. JEONG, T. KIM, D. KIM, K. KIM, Hydrogen production by the photocatalytic overall water splitting on $NiO/Sr_3Ti_2O_7NiO/Sr_3Ti_2O_7$: Effect of preparation method, Int. J. Hydrogen Energy. 31 (2006) 1142–1146. https://doi.org/10.1016/j.ijhydene.2005.10.005.

[91] Y.-G. Ko, W.Y. Lee, Effects of Nickel-Loading Method on the Water-Splitting Activity of a Layered $NiO_x/Sr_4Ti_3O_{10}$ Photocatalyst, Catal. Letters. 83 (2002) 157–160. https://doi.org/10.1023/A:1021021627635.

[92] T. Takata, Y. Furumi, K. Shinohara, A. Tanaka, M. Hara, J.N. Kondo, K. Domen, Photocatalytic Decomposition of Water on Spontaneously Hydrated Layered Perovskites, Chem. Mater. 9 (1997) 1063–1064. https://doi.org/10.1021/cm960612b.

[93] A. Kudo, S. Hijii, H_2 or O_2 Evolution from Aqueous Solutions on Layered Oxide Photocatalysts Consisting of Bi^{3+} with $6s^2$ Configuration and d^0 Transition Metal Ions, Chem. Lett. 28 (1999) 1103–1104. https://doi.org/10.1246/cl.1999.1103.

[94] Y. Shimodaira, H. Kato, H. Kobayashi, A. Kudo, Photophysical Properties and Photocatalytic Activities of Bismuth Molybdates under Visible Light Irradiation, J. Phys. Chem. B. 110 (2006) 17790–17797. https://doi.org/10.1021/jp0622482.

[95] H.G. Kim, D.W. Hwang, J.S. Lee, An Undoped, Single-Phase Oxide Photocatalyst Working under Visible Light, J. Am. Chem. Soc. 126 (2004) 8912–8913. https://doi.org/10.1021/ja049676a.

[96] K. Iizuka, T. Wato, Y. Miseki, K. Saito, A. Kudo, Photocatalytic Reduction of Carbon Dioxide over Ag Cocatalyst-Loaded $ALa_4Ti_4O_{15}$ (A = Ca, Sr, and Ba) Using Water as a Reducing Reagent, J. Am. Chem. Soc. 133 (2011) 20863–20868. https://doi.org/10.1021/ja207586e.

[97] W. Chen, C. Li, H. Gao, J. Yuan, W. Shangguan, J. Su, Y. Sun, Photocatalytic water splitting on protonated form of layered perovskites $K_{0.5}La_{0.5}Bi_2M_2O_9$ (M = Ta; Nb) by ion-exchange, Int. J. Hydrogen Energy. 37 (2012) 12846–12851. https://doi.org/10.1016/j.ijhydene.2012.05.090.

[98] M. Machida, J. Yabunaka, T. Kijima, Efficient photocatalytic decomposition of water with the novel layered tantalate $RbNdTa_2O_7$, Chem. Commun. (1999) 1939–1940. https://doi.org/10.1039/a905246a.

[99] X. Zong, C. Sun, Z. Chen, A. Mukherji, H. Wu, J. Zou, S.C. Smith, G.Q. Lu, L. Wang, Nitrogen doping in ion-exchangeable layered tantalate towards visible-light induced water oxidation, Chem. Commun. 47 (2011) 6293. https://doi.org/10.1039/c0cc05440b.

[100] K. Maeda, T.E. Mallouk, Comparison of two- and three-layer restacked Dion–Jacobson phase niobate nanosheets as catalysts for photochemical hydrogen evolution, J. Mater. Chem. 19 (2009) 4813. https://doi.org/10.1039/b903692j.

[101] Y. Ebina, T. Sasaki, M. Harada, M. Watanabe, Restacked Perovskite Nanosheets and Their Pt-Loaded Materials as Photocatalysts, Chem. Mater. 14 (2002) 4390–4395. https://doi.org/10.1021/cm020622e.

[102] D. Arney, P.A. Maggard, Effect of Platelet-Shaped Surfaces and Silver-Cation Exchange on the Photocatalytic Hydrogen Production of $RbLaNb_2O_7$, ACS Catal. 2 (2012) 1711–1717. https://doi.org/10.1021/cs200643h.

[103] Y. Huang, Y. Wei, L. Fan, M. Huang, J. Lin, J. Wu, Photocatalytic activities of $HLaNb_2O_7$ prepared by polymerized complex method, Int. J. Hydrogen Energy. 34 (2009) 5318–5325. https://doi.org/10.1016/j.ijhydene.2009.04.040.

[104] Y. Huang, Y. Li, Y. Wei, M. Huang, J. Wu, Photocatalytic property of partially substituted Pt-intercalated layered perovskite, $ASr_2Ta_xNb_{3-x}O_{10}$ (A=K, H; x=0, 1, 1.5, 2 and 3), Sol. Energy Mater. Sol. Cells. 95 (2011) 1019–1027. https://doi.org/10.1016/j.solmat.2010.12.017.

[105] J. Boltersdorf, P.A. Maggard, Silver Exchange of Layered Metal Oxides and Their Photocatalytic Activities, ACS Catal. 3 (2013) 2547–2555. https://doi.org/10.1021/cs400466b.

[106] C. Acar, I. Dincer, C. Zamfirescu, A review on selected heterogeneous photocatalysts for hydrogen production, Int. J. Energy Res. 38 (2014) 1903–1920. https://doi.org/10.1002/er.3211.

[107] M. Ni, M.K.H. Leung, D.Y.C. Leung, K. Sumathy, A review and recent developments in photocatalytic water-splitting using TiO_2 for hydrogen production, Renew. Sustain. Energy Rev. 11 (2007) 401–425. https://doi.org/10.1016/j.rser.2005.01.009.

[108] A. FUJISHIMA, K. HONDA, Electrochemical Photolysis of Water at a Semiconductor Electrode, Nature. 238 (1972) 37–38. https://doi.org/10.1038/238037a0.

[109] W. Choi, A. Termin, M.R. Hoffmann, The Role of Metal Ion Dopants in Quantum-Sized TiO_2 : Correlation between Photoreactivity and Charge Carrier Recombination Dynamics, J. Phys. Chem. 98 (1994) 13669–13679. https://doi.org/10.1021/j100102a038.

[110] J. Soria, J.C. Conesa, V. Augugliaro, L. Palmisano, M. Schiavello, A. Sclafani, Dinitrogen photoreduction to ammonia over titanium dioxide powders doped with ferric ions, J. Phys. Chem. 95 (1991) 274–282. https://doi.org/10.1021/j100154a052.

[111] J. Engweiler, J. Harf, A. Baiker, WO_x/TiO_2 Catalysts Prepared by Grafting of Tungsten Alkoxides: Morphological Properties and Catalytic Behavior in the

Selective Reduction of NO by NH_3, J. Catal. 159 (1996) 259–269. https://doi.org/10.1006/jcat.1996.0087.

[112] G. BALASUBRAMANIAN, D. DIONYSIOU, M. SUIDAN, I. BAUDIN, J. LAINE, Evaluating the activities of immobilized TiO_2 powder films for the photocatalytic degradation of organic contaminants in water, Appl. Catal. B Environ. 47 (2004) 73–84. https://doi.org/10.1016/j.apcatb.2003.04.002.

[113] B.L. Phoon, C.W. Lai, G.-T. Pan, T.C.-K. Yang, J.C. Juan, One-pot hydrothermal synthesis of strontium titanate nanoparticles photoelectrode using electrophoretic deposition for enhancing photoelectrochemical water splitting, Ceram. Int. 44 (2018) 9923–9933. https://doi.org/10.1016/j.ceramint.2018.03.017.

[114] K. van Benthem, C. Elsässer, R.H. French, Bulk electronic structure of $SrTiO_3$: Experiment and theory, J. Appl. Phys. 90 (2001) 6156–6164. https://doi.org/10.1063/1.1415766.

[115] C. Wang, H. Qiu, T. Inoue, Q. Yao, Band gap engineering of $SrTiO_3$ for water splitting under visible light irradiation, Int. J. Hydrogen Energy. 39 (2014) 12507–12514. https://doi.org/10.1016/j.ijhydene.2014.06.059.

[116] X. Yu, Y. Lin, H. Liu, C. Yang, Y. Peng, C. Du, S. Wu, X. Li, Y. Zhong, Photocatalytic performances of heterojunction catalysts of silver phosphate modified by PANI and Cr-doped $SrTiO_3$ for organic pollutant removal from high salinity wastewater, J. Colloid Interface Sci. 561 (2020) 379–395. https://doi.org/10.1016/j.jcis.2019.10.123.

[117] J. Pan, Y. Liu, W. Ou, S. Li, H. Li, J. Wang, C. Song, Y. Zheng, C. Li, The photocatalytic hydrogen evolution enhancement of the MoS_2 lamellas modified g-C_3N_4/$SrTiO_3$ core-shell heterojunction, Renew. Energy. 161 (2020) 340–349. https://doi.org/10.1016/j.renene.2020.07.097.

[118] X. Sun, Y. Xie, F. Wu, H. Chen, M. Lv, S. Ni, G. Liu, X. Xu, Photocatalytic Hydrogen Production over Chromium Doped Layered Perovskite Sr_2TiO_4, Inorg. Chem. 54 (2015) 7445–7453. https://doi.org/10.1021/acs.inorgchem.5b01042.

[119] Y. Zhu, H.A. Tahini, Z. Hu, J. Dai, Y. Chen, H. Sun, W. Zhou, M. Liu, S.C. Smith, H. Wang, Z. Shao, Unusual synergistic effect in layered

Ruddlesden−Popper oxide enables ultrafast hydrogen evolution, Nat. Commun. 10 (2019) 149. https://doi.org/10.1038/s41467-018-08117-6.

[120] H. Kato, Y. Takeda, M. Kobayashi, H. Kobayashi, M. Kakihana, Photoluminescence Properties of Layered Perovskite-Type Strontium Scandium Oxyfluoride Activated With Mn^{4+}, Front. Chem. 6 (2018). https://doi.org/10.3389/fchem.2018.00467.

[121] J.N. Yun, Z.Y. Zhang, J.F. Yan, W. Zhao, First-principles study of Sc-doping effect on the stability, electronic structure and photocatalytic properties of Sr_2TiO_4, Thin Solid Films. 542 (2013) 276–280. https://doi.org/10.1016/j.tsf.2013.06.067.

[122] Y. Jia, S. Shen, D. Wang, X. Wang, J. Shi, F. Zhang, H. Han, C. Li, Composite $Sr_2TiO_4/SrTiO_3$(La,Cr) heterojunction based photocatalyst for hydrogen production under visible light irradiation, J. Mater. Chem. A. 1 (2013) 7905. https://doi.org/10.1039/c3ta11326d.

[123] X. Xu, R. Wang, X. Sun, M. Lv, S. Ni, Layered Perovskite Compound $NaLaTiO_4$ Modified by Nitrogen Doping as a Visible Light Active Photocatalyst for Water Splitting, ACS Catal. 10 (2020) 9889–9898. https://doi.org/10.1021/acscatal.0c02626.

[124] R.D. Shannon, Revised effective ionic radii and systematic studies of interatomic distances in halides and chalcogenides, Acta Crystallogr. Sect. A. 32 (1976) 751–767. https://doi.org/10.1107/S0567739476001551.

[125] H. Chen, C. Lim, M. Zhou, Z. He, X. Sun, X. Li, Y. Ye, T. Tan, H. Zhang, C. Yang, J.W. Han, Y. Chen, Activating Lattice Oxygen in Perovskite Oxide by B-Site Cation Doping for Modulated Stability and Activity at Elevated Temperatures, Adv. Sci. 8 (2021) 2102713. https://doi.org/10.1002/advs.202102713.

[126] F.A. Akgul, G. Akgul, N. Yildirim, H.E. Unalan, R. Turan, Influence of thermal annealing on microstructural, morphological, optical properties and surface electronic structure of copper oxide thin films, Mater. Chem. Phys. 147 (2014) 987–995. https://doi.org/10.1016/j.matchemphys.2014.06.047.

[127] Z. Li, K.-H. Xue, J. Wang, J.-G. Li, X. Ao, H. Sun, X. Song, W. Lei, Y. Cao, C. Wang, Cation and Anion Co-doped Perovskite Nanofibers for Highly Efficient Electrocatalytic Oxygen Evolution, ACS Appl. Mater. Interfaces. 12 (2020) 41259–41268. https://doi.org/10.1021/acsami.0c10045.

[128] X.-G. Yan, W.-Q. Huang, G.-F. Huang, L. Xu, S.-Q. Zhan, Z.-M. Yang, Z. Wan, P. Peng, Band-Gap Widening of Nitrogen-Doped Cu2O: New Insights from First-Principles Calculations, Sci. Adv. Mater. 6 (2014) 1221–1227. https://doi.org/10.1166/sam.2014.1896.

[129] P. Zhang, Y. Gong, J. Lin, Photocurrent Response of Two -Metal(II) Complexes Based on Rigid Ligands, Eur. J. Inorg. Chem. 2016 (2016) 322–329. https://doi.org/10.1002/ejic.201501114.

[130] G. Anuradha, G. Vasuki, I.A. Khan, M. V. Kulkarni, Crystal and Molecular Structure of N-[2-(6-Methoxy-2-oxo-2H-Chromen-4-yl-Benzofuran-3-yl]-Benzamide, Cryst. Struct. Theory Appl. 01 (2012) 107–113. https://doi.org/10.4236/csta.2012.13020.

[131] Y. Matsumoto, Y. Miura, S. Takata, Thickness-Dependent Flat Band Potential of Anatase TiO_2 (001) Epitaxial Films on Nb:$SrTiO_3$ (001) Investigated by UHV-Electrochemistry Approach, J. Phys. Chem. C. 120 (2016) 1472–1477. https://doi.org/10.1021/acs.jpcc.5b08708.

[132] P.I. Kyesmen, N. Nombona, M. Diale, Effects of Film Thickness and Coating Techniques on the Photoelectrochemical Behaviour of Hematite Thin Films, Front. Energy Res. 9 (2021). https://doi.org/10.3389/fenrg.2021.683293.

[133] H. Xiao, P. Liu, W. Wang, R. Ran, W. Zhou, Z. Shao, Enhancing the photocatalytic activity of Ruddlesden-Popper Sr_2TiO_4 for hydrogen evolution through synergistic silver doping and moderate reducing pretreatment, Mater. Today Energy. 23 (2022) 100899. https://doi.org/10.1016/j.mtener.2021.100899.

[134] W. Guo, C. Bo, W. Li, Z. Feng, E. Cong, L. Yang, L. Yang, Enhanced Photocatalytic Activity of Nonuniformly Nitrogen-Doped Nb_2O_5 by Prolonging the Lifetime of Photogenerated Holes, Nanomaterials. 12 (2022) 1690. https://doi.org/10.3390/nano12101690.

[135] K. Iwashina, A. Kudo, Rh-Doped $SrTiO_3$ Photocatalyst Electrode Showing Cathodic Photocurrent for Water Splitting under Visible-Light Irradiation, J. Am. Chem. Soc. 133 (2011) 13272–13275. https://doi.org/10.1021/ja2050315.

[136] H. Yoshida, A. Yamamoto, Photocatalytic activation of water with metal loaded photocatalysts prepared by a flux method, in: 2016: p. 020001. https://doi.org/10.1063/1.4946904.

[137] H. Kato, K. Asakura, A. Kudo, Highly Efficient Water Splitting into H_2 and O_2 over Lanthanum-Doped $NaTaO_3$ Photocatalysts with High Crystallinity and Surface Nanostructure, J. Am. Chem. Soc. 125 (2003) 3082–3089. https://doi.org/10.1021/ja027751g.

[138] H. Xiao, P. Liu, W. Wang, R. Ran, W. Zhou, Z. Shao, Ruddlesden–Popper Perovskite Oxides for Photocatalysis-Based Water Splitting and Wastewater Treatment, Energy & Fuels. 34 (2020) 9208–9221. https://doi.org/10.1021/acs.energyfuels.0c02301.

[139] F. Lichtenberg, A. Herrnberger, K. Wiedenmann, Synthesis, structural, magnetic and transport properties of layered perovskite-related titanates, niobates and tantalates of the type $A_nB_nO_{3n+2}$, $A'A_{k-1}B_kO_{3k+1}$ and $A_mB_{m-1}O_{3m}$, Prog. Solid State Chem. 36 (2008) 253–387. https://doi.org/10.1016/j.progsolidstchem.2008.10.001.

[140] M. Hojamberdiev, M.F. Bekheet, E. Zahedi, H. Wagata, Y. Kamei, K. Yubuta, A. Gurlo, N. Matsushita, K. Domen, K. Teshima, New Dion–Jacobson Phase Three-Layer Perovskite $CsBa_2Ta_3O_{10}$ and Its Conversion to Nitrided $Ba_2Ta_3O_{10}$ Nanosheets via a Nitridation–Protonation–Intercalation–Exfoliation Route for Water Splitting, Cryst. Growth Des. 16 (2016) 2302–2308. https://doi.org/10.1021/acs.cgd.6b00081.

[141] D. Jiang, W. Ma, Y. Yao, P. Xiao, B. Wen, D. Li, M. Chen, Dion–Jacobson-type perovskite $KCa_2Ta_3O_{10}$ nanosheets hybridized with g-C_3N_4 nanosheets for photocatalytic H_2 production, Catal. Sci. Technol. 8 (2018) 3767–3773. https://doi.org/10.1039/C8CY00930A.

[142] A.V. Knyazev, O.V. Krasheninnikova, E.V. Syrov, V.M. Kyashkin, M.I. Lelet,

N.N. Smirnova, Thermodynamic and X-ray studies of layered perovskite $KCa_2NaNb_4O_{13}$, J. Chem. Thermodyn. 138 (2019) 255–261. https://doi.org/10.1016/j.jct.2019.06.031.

[143] Y. Okamoto, S. Ida, J. Hyodo, H. Hagiwara, T. Ishihara, Synthesis and Photocatalytic Activity of Rhodium-Doped Calcium Niobate Nanosheets for Hydrogen Production from a Water/Methanol System without Cocatalyst Loading, J. Am. Chem. Soc. 133 (2011) 18034–18037. https://doi.org/10.1021/ja207103j.

[144] H.G. Kim, D.W. Hwang, J. Kim, Y.G. Kim, J.S. Lee, Highly donor-doped (110) layered perovskite materials as novel photocatalysts for overall water splitting, Chem. Commun. (1999) 1077–1078. https://doi.org/10.1039/a902892g.

[145] K. Domen, S. Naito, T. Onishi, K. Tamaru, M. Soma, Study of the photocatalytic decomposition of water vapor over a nickel(II) oxide-strontium titanate ($SrTiO_3$) catalyst, J. Phys. Chem. 86 (1982) 3657–3661. https://doi.org/10.1021/j100215a032.

[146] H. Suzuki, O. Tomita, M. Higashi, A. Nakada, R. Abe, Improved visible-light activity of nitrogen-doped layered niobate photocatalysts by NH_3-nitridation with KCl flux, Appl. Catal. B Environ. 232 (2018) 49–54. https://doi.org/10.1016/j.apcatb.2018.03.007.

[147] Y. Ebina, K. Akatsuka, K. Fukuda, T. Sasaki, Synthesis and In Situ X-ray Diffraction Characterization of Two-Dimensional Perovskite-Type Oxide Colloids with a Controlled Molecular Thickness, Chem. Mater. 24 (2012) 4201–4208. https://doi.org/10.1021/cm302480h.

[148] A.J. Jacobson, J.W. Johnson, J.T. Lewandowski, Interlayer chemistry between thick transition-metal oxide layers: synthesis and intercalation reactions of $K[Ca_2Na_{n-3}Nb_nO_{3n+1}]$ (3 .ltoreq. n .ltoreq. 7), Inorg. Chem. 24 (1985) 3727–3729. https://doi.org/10.1021/ic00217a006.

[149] R. Liu, B. Feng, Y. Ma, H. Liu, J. Cui, D. Yang, H. Yuan, Synthesis of layered-perovskite $KCa_2Na_{n-3}Nb_nO_{3n+1}$ with different layer thickness, Mater. Lett. 281 (2020) 128635. https://doi.org/10.1016/j.matlet.2020.128635.

[150] J. Cui, X. Wu, S. Yang, C. Li, F. Tang, J. Chen, Y. Chen, Y. Xiang, X. Wu, Z. He, Cryptomelane-Type KMn_8O_{16} as Potential Cathode Material — for Aqueous Zinc Ion Battery, Front. Chem. 6 (2018). https://doi.org/10.3389/fchem.2018.00352.

[151] G.C. Gomes, F.F. Borghi, R.O. Ospina, E.O. López, F.O. Borges, A. Mello, Nd:YAG (532 nm) pulsed laser deposition produces crystalline hydroxyapatite thin coatings at room temperature, Surf. Coatings Technol. 329 (2017) 174–183. https://doi.org/10.1016/j.surfcoat.2017.09.008.

[152] A. Al-Mamoori, S. Lawson, A.A. Rownaghi, F. Rezaei, Improving Adsorptive Performance of CaO for High-Temperature CO_2 Capture through Fe and Ga Doping, Energy & Fuels. 33 (2019) 1404–1413. https://doi.org/10.1021/acs.energyfuels.8b03996.

[153] D. Briggs, Handbook of X-ray Photoelectron Spectroscopy C. D. Wanger, W. M. Riggs, L. E. Davis, J. F. Moulder and G. E.Muilenberg Perkin-Elmer Corp., Physical Electronics Division, Eden Prairie, Minnesota, USA, 1979. 190 pp. $195, Surf. Interface Anal. 3 (1981) v–v. https://doi.org/10.1002/sia.740030412.

[154] K. Skrodczky, M.M. Antunes, X. Han, S. Santangelo, G. Scholz, A.A. Valente, N. Pinna, P.A. Russo, Niobium pentoxide nanomaterials with distorted structures as efficient acid catalysts, Commun. Chem. 2 (2019) 129. https://doi.org/10.1038/s42004-019-0231-3.

[155] L. Hu, X. Liu, S. Dalgleish, M.M. Matsushita, H. Yoshikawa, K. Awaga, Organic optoelectronic interfaces with anomalous transient photocurrent, J. Mater. Chem. C. 3 (2015) 5122–5135. https://doi.org/10.1039/C5TC00414D.

[156] K.A. Lehuta, A. Haldar, D. Zhou, K.R. Kittilstved, Spectroscopic Study of the Reversible Chemical Reduction and Reoxidation of Substitutional Cr Ions in Sr_2TiO_4, Inorg. Chem. 56 (2017) 9177–9184. https://doi.org/10.1021/acs.inorgchem.7b01210.

[157] W. Wang, R. Tran, J. Qu, Y. Liu, C. Chen, M. Xu, Y. Chen, S.P. Ong, L. Wang, W. Zhou, Z. Shao, Chlorine-Doped Perovskite Oxide: A Platinum-Free Cathode for Dye-Sensitized Solar Cells, ACS Appl. Mater. Interfaces. 11 (2019) 35641–

35652. https://doi.org/10.1021/acsami.9b07966.

[158] W. Meng, B. Saparov, F. Hong, J. Wang, D.B. Mitzi, Y. Yan, Alloying and Defect Control within Chalcogenide Perovskites for Optimized Photovoltaic Application, Chem. Mater. 28 (2016) 821–829. https://doi.org/10.1021/acs.chemmater.5b04213.